UNIVERSITY OF THESSALY

SCHOOL OF ENGINEERING

DEPARTMENT OF MECHANICAL ENGINEERING

Doctor of Philosophy Dissertation

FATIGUE CRACK GROWTH PREDICTION UNDER MODE I LOADING IN FRICTION STIR ALUMINUM ALLOY WELD

by

ANDREAS TZAMTZIS

Diploma of Mechanical Engineering, U.Th., 2007

Master of Science (M.Sc.), Department of Mechanical Engineering, U.Th., 2011

Submitted in partial fulfillment

of the requirements of the degree

of Doctor of Philosophy

Volos, 2015

Examination Committee:

Dr. Alexis Kermanidis, Assistant Professor, Dept. of Mechanical Engineering, University of Thessaly

Dr. Nikolaos Aravas, Professor, Department of Mechanical Engineering, University of Thessaly

Dr. Gregory Haidemenopoulos, Professor, Dept. of Mechanical Engineering, University of Thessaly

Dr. Spyros Pantelakis, Professor, Dept. of Mechanical & Aeronautics Engineering, University of Patras

Dr. Antonios Giannakopoulos, Professor, Dept. of Civil Engineering, University of Thessaly

Dr. Spyros Karamanos, Professor, Dept. of Mechanical Engineering, University of Thessaly

Dr. Paraskevas Papanikos, Assistant Professor, Dept. of Product and System Design Engineering, University of Aegean

Ackowledgements

Many people have contributed directly and indirectly to the completion of this dissertation. First of all, I would like to express my sincere gratitude to the supervisor of this thesis, Assistant Professor A. Kermanidis, for giving me the opportunity to obtain my PhD degree. His support and guidance have contributed to the achievement of the scopes of this PhD project. Also, I am grateful to him for giving me the possibility for being a member of the Mechanics & Strength of Materials Laboratory of the University of Thessaly.

I am also thankful to the other members of the examining committee for their remarks and suggestions that improved the study. Especially, I would like to express my gratitude to Professors N. Aravas, G. Haidemenopoulos and Sp. Pantelakis for permitting me to use equipment of their Laboratories. Their support was significant for the completion of this thesis. Furthermore, I would like to thank A. Zervaki, E. Kamoutsi, P. Christodoulou, A. Chamos and A. Dafereras for their help and collaboration. Moreover, I am grateful to my friends and colleagues for their friendship and support.

This dissertation is dedicated to my family for their support all these years of my studies.

Andreas Tzamtzis

FATIGUE CRACK GROWTH PREDICTION UNDER MODE I LOADING IN FRICTION STIR ALUMINUM ALLOY WELD

ANDREAS TZAMTZIS

University of Thessaly, Department of Mechanical Engineering, 2015

Supervisor: Dr. Alexis Kermanidis, Assistant Professor

Abstract

The damage tolerance approach has been used in the design of light structures in the transport sector since the early 1970's. It refers to the ability of a structure to withstand damage and therefore understanding and predicting the behavior of a damaged structure is the basis for successful implementation of this design philosophy.

In aeronautics industry, airframes are primarily made of riveted Al-alloy panels, with a skin and stringer configuration. The requirement for reducing manufacturing and operational costs has lead aerospace industries to look for new, attractive ways to substitute conventional riveting techniques in airframes. Towards this direction, advanced welding technologies such as friction stir and laser beam welding are a promising solution.

In welded structures, damage tolerance assessment is a difficult problem due to the variation of material characteristics in the weld region. The simultaneous presence of a modified due to welding microstructure and weld residual stresses influences the behavior of a propagating crack. For this reason, simulation tools for assessment of crack growth in a welded joint, demand a careful examination of the mechanisms controlling crack propagation. In the present thesis, the effects of weld microstructure and weld residual stresses on fatigue crack propagation in a 2024 T3 friction stir weld have been assessed experimentally and analytically. To investigate the effect of weld microstructure on fatigue crack growth, the microstructure in the heat affected zone (HAZ) was simulated in parent material using a special heat treatment method. Fatigue crack growth rate was experimentally determined in the HAZ simulated material and in the friction stir weld (FSW) by means of fatigue crack growth tests.

In the analytical part, a model was developed to predict mode I fatigue crack growth perpendicular to the friction stir weld line. The model takes into account the independent influences of weld microstructure and residual stresses on fatigue crack propagation. Comparison of analytical results to experimental data showed that the model is suitable for predicting the rate of a growing crack in a friction stir weld under mode I loading.

From the present investigation, additional knowledge is extracted concerning the basic mechanisms that contribute to fatigue crack propagation in a friction stir weld region. Furthermore, an analytical tool is proposed for the evaluation of the remaining fatigue life of a cracked friction stir welded aluminum panel.

Table of contents

Nomenclature

A_{25}	elongation at fracture
α	crack length
c	fatigue ductility exponent
D	parameter of Paris equation
$d\alpha/dN$	fatigue crack growth rate
dW/dN	strain energy contained in a unit material volume
$(dW/dN)_{max}$	maximum strain energy density
$(dW/dN)_{min}$	minimum strain energy density
E	Young's modulus
H	strength coefficient
H´	cyclic strength coefficient
$Hv_{0.2}$	Vicker's hardness (applied force 200gr)
K_c	fracture toughness
K_{cr}	critical stress intensity factor
$K_{max,app}$	maximum applied stress intensity factor
$K_{min,app}$	minimum applied stress intensity factor
$K_{max,total}$	maximum stress intensity factor derived from superposition of external stresses and residual stresses
$K_{min,total}$	minimum stress intensity factor derived from superposition of external stresses and residual stresses
K_{op}	stress intensity factor corresponding to P_{op}
K_{res}	residual stress intensity factor

m	Paris equation exponent
N	number of cycles
N_f	fatigue life
N_{ini}	phase (number of cycles) for fatigue crack initiation
$N_{hardening}$	phase (number of cycles) for cyclic hardening
N_{sat}	phase (number of cycles) for maximum cyclic stress saturation
n	strain hardening exponent
n'	cyclic strain hardening exponent
P	force
P_{op}	crack opening load
P_{max}	maximum applied load
R	stress/strain ratio
R_{eff}	effective stress ratio
r	radial distance from crack tip used in SED criterion
r_c	critical radial distance from crack tip (at fracture) used in SED criterion
r_{cy}	cyclic plastic zone size
r_y	monotonic plastic zone size
S	strain energy density factor
S_c	critical strain energy density factor
S_{min}	minimum strain energy density factor
V_r	tool rotation speed
V_f	welding speed

W_f	critical amount of energy accumulated in a material after a finite number of loading cycles
ΔN	critical number of cycles for failure of material element
Δr	width of material element at the crack tip subjected to low cycle fatigue
ΔK	stress intensity factor range
ΔK_{app}	applied stress intensity factor range
ΔK_{eff}	effective stress intensity factor range
ΔK_{th}	stress intensity threshold
ΔW	absorbed plastic strain energy per cycle
$\Delta \alpha$	crack growth increment
$\Delta \varepsilon_{pm}$	mean plastic strain range
$\Delta \varepsilon_p$	plastic strain range
$\Delta \sigma$	stress range
$\varepsilon_{p,\alpha}$	plastic strain amplitude
$\varepsilon_f{}'$	fatigue ductility coefficient
θ	nuting angle
μ	shear modulus of elasticity
v	Poisson ratio
σ_c	critical stress for onset of crack extension
σ_A	stress amplitude
$\sigma_{y0.2}$	yield strength (offset 0.2%)
$\sigma_{c0.2}$	cyclic yield strength (offset 0.2%)
σ_{max}	maximum stress

σ_{min}	minimum stress
σ_p	tensile peak stress
$\sigma_y res(x)$	longitudinal residual stress (y-direction) at a position x with regard to the weld line
σ_{UTS}	tensile strength

Chapter 1: Introduction

1.1 Description of the technological problem

The demand for reduction of weight and production costs in the transport sector has led to re-examination of techniques used for manufacturing of components. In aircraft structural design, a promising solution in this direction is to replace riveted components with large structural elements manufactured as integral structures. In the frame of this concept, implementation of advanced welding technologies in both military and commercial airplanes combined with high-strength aluminum alloys with improved damage tolerance performance, has received significant attention (Figure 1.1). Apart from the attractive mechanical properties, welded integral structures can offer a cost saving of up to 60% over built-up (differential) structures.
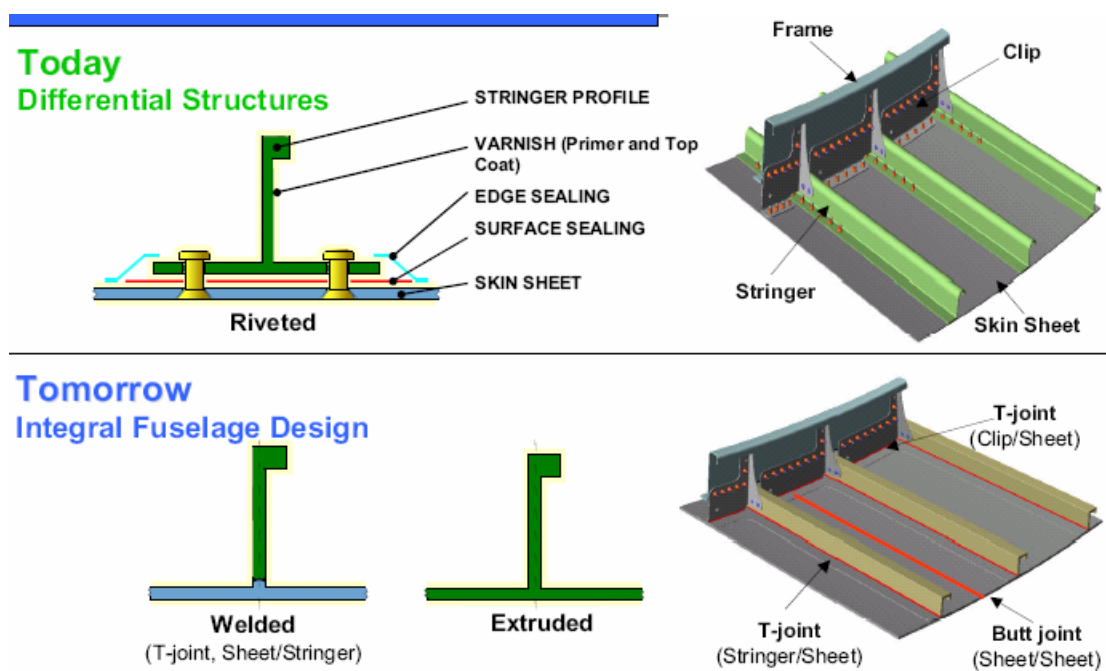
Figure 1.1 Riveted vs Integral structures [1].

Advanced welding techniques such as laser beam welding (LBW) and friction stir welding (FSW) are used in various civilian aircraft structures [2, 3]. The LBW process is currently used for skin-stringer joints (T-joints) and FSW for skin-skin joints (butt joints), but their application is restricted to the compression dominated lower part of the fuselage. Extending the level of technological implementation to more critical, tension dominated sections of the metallic airframes, requires a better understanding of the fatigue and damage tolerance

behavior of the welded structure.

The damage tolerant design philosophy is based on the ability of a structure to sustain defects safely until a repair procedure can be performed. In engineering design, the approach of damage tolerance is based on the assumption that flaws exist in any structure and may propagate under operational loads. Damage tolerant design is used extensively in aircraft construction and is mandatory for large civil aircrafts [4]. A maintenance program is implemented that results in the detection and repair of damage, in the form of corrosion and fatigue cracking, before such damage reduces the residual strength of the structure below an acceptable limit.

In welded structures, the distribution of defect sizes, inhomogeneous microstructure and residual stresses arising from the weld process, influence fatigue crack propagation, a problem that has to be considered in design. A reliable damage tolerance analysis requires knowledge on how parameters like weld residual stresses and microstructural variations influence the rate of a propagating fatigue crack (Figure 1.2).
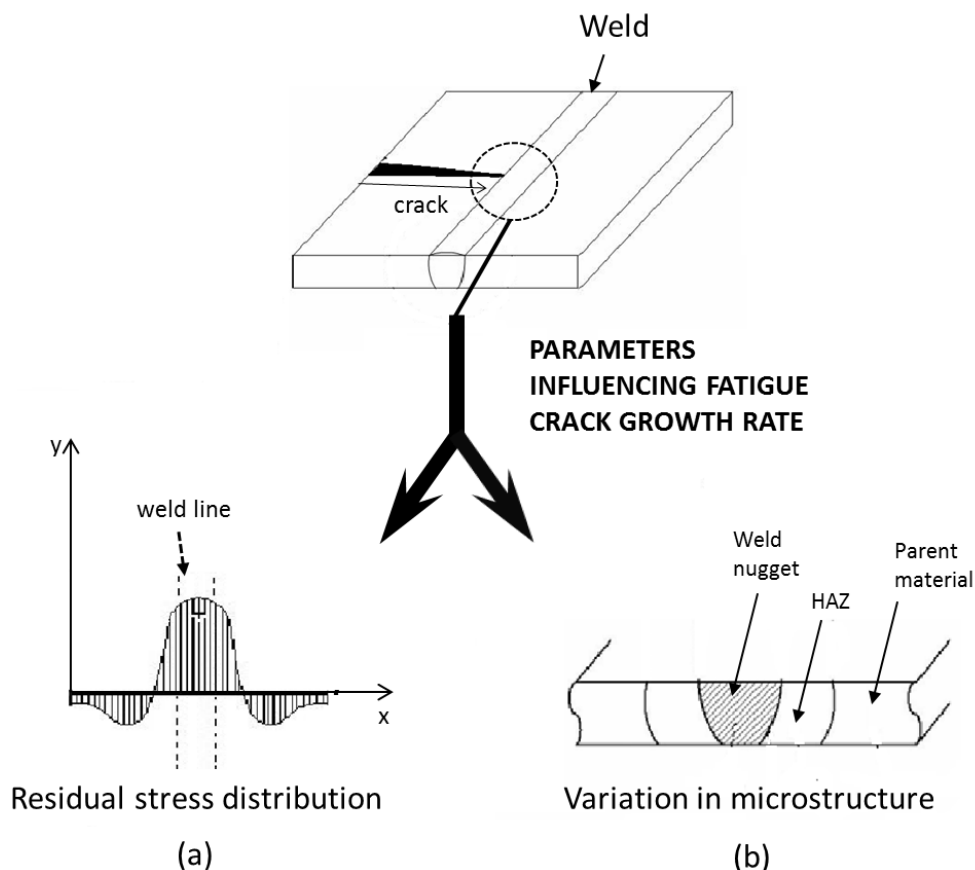
Figure 1.2 Parameters influencing mode I fatigue crack propagation in weld region

(a) residual stresses, (b) microstructural variations

2

1.2 Scope of the present work

In the present work the problem of a crack propagating perpendicular to a FSW under mode I loading has been investigated experimentally and analytically. In the analysis, the effects of microstructural variations and weld residual stresses on fatigue crack growth have been independently studied and the weight of each influence on crack growth rate has been assessed. To investigate the influence of weld microstructure on the propagating crack, a special heat treatment method was developed to simulate the heat affected zone (HAZ) microstructure of the weld region (Figure 1.3) in parent 2024 T3 material. With the implemented heat treatment process, overaged 2024 aluminum alloy was produced with microstructural characteristics and local property variation similar to the HAZ.
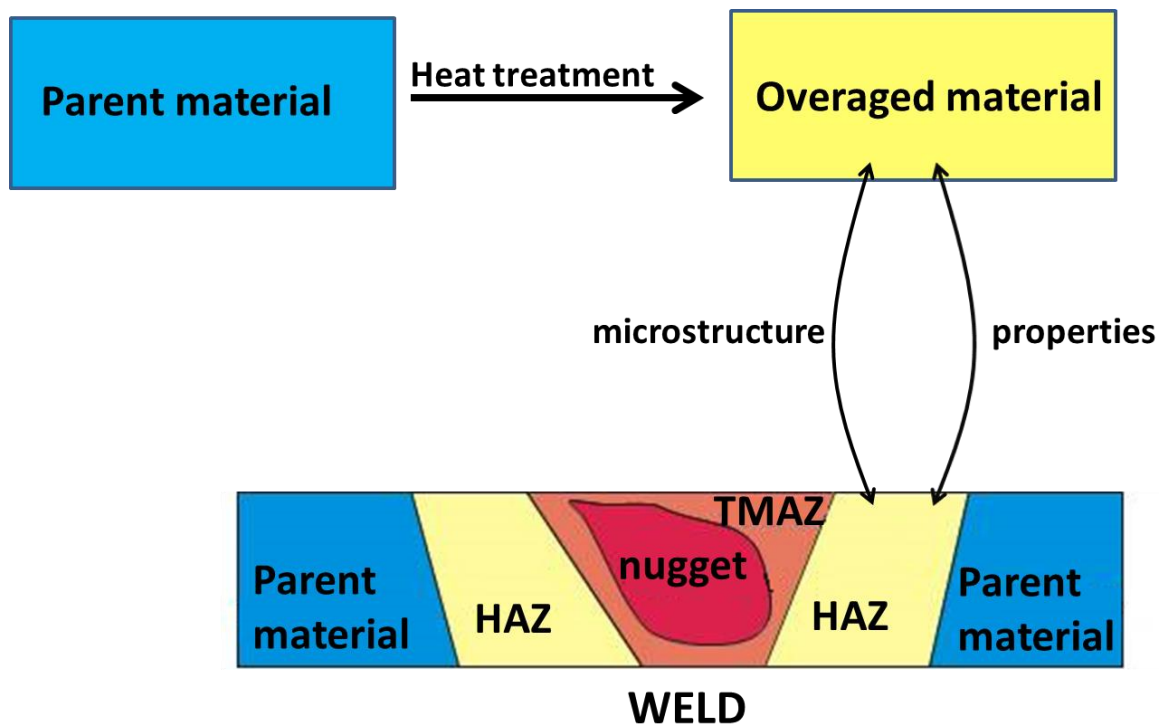
Figure 1.3 Methodology used for the simulation of HAZ microstructure in parent 2024 T3 aluminum alloy.

Two conditions of overaged 2024 alloy were investigated, one with uniform strength to assess the influence of overaging on the material mechanical properties, and one with strength gradient, which is a more accurate simulation of the local property variation in the HAZ. The mechanical performance and fracture behavior of the weld and heat treated material were assessed by means of tensile, fracture toughness and fatigue crack growth tests. Additionally, fractography was performed to examine the change of fracture characteristics due to

overaging of the material. Special attention was paid to the modifications in strain hardening characteristics, due to overaging treatment. The cyclic strain hardening behavior was investigated with strain controlled cyclic tests and was used in the analysis to explain the dissimilar FCG performance between parent and overaged material. Finally, microhardness measurements in the cross-section of the weld and residual stress measurements perpendicular to the FSW line were conducted.

In the analytical part of the work, a model was developed to predict FCG rate under mode I loading in the FSW. The model takes into account the effects of weld microstructure and weld residual stresses on fatigue crack propagation. It is assumed that crack growth occurs incrementally by damage accumulation. The critical energy for incremental crack growth is determined using the strain energy density (SED) criterion. For prediction of fatigue crack growth the cyclic properties of the overaged material are used. In the model the weld residual stresses are accounted for with the method of the superposition approach. The analytical simulations have been compared to experimental results in FSW 2024 T3 aluminum alloy.

A schematic representation of methodology used in the thesis is shown in Figure 1.4.
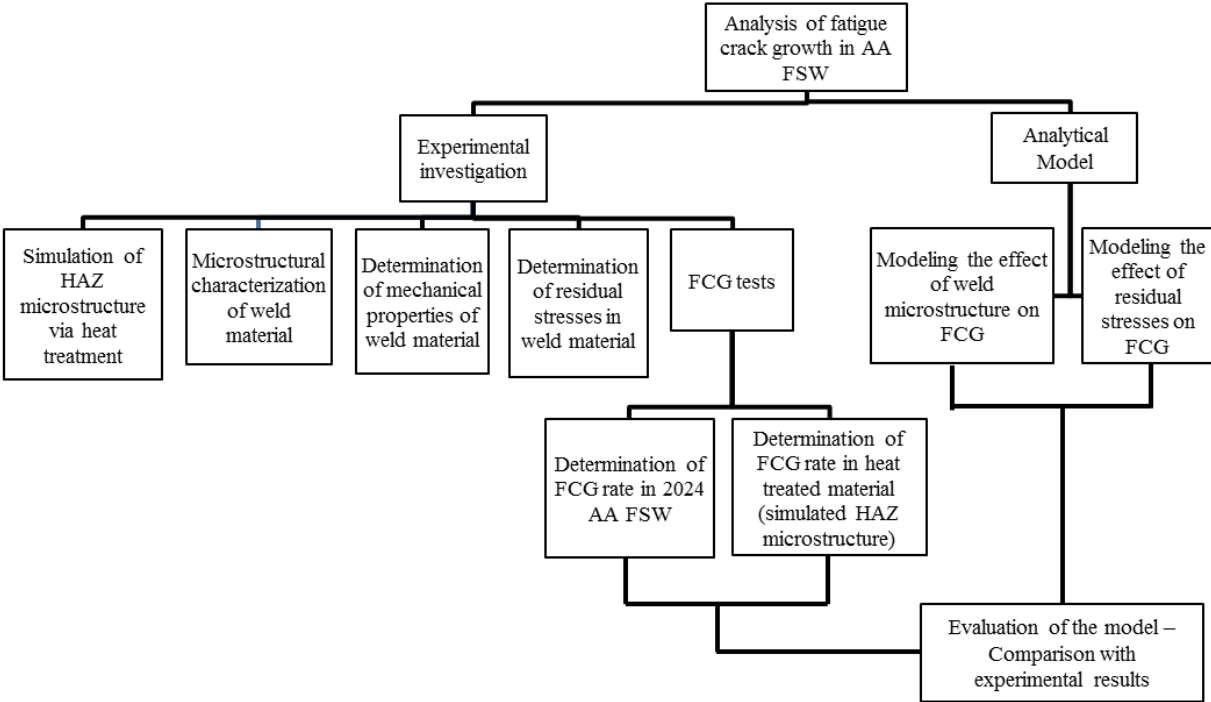
Figure 1.4 Methodology used in the thesis.

4

1.3 Layout of the dissertation

The dissertation is developed in 7 Chapters. In **Chapter 1** the description of the technological problem and the necessity of the investigation are presented. In **Chapter 2** relevant literature review is performed, which is focused on microstructural characteristics of FSW, basic mechanisms that influence stage II fatigue crack growth and existing models for the fatigue crack growth simulation. In **Chapters 3** and **4** the experimental methodology and results are presented and analyzed. They include friction stir welding of 2024 T3 aluminum alloy sheets, metallographic characterization, microhardness measurements in the weld region, determination of the profile of residual stresses and mechanical testing in the weld material (tensile tests, FCG tests, LCF tests and fracture toughness tests). Specific attention is paid on the heat treatment method used for the simulation of HAZ microstructure. In **Chapter 5** the analytical model for fatigue crack growth assessment in the weld region is developed. The parts that include (i) the effect of varying microstructure and (ii) the effect of weld residual stresses on fatigue crack growth are analyzed separately in two different sections. In **Chapter 6** the analytical results are presented and evaluation of the model is performed using experimental results from Chapter 4. Finally, in **Chapter 7** the conclusions of the present work and recommendations for further study are presented.

Chapter 2: Friction Stir Welding in aluminum alloys and intermediate fatigue crack growth

In this chapter the basic principles of FSW process are presented and a literature review on the basic mechanisms influencing fatigue crack propagation behavior is performed. Specific attention is paid to parameters influencing intermediate fatigue crack growth and contribute to crack closure. The basic models for simulation of constant amplitude fatigue crack growth are presented and the important scientific investigations examining fatigue crack growth in aluminum FSW are discussed.

2.1 Friction Stir Welding

Friction stir welding (FSW) was invented by Wayne Thomas at TWI Ltd in 1991. It is a patented process [5], and over 114 organizations have been granted licenses to use it. It has a broad industrial implementation, such as shipbuilding, marine, railway, land transportation and in aerospace it is used for the joining of aluminum alloy components.

Friction stir welding uses a non-consumable rotating tool (Figure 2.1a), which moves along the joint between two components to produce high-quality butt or lap welds. The FSW tool generally has a profiled pin and a shoulder with a larger diameter than that of the pin. The pin length is similar to the required weld depth. The pin passes through the joint line while the shoulder is in contact with the top surface of the work-piece to avoid expelling of softened material and provide consolidation.

In contrast to the traditional fusion-welding technologies, FSW is a solid-state metal joining process, which is generally employed in applications where the original material microstructure/properties must be maintained after joining. The advantages of FSW result from the fact that the welding process takes place in the solid phase, below the melting point of the materials to be welded. The benefits include the ability to join materials that are difficult to weld by fusion, for example 2xxx and 7xxx aluminum alloys, magnesium and copper. Friction stir welding can use purpose-design equipment or modified existing machine tool technology. With regard to the traditional fusion-welding technologies, FSW offers a number of advantages such as: (a) good mechanical properties in the as-welded condition, (b) improved safety due to the absence of toxic fumes or the spatter of molten material, (c) no consumables such as the filler metal or gas shield are required, (d) ease of process automation, (e) ability to operate in all positions (horizontal, vertical, overhead, orbital, etc.)

6

as there is no weld pool, and (f) low environmental impact. However, some disadvantages of the FSW process have also been identified such as: (a) an existing hole is left after the tool is withdrawn from the work-piece, (b) relatively large tool press-down and plates-clamping forces are required, (c) lower flexibility of the process with respect to variable thickness and non-linear welds, and (d) it is often associated with lower welding rates than conventional fusion-welding techniques, although this shortcoming is somewhat lessened since fewer welding passes are required.

Various thermo-mechanical processes such as friction-energy dissipation, plastic deformation and the associated heat dissipation, material transport/flow, dynamic recrystallization, local cooling, etc., and their complex interaction play a critical role in the FSW process [6-16]. Metallographic examinations of the FSW joints typically reveal the existence of the following four zones, (Figure 2.1b):

(a) An uneffected zone referred to as base metal (BM), which is far from the weld so that material microstructure/properties are not altered by the joining process.

(b) The heat-affected zone (HAZ), in which material microstructure/properties are affected only by the thermal effects associated with FSW. In heat treatable aluminum alloys, the HAZ is characterized by overaging conditions (coarsening of metastable phases), resulting in degradation of mechanical properties. While this zone is normally found in the case of fusion welds, the nature of the microstructural changes may be different in the FSW case due to generally lower temperatures.

(c) The thermo-mechanically affected zone (TMAZ), which is located closer than the HAZ to the weld center. Both the thermal (temperature gradients) and the mechanical aspects (plastic deformation due to stiring) of FSW affect the material microstructure/properties in this zone. The original grains may have undergone severe plastic deformation.

(d) The weld nugget which is the innermost zone of an FSW joint. As a result of the way the material is transported from the regions ahead of the tool to the wake regions behind the tool, this zone typically contains the so-called 'onion-ring' features. The material in this region has been subjected to severe conditions of plastic deformation and high temperature exposure and consequently contains a very fine dynamically recrystallized microstructure.
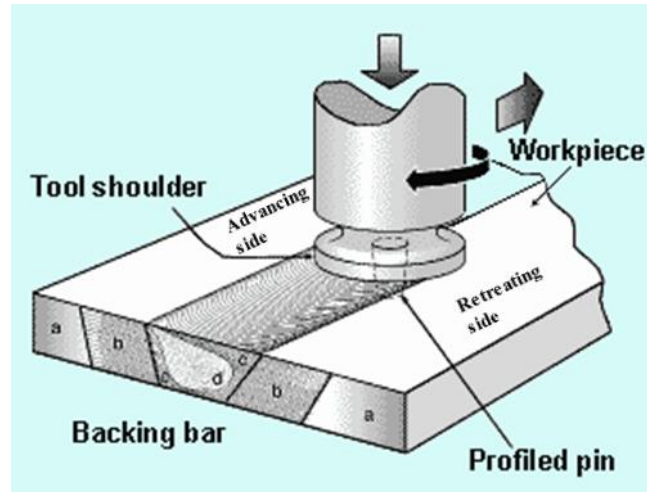
(a)
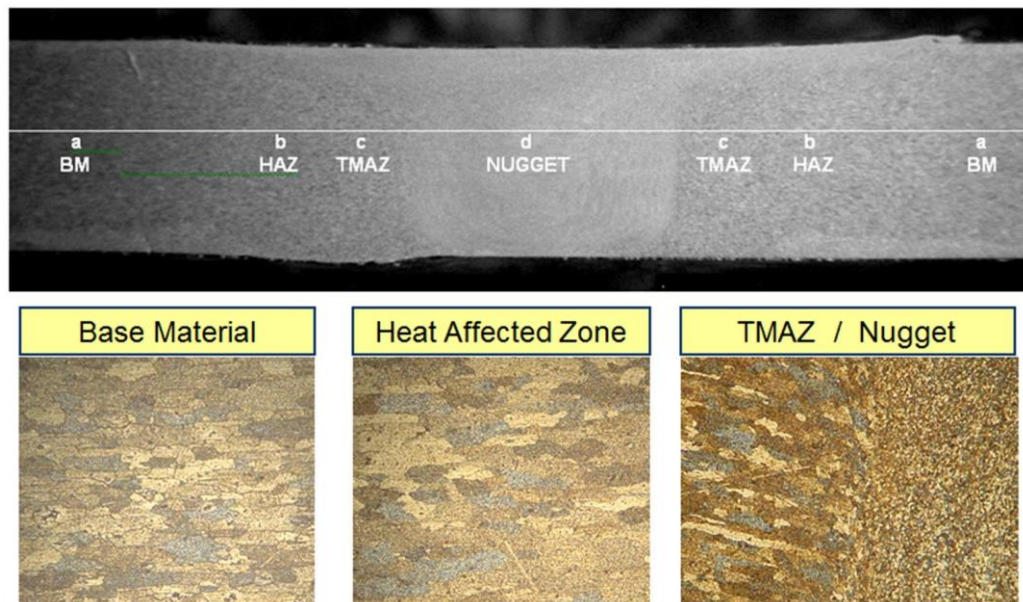
(b)

Figure 2.1 (a) Friction stir welding principle and (b) FSW microstructural zones (Metallographic analysis of a FSW 5083-H111 AA [17]).

The welding process parameters which typically influence the FSW quality (Figure 2.2) are: (a) the rotational and transverse velocities of the tool, (b) the tool-plunge depth, (c) the tool tilt-angle, and (d) the tool-design/material. Since, in general, higher temperatures are encountered in the case of higher rotational and lower transverse tool velocities, it is critical that a delicate balance between these two velocities is attained. Specifically, if the temperatures in the weld region are not high enough and the material has not been sufficiently softened, the weld zone may develop various flaws/defects arising from low ductility of the material. On the other hand, when the temperatures are too high, undesirable changes in the

material microstructure/properties may take place and possibly incipient-melting flaws may be created during joining. To ensure that the necessary level of shoulder/work-piece contact pressure is attained and that the tool fully penetrates the weld, the tool-plunge depth (defined as the depth of the lowest point of the shoulder below the surface of the weld plate) has to be set correctly. Tool rearward tilting by 2°-4° has been often found to be beneficial since it enhances the effect of the forging process [15, 16, 18]. Typically, insufficient tool-plunge depths (lack of penetration) result in low-quality welds due to inadequate forging of the material at the rear of the tool, while excessive tool-plunge depths lead to under-matching of the weld thickness compared to the base metal thickness. Kissing bond is a specific type of solid-state bonding defect, mainly occurs due to lack of penetration of the tool during the FSW process, where two previously separated regions of the material are in contact with little or no metallic bond present. Kissing bonds are a concern with FSW as such features can reduce fatigue performance of joints and are currently very difficult to detect (or accurately size) using existing NDT methods [3, 19, 20].

(a)   (b)
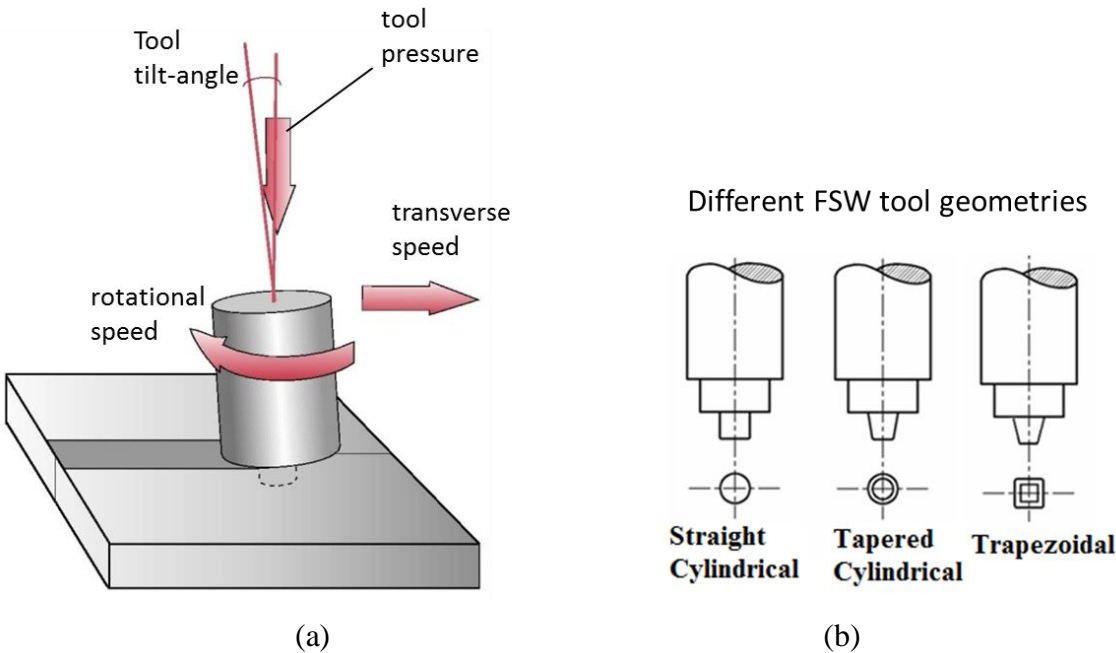
Figure 2.2 (a) Friction stir welding process parameters and (b) different geometries of welding tools.

2.2 Constant amplitude fatigue crack growth (Stage II)

The life of a cyclically loaded component consists of the crack initiation and crack propagation stages. Modern defect-tolerant design approaches are based on the premise that

engineering structures are inherently flawed. The useful fatigue life is the time or the number of cycles to propagate a dominant flaw of an assumed or measured initial size to a critical dimension. In most metallic materials, failure is preceded by a substantial amount of stable crack propagation under cyclic loading conditions. The rates at which the crack propagates for different combinations of applied stress, crack length and geometrical conditions as well as the mechanisms which influence crack propagation rates are topics of considerable scientific and practical interest.

In constant amplitude fatigue for a given material and set of conditions, the crack growth behavior can be described by the relation between cyclic crack growth rate ($d\alpha/dN$) and stress intensity range (ΔK_R):

$$\frac{da}{dN} = f(\Delta K_R) \qquad (2\text{-}1)$$

where R is the load ratio.

In Figure 2.3 a schematic ($d\alpha/dN$-ΔK) plot is presented, showing the different regimes of stable fatigue crack propagation.

At intermediate ΔK values, the rate of crack growth remains constant and ($d\alpha/dN$-ΔK) can be plotted as a straight line in log-log scale. The first approach to describe FCG in this stage (Stage II), is well known as the 'Paris law' and has the form [21]:

$$\frac{da}{dN} = D(\Delta K)^m \qquad (2\text{-}2)$$

where D and m are empirical parameters that depend on the material, environment, frequency, temperature and load ratio R. The load ratio is defined as:

$$R = \frac{\sigma_{min}}{\sigma_{max}} = \frac{K_{min}}{K_{max}} \qquad (2\text{-}3)$$

where K_{min}, K_{max} are the minimum and maximum values of the stress intensity factor and σ_{min}, σ_{max} are the minimum and maximum stress values. Although equation (2-2) is empirical, it still remains one of the most useful expressions in the analysis of FCG for a vast spectrum of materials and fatigue test conditions.
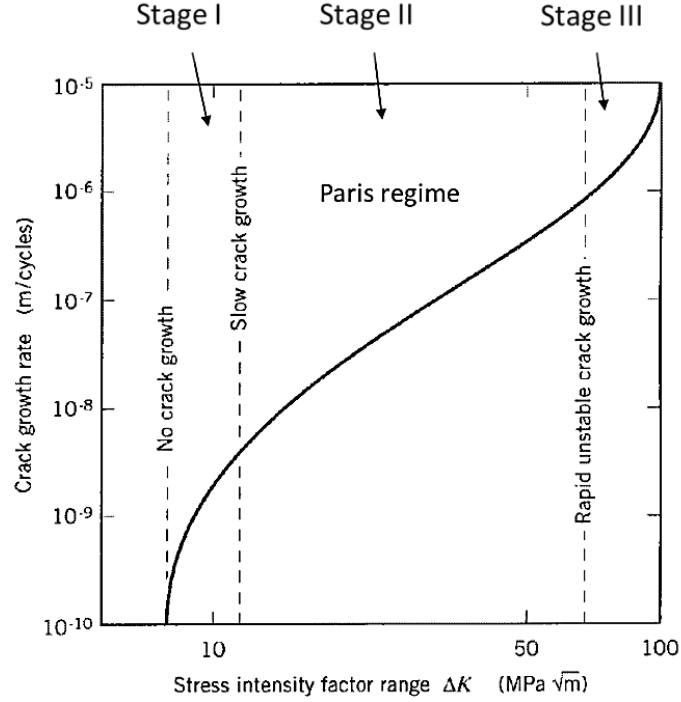
Figure 2.3 Schematic illustration of different regimes of stable fatigue crack propagation.

Many semi-empirical and empirical models have been proposed in the literature to account for the load ratio dependence of $d\alpha/dN$. The most notable and widely used for industrial design purposes, are the empirical approaches of Forman et al. [22] and Walker [23]. These models are described, respectively, by the following two equations:

$$\frac{da}{dN} = D_a \left\{ \frac{\Delta K^{m_a}}{(1-R)K_c - \Delta K} \right\} \tag{2-4}$$

and

$$\frac{da}{dN} = D_b \left\{ \frac{\Delta K^{m_b}}{(1-R)^{c_1}} \right\} \tag{2-5}$$

where D_a, D_b, m_a, m_b, c_1 are material constants and K_c is the fracture toughness. These models do not account for microstructural, environmental or load interaction effects and should be further modified empirically when marked levels of crack closure develop [24, 25].

2.2.1 Fatigue crack closure

Fatigue crack growth in aluminum alloys has been a subject of extensive research. The rate which a crack propagates under fatigue loads is influenced by several concurrent and

11

mutually competitive mechanistic processes involving the microstructure, mechanical load variables (ΔK and K_{max} value, stress ratio) and environment. Fatigue crack closure discovered by Elber [26, 27] is a parameter that has been investigated rigorously and has been linked to fatigue crack growth. The evolution of crack closure and associated retardation mechanisms during fatigue cannot be quantified accurately. They are strongly influenced by even small variations in the path of the crack, environmental conditions, loading conditions and testing methods. The basic mechanisms contributing to fatigue crack closure in ductile metals are i) plasticity-induced closure, ii) roughness induced closure, iii) transformation-induce closure, iv) hardening at the crack tip, and v) oxide-induced closure [24, 28].

In aluminum alloys, excluding the environmental factors, the most relevant mechanisms influencing crack closure are plasticity, roughness at the crack path and hardening at the crack tip. Elber [26, 27] monitored changes in the compliance of thin sheets of cracked 2024 T3 AA and observed that fracture surfaces of a fatigue crack come into premature contact during the unloading of a force cycle and reduction in crack opening displacement, causing a reduction in the apparent 'driving force' for fatigue crack growth. Crack closure was related to the crack-tip plasticity and was the result of residual plastic deformation left in the wake of the crack tip (plasticity induced crack closure). Since then, extensive work in aluminum alloys has been performed [29-32], demonstrating the influence of crack closure due to plasticity on Stage II crack growth.

The roughness induced closure effect is more microstructurally dependent and therefore more relevant in near threshold ΔK conditions [33-37]. However, several investigations have shown that certain microstructural aspects may influence fatigue crack propagation in early stages of intermediate growth (Stage II). In [38-40] the lower FCG rates in aluminum alloys with large and elongated grains, compared to the same alloys with smaller equiaxed grains, were associated with pronounced surface roughness induced closure at the crack path. The variation in grain morphology was a result of the different degree of plastic deformation of the alloys.

Theoretical approaches have shown that cyclic hardening is associated with increased crack closure levels under cyclic stresses [41-43]. Budiansky and Hutchinson [41] presented a theoretical model for the phenomenon of fatigue crack closure discovered experimentally by Elber [26, 27]. It was found that cyclic hardening enhances crack closure, while cyclic softening reduces closure levels. In [42], cyclic hardening was found to affect both crack closure and the shape of the plastic zone at the crack tip. It was shown that since the material

becomes more resistant due to work hardening it is easier to plastically deform it out of that initial plastic zone, than within the initial plastic zone. The higher the amount of hardening, the larger the spreading of the plastic zone around the initial site. For cyclic loading, the residual stresses in front of the crack tip make this area more difficult to plastically deform. Therefore cyclic plastic straining mostly occurs in an area located above and behind the crack tip increasing residual stresses in this area, which enhances crack closure. Microstructural characteristics, which can influence the hardening behavior in overaged aluminum alloys are the degree of incoherency and coarsening of second-phase particles with non-shearable characteristics, and the resulting Orowan bypassing mechanism of semi- or incoherent particles [44, 45].

Other micromechanical factors that may influence a propagating fatigue crack are local strength variations at the tip of a crack. In an early work, Reifsnider and Kahl [46] have shown that in the case of heat treatable aluminum alloys of 6xxx and 7xxx series, crack propagation rates depend on the slope of the yield strength gradient ahead the crack tip. It was demonstrated that crack propagation rates are reduced during the transition of a crack from a uniform strength region to a positive yield strength gradient. At larger crack lengths with continuous increasing strength the phenomenon is reversed and crack propagation rate increases up to the initial levels. The transient effects on fatigue crack growth rate observed reveal the strong dependency of crack propagation behavior on the local material properties at the tip of the crack.

2.2.2 Theories for prediction of constant amplitude fatigue crack growth (Stage II)

Fatigue crack growth rates are influenced by several interactive processes that involve the microstructure, mechanical load variables, environment and parameters associated with crack closure. Therefore, prediction of crack propagation rates is difficult and most models rely on empirical observations and experimental data, which however lack physical background. Theories based on physical principles, that have been proposed to predict fatigue crack growth in terms of ΔK, can be divided in two main categories. Theories based on geometrical factors (e.g. crack opening displacement) and rely on experimental correlation of striation spacing with crack growth rates [47-51], and theories based on accumulation of damage at the crack tip [52-59].

Laird and McClintock [49, 50] correlated the crack advance per cycle with the crack-tip opening displacement $\Delta\delta_t$, through equation (2-6):

$$\frac{da}{dN} \approx \Delta\delta_t = \beta \frac{(\Delta K)^2}{\sigma_{yc}E} \tag{2-6}$$

where σ_{yc} is the cyclic yield strength, E is Young's modulus in plane strain, and β is a material parameter.

More recently, Nicholls [47, 51] expressed the fatigue crack growth rate relating the crack tip radius during blunting with the crack opening displacement in the form:

$$\frac{da}{dN} = \Delta\alpha = \left(\frac{pb}{K_c^2}\right)^{1/(1-p)} \Delta K^{2/(1-p)} \tag{2-7}$$

where K_C is the fracture toughness, while parameters p and b are constants which relate the crack blunting with crack extension (Δα):

$$r = b\Delta\alpha^p \tag{2-8}$$

where r is the crack tip radius. Equation (2-7) requires the determination of constants b and p.

Damage accumulation models [52-59] use criteria for fatigue fracture, based on the critical value of accumulated strains or plastic work at the crack tip. Damage is calculated cycle-by-cycle or incrementally. Due to the complexity of the process most of the codes include a hierarchy of major simplifications, with most important being the application of the linear elastic fracture mechanics (LEFM) concept. In the model developed by McClintock [59], fatigue crack growth occurs when the following function of the local average plastic strain amplitude $\varepsilon_{p,\alpha}$ at the crack tip and the true plastic strain for monotonic fracture $\varepsilon_{(true),f}$, integrated over the number of fatigue cycles N, reaches unity:

$$\int_0^N 4\left(\frac{\varepsilon_{p,a}}{\varepsilon_{(true),f}}\right)^k dn = 1 \tag{2-9}$$

where k exponent takes the values 1 or 2.

Rice [52] and Weertman [53] independently proposed essentially identical damage

accumulation models which consider plasticity of a discrete surface of tensile yielding or slip ahead of the crack. In [52] crack growth was assumed to occur when the total absorbed hysteresis energy reaches a critical value U* per unit area of newly created fracture surface. By assuming that crack growth rate is constant for fracture over a distance of a cyclic plastic zone, for small-scale yielding the crack growth rate was given by:

$$\frac{da}{dN} = \frac{5\pi\left(1-\nu^2\right)\varepsilon_y\sigma_y}{96U^*}\left(\frac{\Delta K}{\sigma_y}\right)^4 \tag{2-10}$$

where ε_y is the yield strain, σ_y is the yield strength and ν is the Poisson's ratio. For cyclically hardening or softening materials, σ_y and ε_y should be replaced by the corresponding values for cyclic loading. The difficulty of the model is in determining parameter U*. Weertman [53] developed a damage accumulation theory similar to that of Rice. His analysis revealed that the FCG rate can be described by:

$$\frac{da}{dN} \propto \frac{(\Delta K)^4}{G\sigma_y^2 U^*} \tag{2-11}$$

where G is the shear modulus.

The total plastic strain energy required to cause fatigue fracture of a material element at the crack tip after it enters the reversed plastic zone, is not constant but increases with decreasing plastic strain amplitude [60]. This variation is a result of the Coffin-Manson law [61, 62] for strain-controlled cyclic fatigue. Many authors [54-57, 63] attempted to use the Coffin-Manson law to derive analytical expressions for the fatigue crack growth rate. Most of these models contain material parameters that need to be determined experimentally or numerically. In a recent work of Chen et al. [57], the near crack tip elastic-plastic stress and strain were evaluated in terms of modified Hutchinson-Rice-Rosengren (HRR) formulations, with introduction of a fatigue blunting factor. An average damage per loading-cycle in the cyclic plastic deformation region is defined due to Coffin-Manson law and a theoretical model of FCG was developed by considering linear damage accumulation, given in equation (2-12):

$$\frac{da}{dN} = 2\frac{E\varepsilon_f'}{\sigma_{yc}}\frac{c+cn'}{c+cn'+1}r_{cy}\left[1-\left(\frac{\rho_c}{r_{cy}}\right)^{1+\frac{1}{c+cn'}}\right] \tag{2-12}$$

where σ_{yc} is the cyclic yield strength, E is the Young's modulus, n´ is the cyclic strain hardening exponent, ε_f' and c are the fatigue ductility coefficient and exponent given by Coffin-Manson law, r_{cy} and ρ_c are cyclic plastic zone and crack blunting radius respectively. Shi et al. [56], based on the critical plastic strain energy accumulated at the crack tip, proposed an analytical model presented in equation (2-13):

$$\frac{da}{dN} = \frac{\left(\Delta K^2 - \Delta K_{th}^2\right)^{1/2}}{4\pi(1+n')\sigma_{yc}^2 N^*} \tag{2-13}$$

where N^* is the number of cycles required for the crack to penetrate through the processing zone, $r_{cy} - \rho_c$, and can be defined as:

$$N^* = \frac{1}{2}\left[\frac{H'}{\left(\sigma_f' - \sigma_m\right)\varepsilon_f'}\left(\frac{\sigma_{yc}}{E}\right)^{n'+1}\frac{r_{cy}}{r_{cy}-\rho_c}\left[ln\left(r_{cy}\right) - ln(\rho_c)\right]\right]^{\frac{1}{b+c}} \tag{2-14}$$

In equation (2-14) H´ is the cyclic strength coefficient, σ_f' is the fatigue strength coefficient and σ_m is the mean stress. Equation (2-13) requires the determination of stress intensity threshold ΔK_{th}. In [64], a fatigue crack growth model is developed, which considers a strip plastic zone with material hardening at the tip of a crack. Crack growth is treated incrementally and corresponds to failure of material elements ahead of the crack tip under low cycle fatigue conditions. For constant amplitude loading, fatigue crack growth is described by:

$$\frac{da}{dN} = \frac{\pi}{32}\left(\frac{1}{2K_{cr}^2}\right)^{1/c}\frac{(\Delta K)^{2(1+1/c)}}{\sigma_y^2} \tag{2-15}$$

with K_{cr} being the critical stress intensity factor, σ_y the yield strength and c the fatigue ductility exponent.

2.3 Weld residuals stresses and fatigue crack growth

Residual stresses are present in many fabricated structures due to local plastic deformation from thermal and mechanical processes during weld manufacturing. Weld residual stresses are produced by thermal expansion, plastic deformation, and shrinkage during cooling. The

amount of constraint determines the amount of residual stresses. The intense heat associated with welding causes the region of the weld to expand. The surrounding material provides resistance to the expansion and subsequent contraction, generating residual stresses in the vicinity of the weld. Within the weld metal, residual stresses tend to be predominantly tensile in nature. The tensile residual stress field is self-balanced by compressive stresses induced in the parent metal [65]. A schematic view of the residual stress field (longitudinal and transverse) for a butt weld is shown in Figure 2.4. Through the thickness of the material, residual stresses may remain approximately constant with depth ("uniform" stresses) or they may vary significantly ("non-uniform" stresses). In sheet materials usually small variation in through-thickness residual stresses exists and assumption of uniform stresses may be considered.

<div align="center">(a)   (b)</div>
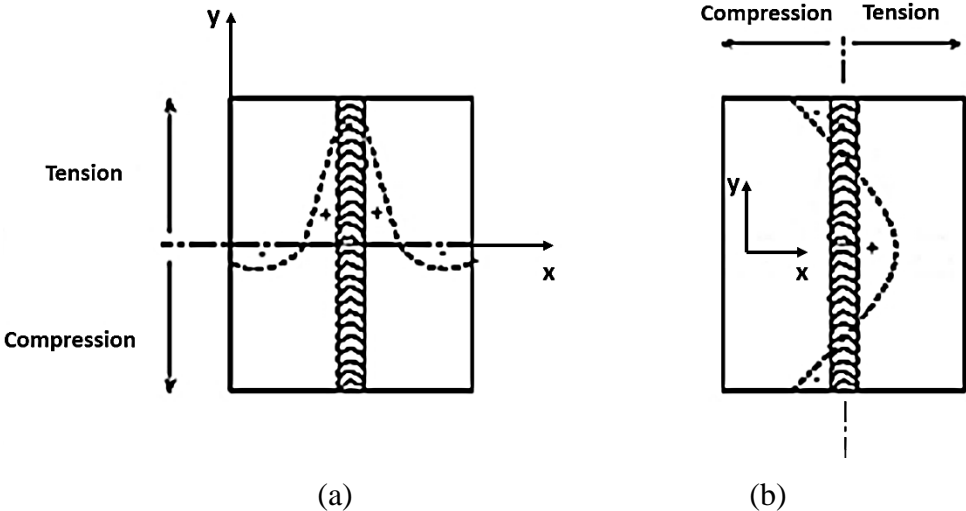
Figure 2.4 (a) Longitudinal (σ_y) and (b) Transverse (σ_x) residual stress field for a butt weld.

Tensile residual stresses have values in the magnitude of the material's yield strength and are detrimental for fatigue behavior of the structure, increasing the growth rate of the fatigue crack. Compressive residual stresses on the other hand decrease fatigue crack growth rate [66-68]. Therefore, accurate and reliable determination of residual stresses is essential for the assessment of structural integrity of welded components.

The main analytical approaches accounting for the effect of residual stresses on FCG rate, are the crack closure concept [26, 69-76] and the method of superposition [69, 72, 77-81]. They are used in combination with an appropriate fatigue crack growth model to describe how FCG rate is influenced by existing residual stresses.

2.3.1 Crack closure approach

The crack closure approach has been originally proposed by Elber [26] and was modified by Newman [73]. The effective stress intensity factor ΔK_{eff} corresponds to the range of the applied load cycle where the crack is open and can be calculated from equation (2-16):

$$\Delta K_{eff} = U\Delta K_{app} \tag{2-16}$$

where ΔK_{app} is the applied stress intensity factor range due to external loading and parameter U is expressed by:

$$U = \frac{1 - \sigma_{open}/\sigma_{max}}{1 - R} \tag{2-17}$$

where σ_{open} is the crack opening stress and σ_{max} is the applied maximum stress.

Several attempts have been made to develop simple analytical models of crack closure to calculate crack opening stresses σ_{open} [71, 73, 76]. Most of them were based on the Dugdale model [82] and have shown that σ_{open} is a function of stress ratio R, maximum stress σ_{max} and specimen thickness.

For a center crack tension specimen, $\sigma_{open}/\sigma_{max}$ has been calculated by Newman [73]:

$$\frac{\sigma_{open}}{\sigma_{max}} = A_0 + A_1 R + A_2 R^2 + A_3 R^3 \quad for\ R \geq 0 \tag{2-18}$$

$$\frac{\sigma_{open}}{\sigma_{max}} = A_0 + A_1 R \qquad for\ -1 \leq R < 0 \tag{2-19}$$

when $\sigma_{open} \geq \sigma_{min}$ (σ_{min} is the applied minimum stress). The coefficients A_o, A_1, A_2, A_3, are:

$$A_0 = (0.825 - 0.34\gamma + 0.05\gamma^2)[\cos(\pi\sigma_{max}/2\sigma_0)]^{1/\gamma} \tag{2-20}$$

$$A_1 = (0.415 - 0.071\gamma)\,\sigma_{max}/\sigma_0 \tag{2-21}$$

$$A_2 = 1 - A_0 - A_1 - A_3 \tag{2-22}$$

$$A_3 = 2A_0 + A_1 - 1 \tag{2-23}$$

For plane stress conditions $\gamma = 1$, while for plane strain conditions $\gamma = 3$. The value σ_0 is taken to be the average between the uniaxial yield stress and uniaxial ultimate tensile strength of the material.

2.3.2 Superposition approach

In the superposition approach, the maximum and minimum stress intensity factors $K_{max,total}$, $K_{min,total}$ derived from superposition of the external stresses and residual stresses are given by:

$$K_{max,total} = K_{max,app} + K_{res} \qquad (2\text{-}24)$$

$$K_{min,total} = K_{min,app} + K_{res} \qquad (2\text{-}25)$$

The stress intensity factor range ΔK and effective stress ratio R_{eff} are calculated from (2-26) and (2-27):

$$\Delta K = K_{max,total} - K_{min,total} = \Delta K_{app} \qquad (2\text{-}26)$$

$$R_{eff} = \frac{K_{min,app} + K_{res}}{K_{max,app} + K_{res}} \qquad (2\text{-}27)$$

In Figure 2.5a the stress intensity factor range resulting from superposition of an external constant amplitude and a tensile residual stress field is shown.

The total stress intensity factor range ΔK is not influenced from the residual stress field as indicated in equation (2-26). On the other hand, the effective stress ratio R_{eff} (equation 2-27) is affected. As a result, FCG rates under the influence of a residual stress field are a function of ΔK_{app} and R_{eff}.

$$\frac{da}{dN} = f(\Delta K_{app}, R_{eff}) \qquad (2\text{-}28)$$

K_{res} and R_{eff} change as the crack grows through the residual stress field and the growth rate can be obtained either from experimental data ($d\alpha/dN - \Delta K$) for a specific R_{eff}, or from crack growth equations including the stress ratio effect, such as the Forman, Walker equations [22, 23, 83].

In Figure 2.5b the stress intensity factor range resulting from the superposition of an

external constant amplitude and a compressive residual stress field is shown. A negative K_{res} value characterizes a closed crack. If the applied K value is greater than $|- K_{res}|$, then the crack will open.

(a)

(b)
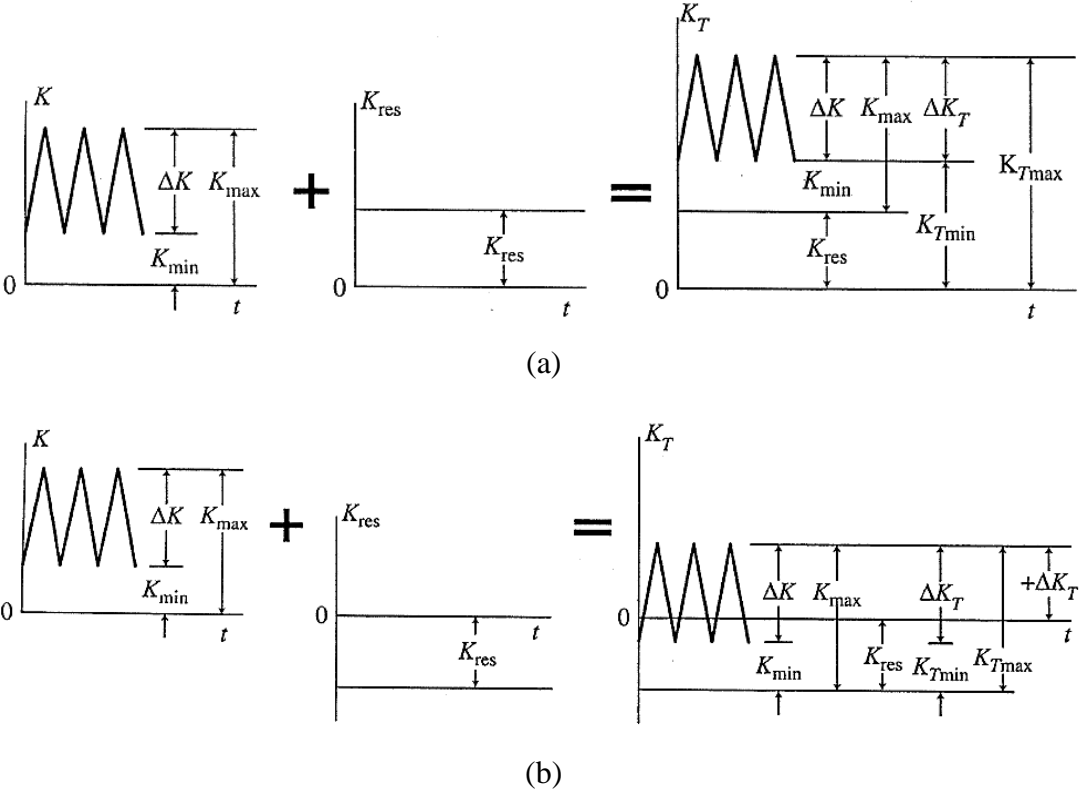
Figure 2.5 Stress intensity factor range resulting from superposition of external loading and residual stresses for (a) tensile K_{res}, and (b) compressive K_{res}.

2.3.3 Determination of the residual stress intensity factor (K_{res})

The calculation of the stress intensity factor K_{res}, is necessary for fatigue crack growth simulation within a residual stress field. The weight function method (WFM) and the fine element method (FEM) have been widely employed for calculating stress intensity factors. The WFM has been successfully used by many researchers for welded test samples [70, 75, 79, 84, 85]. Closed-form or approximate analytical solutions are available for calculating the K_{res} and in general the solutions are exact or accurate enough. However, most weight functions were developed for simple geometries or require finite width correction. Some weight functions are in complicated forms and the calculation process involves solving complex integral equations. On the other hand, the FEM is a more robust and versatile tool for complex geometries and loading conditions. The FEM has been successfully used in the fracture analysis in welds [75, 80, 81, 85]. This method is getting more popular due to the

rapid development of fast computers and implementation of fracture mechanics analysis routines in the commercial FE packages. Welded structural components have usually a complex geometry, for which FEM is more powerful than WFM in evaluating the effect of residual stresses on the crack tip stress field. In [75, 81, 85] a good agreement between WFM and FEM methods for evaluating stress intensity factors due to weld residual stresses was shown.

For the calculation of K_{res} a well-accepted method is the weight function, suggested by Bueckner [86]. For a two dimensional single edge crack element (Figure 2.6), with finite width (W) and infinite length, Bueckner's weight function is given by:

$$m(x, a) = \frac{2}{\sqrt{2\pi(a-x)}}\left[1 + m_1\left(\frac{a-x}{W}\right) + m_2\left(\frac{a-x}{W}\right)^2\right] \qquad \text{(2-29)}$$

where α is the length of the edge crack and parameters m_1, m_2 are:

$$m_1 = 0.6147 + 17.1844\left(\frac{a}{W}\right)^2 + 8{,}782\left(\frac{a}{W}\right)^6 \qquad \text{(2-30)}$$

$$m_2 = 0.2502 + 3.2899\left(\frac{a}{W}\right)^2 + 70{,}0444\left(\frac{a}{W}\right)^6 \qquad \text{(2-31)}$$
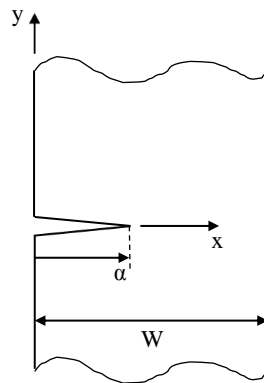
Figure 2.6 Single edge crack, infinite strip.

Using the product of equation (2-29) and the stress distribution $\sigma_y res(x)$ along the crack plane, the stress intensity factor K_{res} can be calculated from:

$$K_{res} = \int_a \sigma_y res(x) m(x, a) dx \qquad \text{(2-32)}$$

In equation (2-32), $\sigma_y res(x)$ is the stress distribution that would exist along the crack plane if the crack was not there (Figure 2.7).

It is worth noting that when using the weight function method, the implicit assumption is being made that the residual stress field does not diminish or redistribute with crack growth. This is a weak point of using the weight function concept since redistribution of residual stresses during fatigue crack propagation is a well-known problem [74, 87-89].
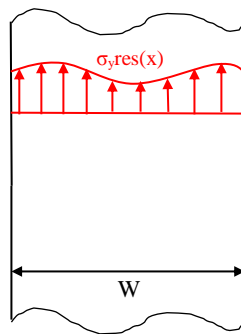
Figure 2.7 Infinite two dimensional strip with a residual stress distribution $\sigma_y res(x)$ along its finite width (W).

2.3.4 Fatigue crack growth in aluminum alloy welds

The propagation rate of a crack growing inside an aluminum weld material is a problem which has received significant attention by many scientists. Focus has been given mainly on the influence of residual stresses on fatigue crack growth rate and less on weld material characteristics.

In aluminum fusion welds, studies have focused on the importance of residual stress fields, microstructural influence and hardness levels on FCG [90-93]. The studies have shown that the residual stress field plays a dominant role in the mechanical performance. For cracks propagating perpendicular to the weld line, in the weld nugget where longitudinal tensile residual stresses exist crack growth rates were significantly greater than those found in the parent metal, while cracks initiating in the HAZ, subjected to compressive residual stress fields, showed lower crack growth rates [90]. Studies on fusion welds have suggested that effect of microstructure and associated hardness variation is small compared to that of the residual stresses, although some small effects have been demonstrated [67, 90, 94, 95].

In aluminum FSW, despite the lower heat input during welding compared to conventional fusion methods, significant microstructure variations and residual stress fields coexist in the

weld material. According to previous studies, FCG in FSW is intensely affected by (i) microstructure [70, 96-99], and (ii) residual stresses [70, 77, 96-101]. These parameters depend on the joined material types and the welding process [18, 102-106].

The majority of investigations however, focus on the aspect of residual stresses and the problem of weld microstructure on FCG has only slightly been investigated. John et al. [99] studied the effect of residual stresses on near threshold fatigue crack growth in friction stir welded 7xxx. Crack growth rates measured in the HAZ were lower than those of the base metal and residual stresses were found to play a significant role. In [107] friction stir welded 7xxx specimens with the crack placed parallel to the weld line, showed lower crack growth rates in the base metal than in the center of the weld but higher than in the HAZ. The decrease in FCG resistance in the weld-nugget was associated with an intergranular failure mechanism, while in the HAZ residual stresses were more dominant than the microstructure improving the fatigue crack growth resistance. Pouget et al. [70] studied the FCG behavior in 2050 AA FSW and found a strong correlation of fatigue crack propagation rate with the presence of residual stresses. At low ΔK values, the microstructure of the recrystallized weld nugget was found to influence the FCG behavior when the crack propagates parallel to the weld. Bussu et al. [101] and Fratini et al. [77] investigated independently the effects of microstructure and residual stresses on FCG of 2024-T351 friction stir welds. Residual stresses were mechanically relieved by plastic stretching. The authors claimed that when the crack propagates perpendicular to the weld line, crack growth behavior is dominated by the weld residual stresses, while microstructure has only a minor influence. In [70, 108], an attempt to describe FCG behavior was made with the use of empirical models. Pouget et al. [70] used the effective stress intensity factor, ΔK_{eff}, to predict FCG rates in 2050 AA FSW at low ΔK values. Goledtaneh et al. [108] attempted to model fatigue crack propagation in 2024-T351 FSW joint, using Walker [23] and Nicholls [47] fatigue models by incorporating the effects of residual stresses, stress relaxation and crack closure.

Chapter 3: Experimental procedure

In this Chapter the experimental methodology of the thesis is presented with a justification of the performed procedures. The experimental investigation is developed in three parts. The first part includes the friction stir welding experiments and analysis of weld microstructure. Friction stir welds have been produced and microstructural analysis has been performed in the parent and weld material. Microhardness measurements were conducted in the cross-section of the weld region and residual stress measurements perpendicular to the FSW line. In the second part the heat treatment experiments for the simulation of HAZ in parent 2024 material are analyzed. The aim of the simulation is to assess the mechanical behavior of a material with HAZ characteristics "free" from residual stresses, that are present in the weld material (Figure 1.2). For this purpose, an appropriate heat treatment procedure was developed that induces microstructural characteristics and local property variation similar to the HAZ in the parent material (Figure 1.3). In the third part the mechanical performance of the weld and heat treated materials is assessed. The experiments include tensile, fatigue crack growth and fracture toughness tests. A set of low cycle fatigue (LCF) tests was included in the investigation to assess the cyclic properties of the material with HAZ characteristics.

3.1 Material

Aluminum alloy (AA) 2024 in T3 condition, which includes solution heat treatment at $495^{o}C$, control stretching and natural aging, was selected for the experimental investigation. The 2024 AA is used extensively in commercial and military aircraft applications in the fuselage skin and wing skins. In the investigation, the material was used in sheet form with a thickness of 3.2mm. The nominal chemical composition of the alloy is presented in Table 3.1.

Table 3.1 Chemical composition (wt.%) of Aluminum alloy 2024 T3 [109]

| Al	Cu	Mg	Mn	Si	Fe	Cr	Zn	Ti	Other Each	Other Total
90.7 - 94.7	4.35	1.5	0.6	max. 0.50	max. 0.50	max. 0.10	max. 0.25	max. 0.15	max. 0.050	max. 0.15

3.2 Friction stir welding (FSW) experiments

For the welding of specimens, a custom friction stir welding system was used (Figure 3.1a) by converting a milling machine to an FSW application with appropriate modifications.

The modifications were made collaboratively by the Laboratory of Materials and Laboratory of Mechanics & Strength of Materials of the University of Thessaly. They included manufacturing of a welding tool, clamping fixtures, and mounting of a load cell with a capacity of 2000kg and special indicators in order to control the welding parameters (tool pressure, tool rotation speed and welding speed) during the welding process. The welding tool has a shoulder diameter of 14mm, a cylindrical pin with diameter 3mm and height 2.8mm as shown in Figure 3.2. It is made of H13 steel, with a hardness value of 53 Rockwell C.

(a)   **(b)**
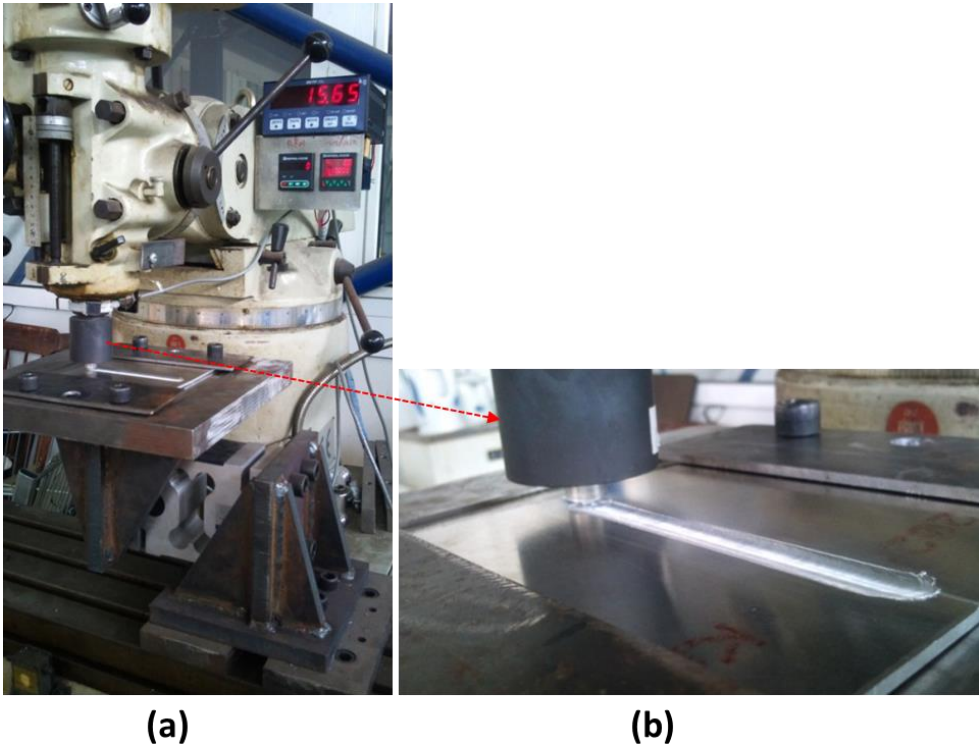
Figure 3.1 (a) Friction Stir Welding system (b) Friction stir welding process of 2024 T3 AA sheet.
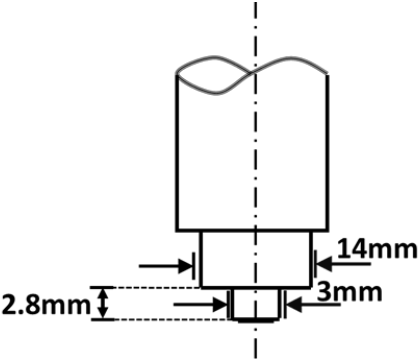
Figure 3.2 Weld tool dimensions.

FSW welds were performed in 2024 T3 AA transverse to the rolling direction (L-T direction). The sheet dimensions were 100x100x3.2mm and the welding parameters were:

➢ Tool rotation speed V_r: 830rpm
➢ Welding speed V_f: 70mm/min
➢ Tool pressure: 8kN
➢ Nuting angle θ: 1°
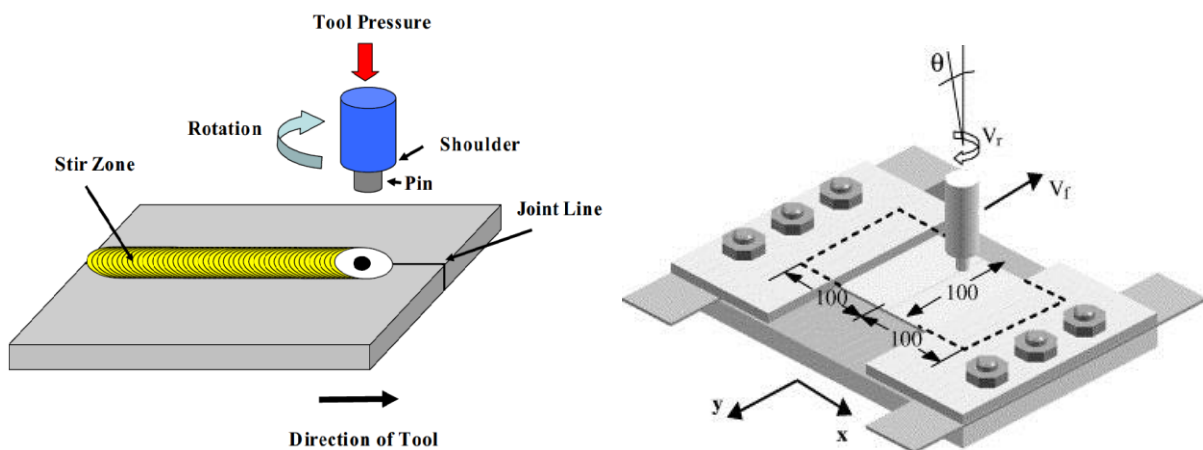
Figure 3.3 Graph with the parameters of FSW procedure.

In total 26 welds were prepared and used for metallographic analysis, microhardness measurements, residual stresses measurements and mechanical testing.

3.3 Heat treatment for simulation of the Heat Affected Zone (HAZ)

The HAZ microstructure was simulated in parent 2024 AA in order to investigate its influence on fatigue crack growth performance without the weld residual stresses. Simulation of the HAZ microstructure is complex due to occurring temperature gradients during the welding process, which produce gradual changes in the microstructural characteristics and mechanical properties. Since the material in the HAZ is in overaged state, an appropriate overaging treatment was used to produce a 2024 microstructure with HAZ characteristics.

For the selection of heat treatment conditions, the overaging curves of the material were determined, which relate the reduction in hardness to the aging temperature and time. A heat treatment furnace (Thermawatt TGT 50) with maximum heating capacity of 1200^oC was used capable of maintaining a temperature accuracy of $\pm1^o$C during treatment. Small samples were placed inside the furnace and were artificially aged at temperatures ranging from 150^oC to

300°C for time periods up to 48 hours. Subsequently, the overaging curves were used to obtain the microhardness variation with regard to aging parameters.

Two types of heat treatment were performed: i) uniform overaging heat treatment, and ii) overaging heat treatment with exposition of the samples to a temperature gradient.

The conditions (temperature and time) for the uniform heat treatment were selected carefully to produce material hardness similar to the positions 1, 2, 3 in the HAZ (Figure 3.4). The temperatures were 200°C, 250°C and 300°C for 15hours.
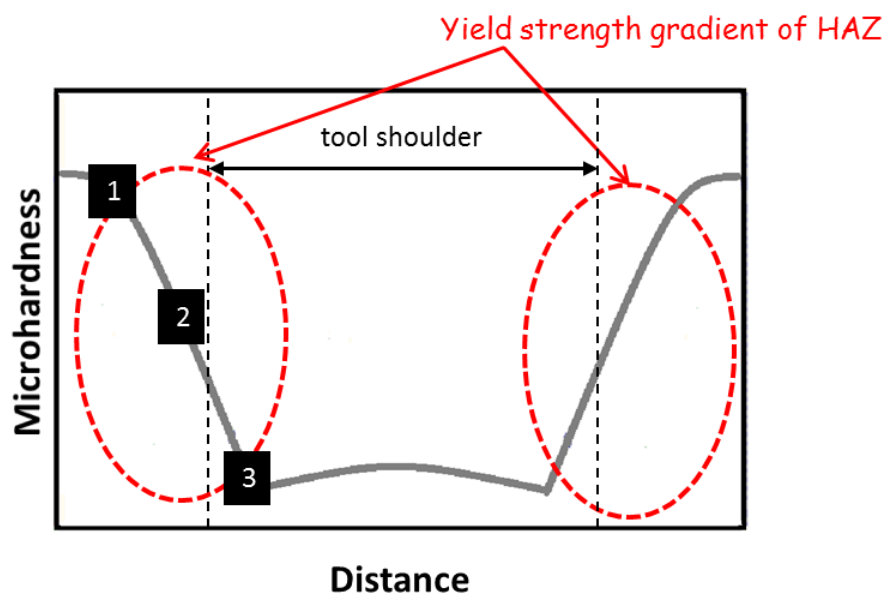
Figure 3.4 Locations in the HAZ which were simulated with heat treatment process (points 1, 2, 3).

In the second type of heat treatment, samples with dimensions of 150x100mm (Figure 3.5) were exposed to a temperature gradient. The temperature boundaries were the limits of areas (W1-W3) and (W2-W3) in the specimen of Figure 3.5. The heat treatment set up (Figure 3.6a) consists of two tanks filled with industrial oil (Figure 3.6b). The oil inside the tanks is heated by electric heating elements. The temperature is controlled by thermocouples connected to special controllers that are shown in Figure 3.6c. By placing parts W1 and W2 (Figure 3.5) in the cavity of the tanks (Figure 3.6b), they maintain the desired temperature. In part W3, the surface of the specimen is insulated with rockwool (Figure 3.6d).
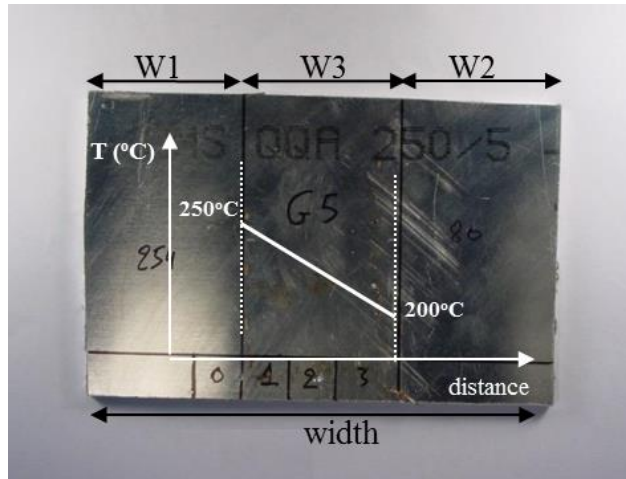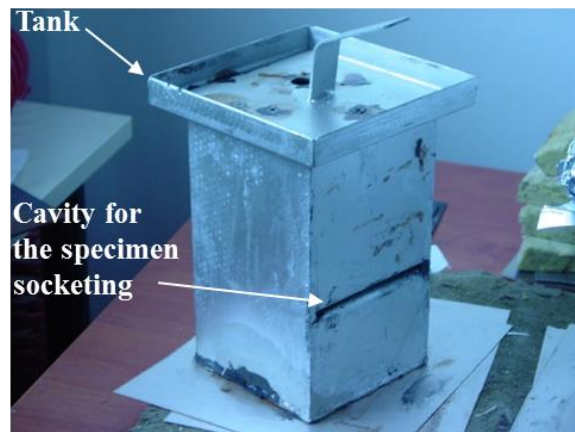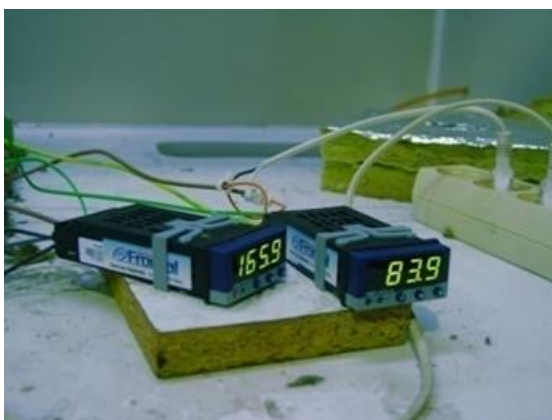
Figure 3.5 Material sample showing the areas W1 and W2 which are exposed to different temperatures and section W3 with resulting temperature gradient.
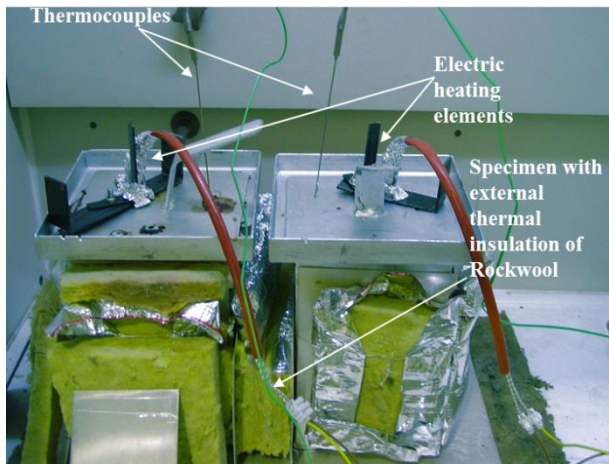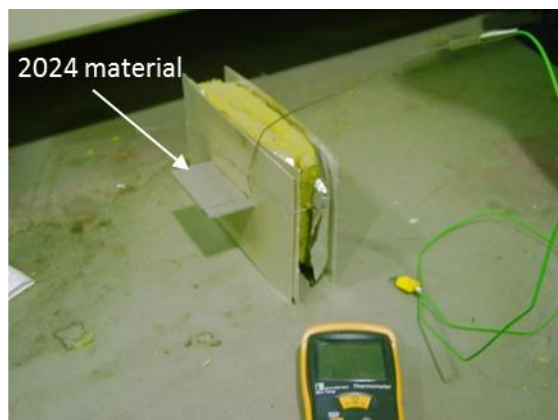

(a)

(b)

(c)

(d)

Figure 3.6 (a) Equipment for exposition of the samples to a temperature gradient (b) oil tank (c) Thermal heat controllers (d) Insulation of 2024 material and installation of thermocouple for monitoring the temperature of the specimen during heat treatment.

According to Fourier's Law of heating conduction (equation 3-1) [110], in an externally thermally insulated material between two constant temperature boundaries, the variation of the temperature inside the boundaries is a linear relation between the temperature of the boundaries (Figure 3.7).

$$T_H = \frac{q}{kA}L + T_c \qquad (3\text{-}1)$$

where q is the heat transferred within the medium per unit time, A is the heat transfer area, k is the thermal conductivity of the material, T_H is the higher temperature, T_C is the lower temperature and L is material thickness.
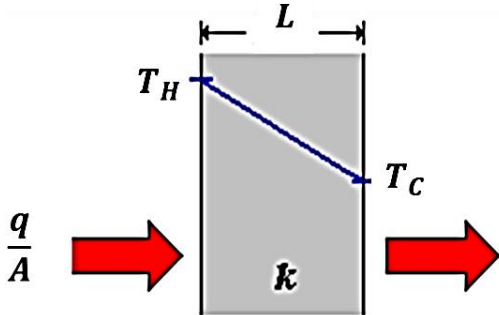
Figure 3.7 Schematic representation of Fourier's Law of heating conduction, showing a linear temperature gradient between two constant thermal boundaries.

During heat treatment, the temperature was kept constant at the two temperature boundaries 200 and 250°C. Two more thermocouples were attached on part W3 in order to check the accuracy of the applied temperatures (Figure 3.6d). In total, 6 specimens were subjected to the temperature gradient in order to produce material with variation in hardness.

3.4 Microstructural analysis

Microstructural analysis of the friction stir welds was performed using optical microscopy. Small samples were extracted from the weld zone (including nugget, HAZ, TMAZ, BM) with dimensions 3.2x50x20mm. Preparation of the samples for metallographic examination was made by incremental grinding with 120-, 500- ,800-, 1000-grit silicon-carbide papers and polishing with diamond (3 and 1 μm) and alumina before etching. The specimens were etched with Keller's reagent, which consists of 2 mL HF, 3 mL HCl, 5 mL HNO_3 and 190 mL H_2O.

Microstructural analysis was also conducted in the heat treated material to evaluate the similarity of microstructural characteristics between heat treated alloy and HAZ.

3.5 Microhardness measurements

Microhardness measurements were performed in accordance with ASTM E92 standard [111], in the cross-section of the weld region. The microhardness values were measured along a distance of ±15mm from the weld centerline, at depths of h=1mm and 2mm from the surface, with a constant step of 25μm between two consecutive measurements. The Vickers scale was used and hardness values were determined using an applied force of 200gr ($Hv_{0.2}$) for 10 sec. In total 500 measurements were performed for the determination of hardness profile.

3.6 Measurement of residual stresses

Residual stresses were measured in the direction of the weld line (y-direction, Figure 2.4) with the use of the hole-drilling method. For the measurements the hole-drilling equipment of the Laboratory of Technology and Strength of Materials of University of Patras was used in accordance with ASTM E 837-08 [112]. Residual stresses were determined using a rectangular strain gauge rosette (type EA-062RE-120), that includes 3 gauges situated at angles 0^0, 90^0, -135^0 with respect to y axis (Figure 3.8a). The procedure included: i) cleaning of the area with Vishay CSM-2 solvent, ii) grinding with 320- and 400-grit silicon-carbide paper for removal of possible surface irregularities or oxides, iii) abrading with 400-grit wetted with Vishay M-Prep Conditioner A, iv) application of Vishay M-Prep Conditioner A and Vishay M-Prep Neutrilizer 5A on the specimen, scrubbing with a cotton-tipped applicator and careful drying of the surface. Attachment of the rosette was achieved with the use of Vishay M-Bond 200 glue.

Incremental drilling of the hole at the rosette center was made with a 0.1mm step using a Vishay RS-200 Milling Guide (Figure 3.8c) and a cutter with a diameter of 1.6mm. The strain gauge values during drilling were monitored with the strain indicator Vishay P3 (Figure 3.8d).

Residual stresses were measured perpendicular to the weld line along a width of ±25mm from the weld center. In total, 20 measurements were made for the determination of the residual stress profile.

The amount of relaxation of residual stresses after cutting of the specimen from the welded plate was determined with additional measurements on a smaller panel of 75x72 mm,

machined from the initial welded plate of 100x200 mm (Figure 3.9).

(a)   (b)

(c)   (d)
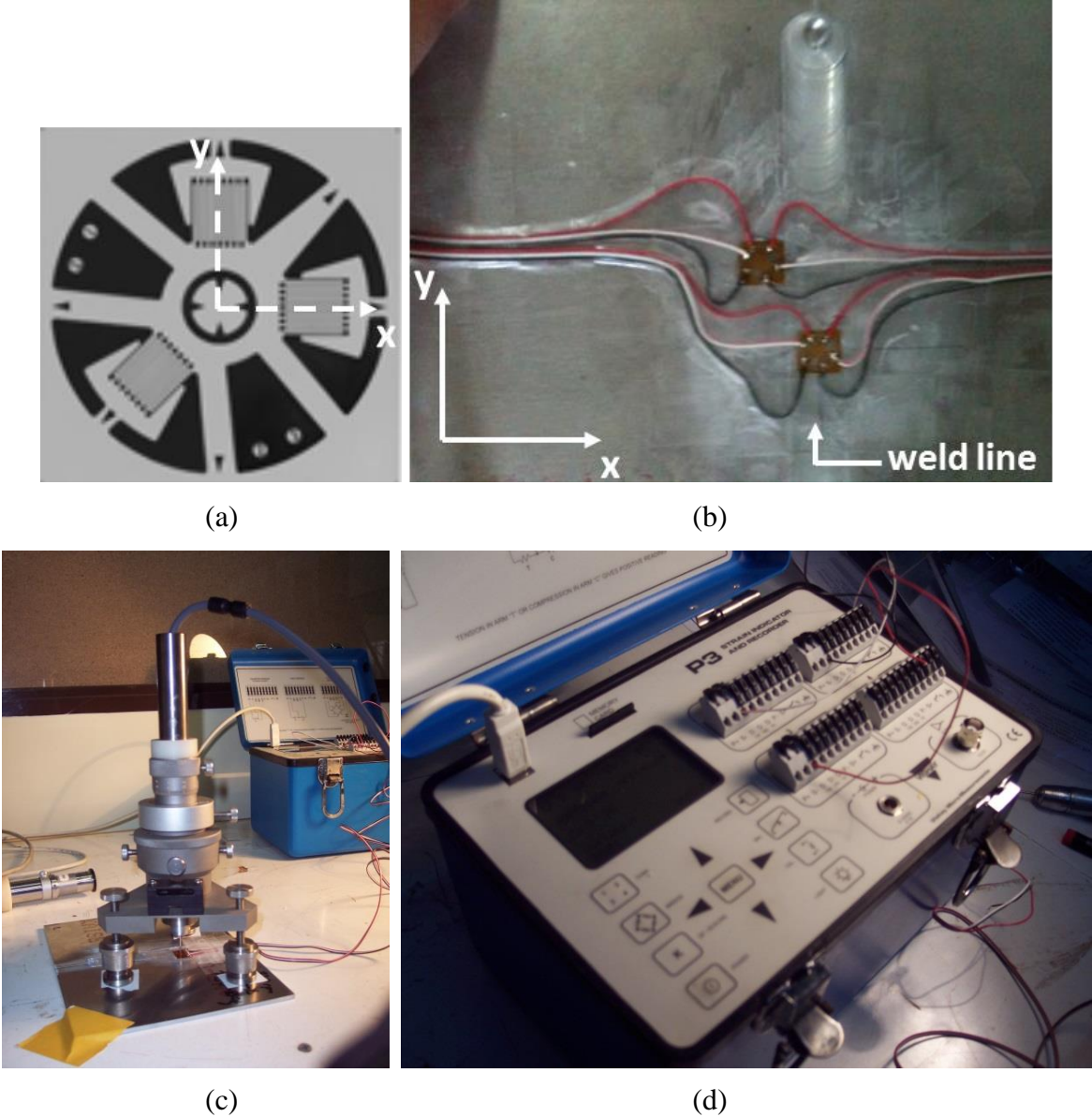
Figure 3.8 (a) Rosette used for residual stress measurements (b) Attachment of a strain gauge rosette on a friction stir weld (c) hole drilling equipment and (d) strain indicator used for analyzing residual stresses.
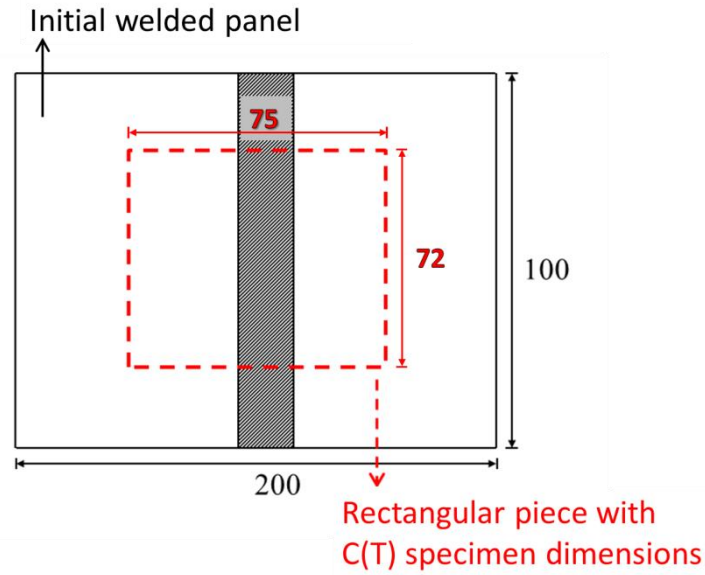
Figure 3.9 Dimensions (in mm) of C(T) specimen used for FCG test compared to the dimensions of the initial panel.

3.7 Mechanical testing

The investigation of mechanical performance was made for FSW material, material under uniformly heat treated conditions and material with hardness (strength) gradient. In Table 3.2 the type of mechanical tests performed for each material condition is presented.

Table 3.2 Type of mechanical tests performed for each material condition

Material condition	Tensile	FCG	Fracture toughness	Strain controlled
Parent metal (2024 T3)	✕	✕	✕	✕
FSW	✕	✕		
Uniformly heat treated	✕	✕	✕	✕
Material with hardness gradient		✕		

3.7.1 Tensile tests

The mechanical properties in the weld region were determined using subsize specimens (Figure 3.10) in accordance with ASTM E8M-01 specification [113]. A 100kN servo-hydraulic machine was used to perform the tensile tests at room temperature with a constant displacement rate of 0.5mm/min.

The specimens were extracted from the weld nugget, TMAZ and HAZ (Figure 3.11). A

more detailed explanation of the exact specimen location where specimens have been extracted from the weld is given in paragraph 4.3.1.1.

In the case of uniformly heat treated material, tensile tests were carried out in L and L-T material directions. Two specimens were tested in each case and average values of properties were obtained.
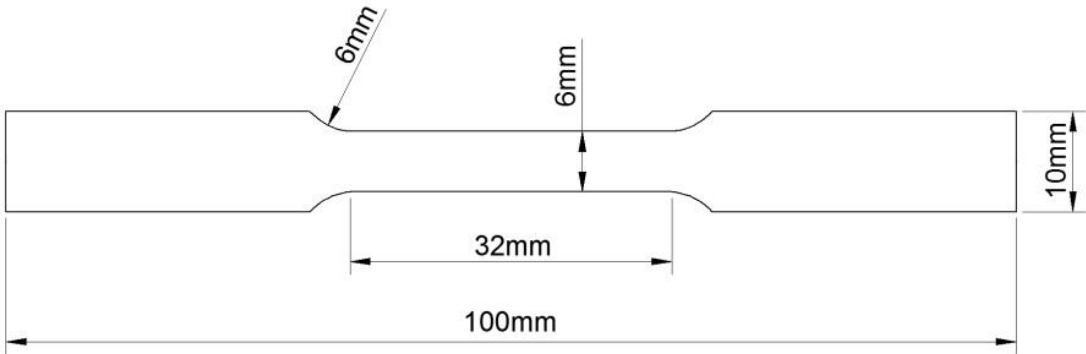
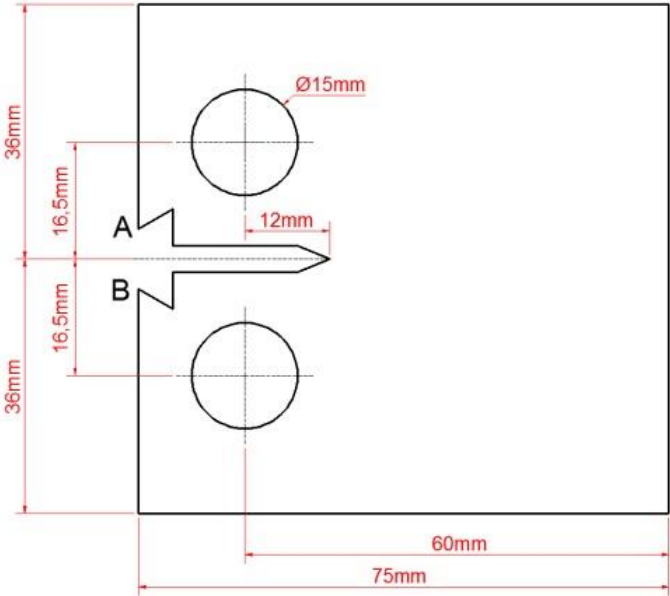**Figure 3.10** Subsize specimen configuration according to specification ASTM E8M-01.
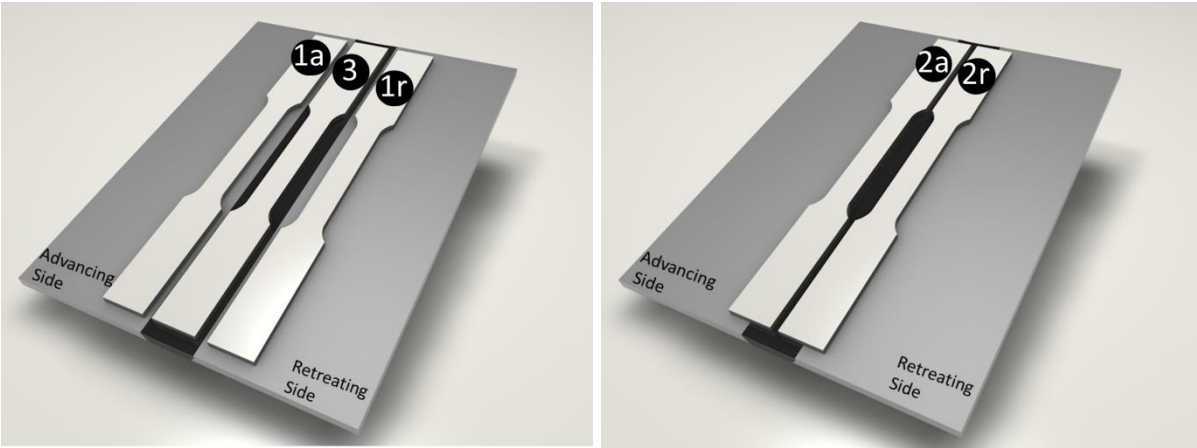
Figure 3.11 Locations where specimens have been extracted from the weld region

3.7.2 Fatigue crack growth (FCG) tests

The fatigue crack propagation tests were carried out on compact tension C(T) specimens (Figure 3.12) in accordance with ASTM E647-00 [114] on a 100kN servo-hydraulic fatigue machine at room temperature. The notch was machined parallel to the material rolling direction. The maximum stress was σ_{max}= 10MPa, the stress ratio R=0.1 and the frequency 5Hz. Crack growth rates were measured in the intermediate ΔK region ranging from 11 to 25 MPam$^{1/2}$. For the determination of crack length, the crack opening displacement (COD) was measured at points A, B of Figure 3.12 with the use of a COD extensometer. Subsequently, data evaluation was performed with implementation of the compliance method. Crack closure

during testing was measured to determine the minimum force at which the crack is open during cyclic loading. The measurements were performed using the compliance method according to ASTM E647-00 [114]. Experiments were conducted in FSW material, uniformly heat treated material and materials with hardness gradient.

In the FSW, fatigue crack growth characteristics were examined in mode I loading transverse to the weld line. Three different configurations (FSW#1, FSW#2, FSW#3) were examined, with different notch tip positions with regard to the weld centerline (Figure 3.14). In FSW#1 the initial notch tip is placed in the advancing side, 17mm from the weld centerline, in FSW#2 in the advancing side, 7mm from the weld centerline and in FSW#3 at the weld centerline. Two FCG tests were carried out for each configuration.

Figure 3.12 C(T) specimen configuration according to specification ASTM E 647-00.
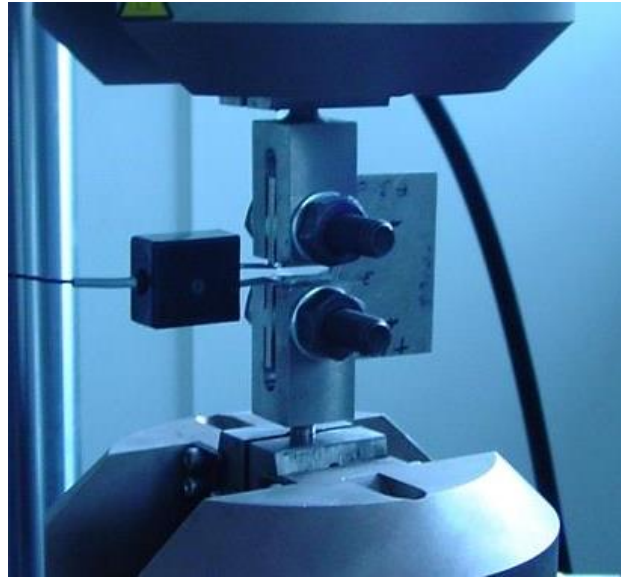
**Figure 3.13** Fatigue crack growth test setup.
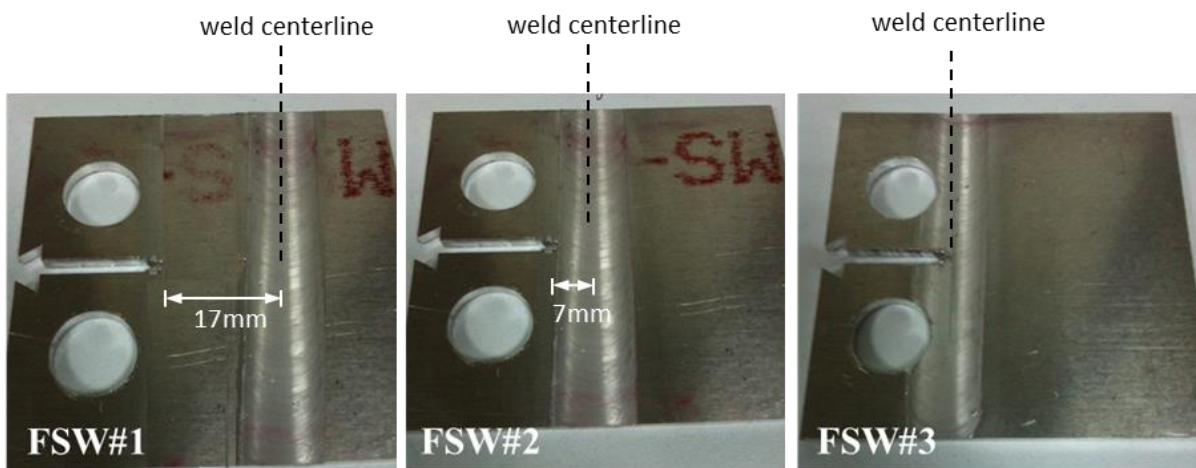
Figure 3.14 FSW#1, FSW#2 and FSW#3 specimen configurations.

In the uniformly heat treated material, 17 FCG tests were carried out, 6 in T3 condition, 3 in material heat treated at $200^{o}C$, 6 in material heat treated at $250^{o}C$ and 5 in material heat treated at $300^{o}C$. Crack closure measurements were also conducted.

In the material with hardness gradient a positive and negative hardness gradient at the crack tip were examined. The C(T) specimens were appropriately machined so that the notch tip coincides with the boundary of hardness gradient (Figure 3.15). For each case, 3 FCG test were carried out.

(a)   (b)
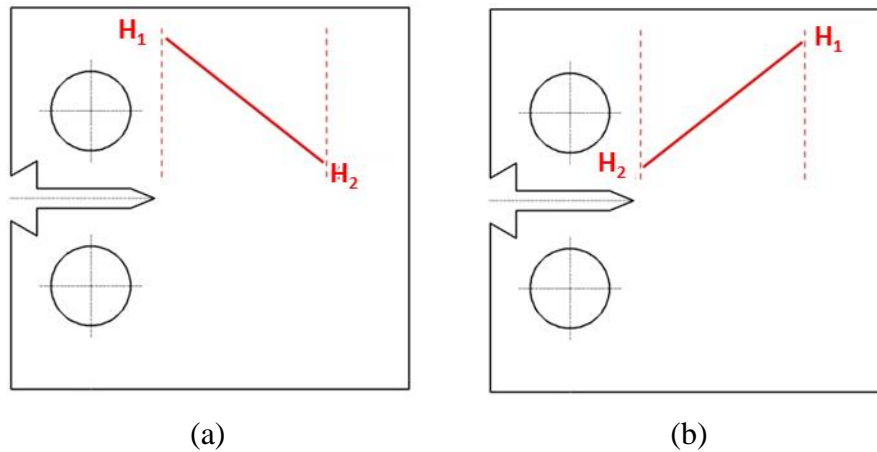
Figure 3.15 C(T) specimen with (a) positive and (b) negative hardness gradient in front of
notch tip resulting from heat treatment

3.7.3 Fracture Toughness tests

Fracture toughness tests were performed on C(T) specimens (Figure 3.16) in accordance
with ASTM E561-98 [115]. The maximum mode I stress intensity factor (K_{max}) was
determined, which complies with LEFM conditions in the test. In order to prevent buckling of
the specimen, an anti-buckling device was used during the tests (Figure 3.17).
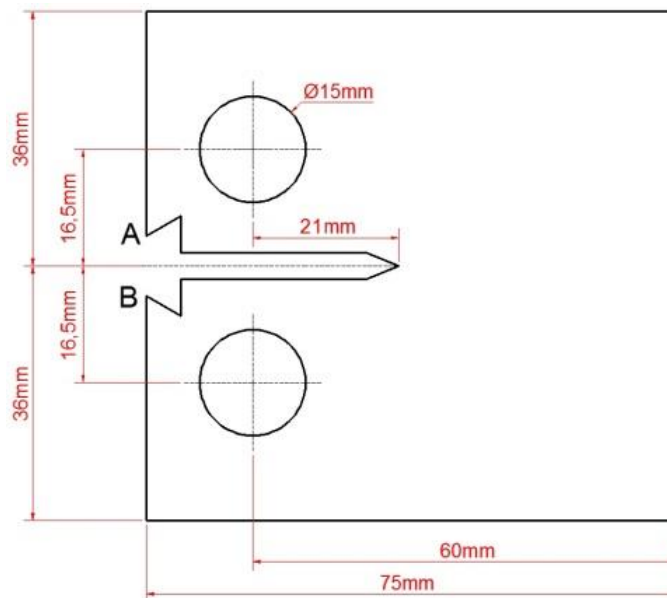
**Figure 3.16** C(T) specimen configuration according to specification ASTM E561-98.
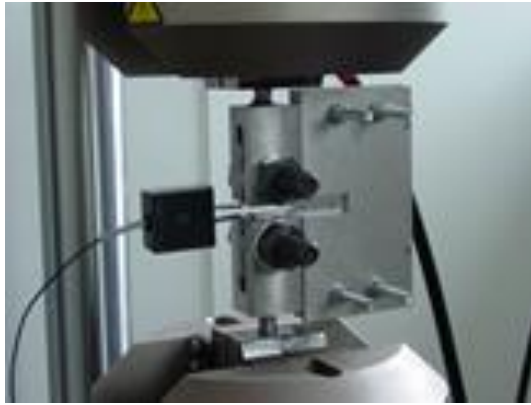
Figure 3.17 Anti-buckling device used in fracture toughness test.

3.7.4 Strain controlled fatigue tests

The strain controlled fatigue tests were conducted in accordance with the guideline SEP 1240 [116] with the specimen configuration shown in Figure 3.18. For the experiments a strain ratio of R= -1 and a frequency of 0.2 Hz was used and the applied strain amplitude was measured with a dynamic axial clip-on extensometer. To prevent buckling during testing, an anti-buckling (Figure 3.19) was attached to the specimen surfaces.
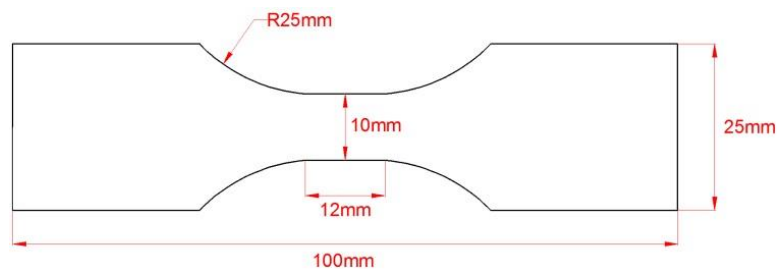
Figure 3.18 Specimen configuration according to specification SEP 1240.
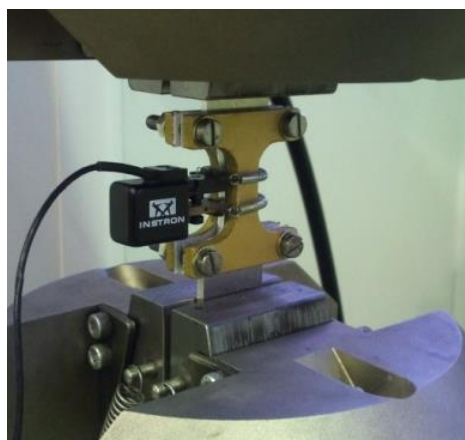
Figure 3.19 Strain controlled fatigue test setup with the use of anti-buckling device.

Chapter 4: Experimental results

In this Chapter, the experimental results are presented, which include: i) microstructural analysis and microhardness measurements ii) mechanical testing (tensile, strain controlled cyclic tests, fracture toughness and fatigue crack growth tests) iii) determination of residual stresses in direction perpendicular to the weld line.

## 4.1 Microstructural analysis and microhardness measurements

4.1.1 FSW material

The cross section of the 2024 T3 friction stir weld shown in Figure 4.1 reveals the heat affected zone (HAZ), the thermo-mechanically affected zone (TMAZ) and the weld nugget. Adjacent to the HAZ, the base metal (BM) is unaffected and consists of the 2024 T3 microstructure shown in Figure 4.2. SEM/EDS analysis showed that the BM includes three types of inclusions: (i) Al-Cu (ii) Al-Cu-Fe-Mn, and (iii) Al-Cu-Fe-Si-Mn containing particles. The results are in agreement with [109, 117, 118]. The 2024 T3 microstructure is characterized by two major second-phase particles, namely the Al_2Cu (θ' phase) and the Al_2CuMg (S´ phase) [117].

In micrographs of Figure 4.1 the weld zone microstructural characteristics are presented. In the HAZ, coarsening of metastable phases due to overaging is observed, while in the TMAZ, the original elongated grains have been plastically deformed by the tool during the welding process. The nugget zone consists of a fully recrystallized microstructure, where the original grains have been replaced with fine, equiaxed, recrystallized grains with smaller mean diameter compared to the base metal.
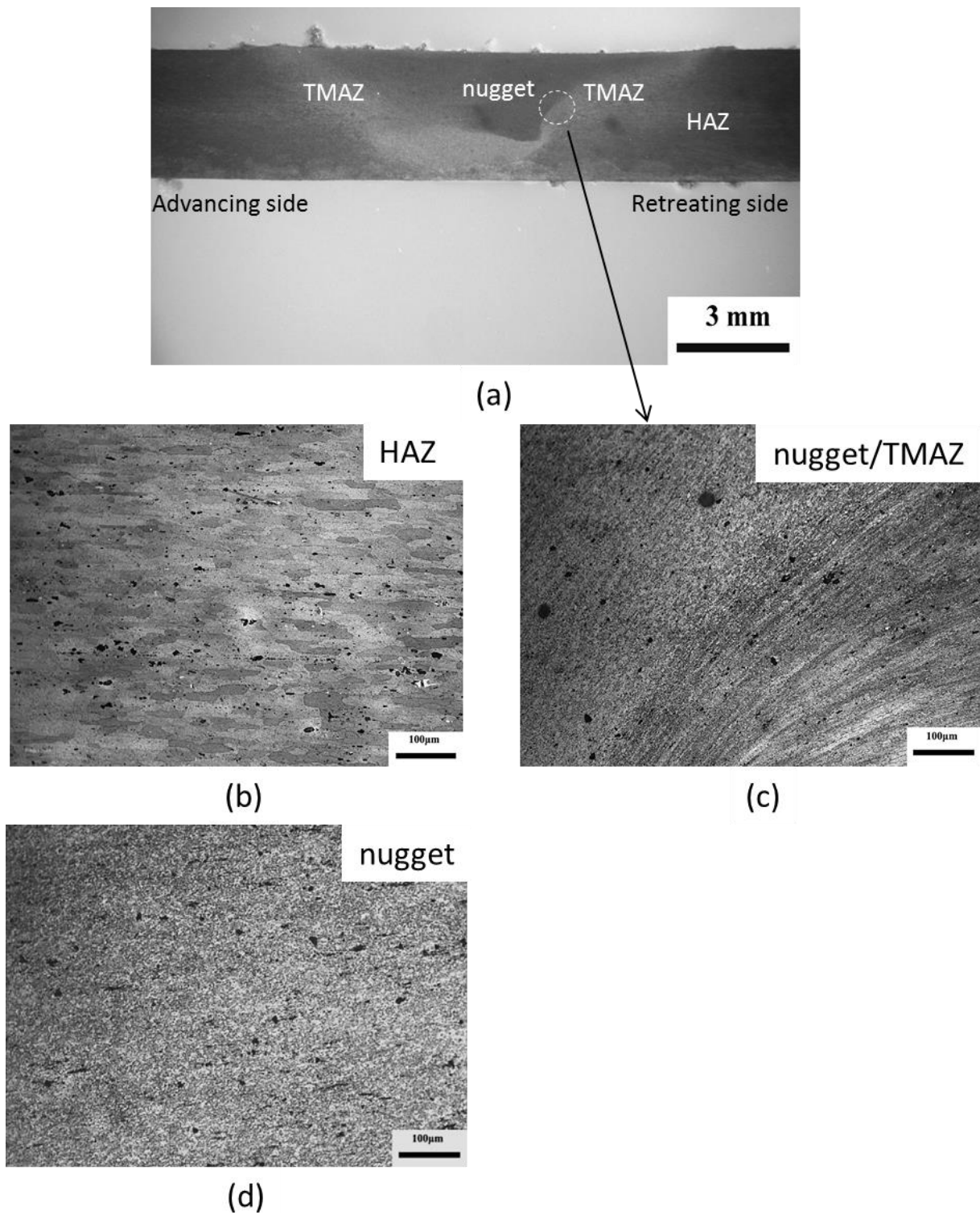
Figure 4.1 Microstructural details of the weld zones in 2024 T3 FSW: a) cross section of the weld joint, b) HAZ c) nugget and TMAZ boundaries b) weld nugget.
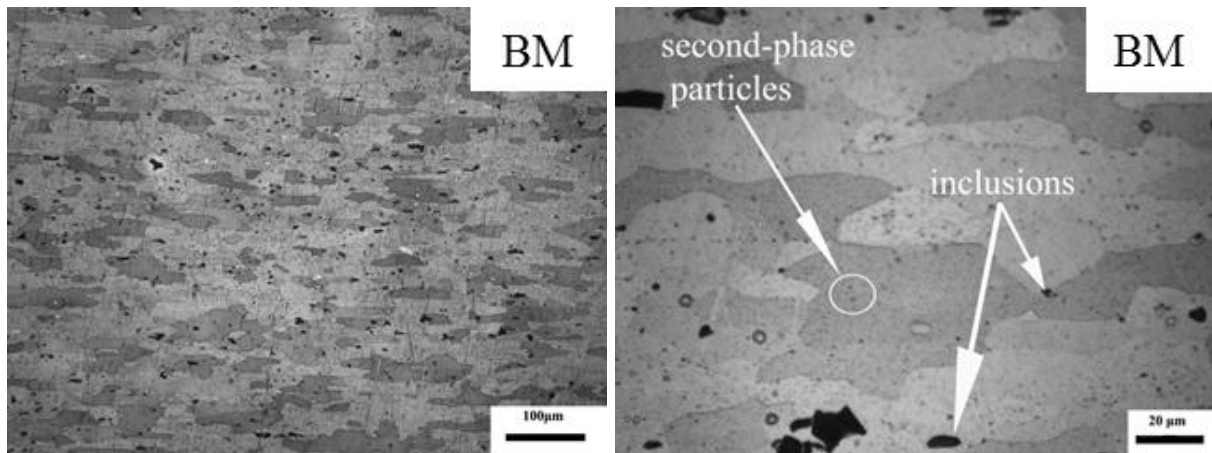
**Figure 4.2** Microstructure of the base 2024 T3 material.

In Figure 4.3 the microhardness values along a cross section of the weld at 1mm and 2mm depth from the weld surface are shown. The microhardness variation has the typical W-shape, present in friction stir welds in precipitation hardened aluminum alloys [3, 119, 120]. In the weld nugget an average drop in hardness of 20% compared to the base metal is observed, which has a hardness of 150 $HV_{0.2}$. The highest drop in hardness was 35% compared to the BM and occurred in the TMAZ. In the HAZ, a hardness gradient exists, with upper and lower limit values of the BM and TMAZ respectively. In the HAZ, softening is observed due to precipitate coarsening (overaged state), accompanied by a steep drop in hardness when moving from the HAZ to the TMAZ. During the welding process, the temperature in the HAZ varies with the distance from the weld centerline. In positions closer to the weld, higher temperatures are reached, that lead to a high reduction in hardness. In the TMAZ, a minimum hardness value is reached as a result of the plastically deformed structure, as well as occurring aging processes. In the weld nugget coarsening and dissolution of precipitates takes place, associated with microhardness reduction, which closer to the weld line center, is followed by a strength recovery due to natural aging.
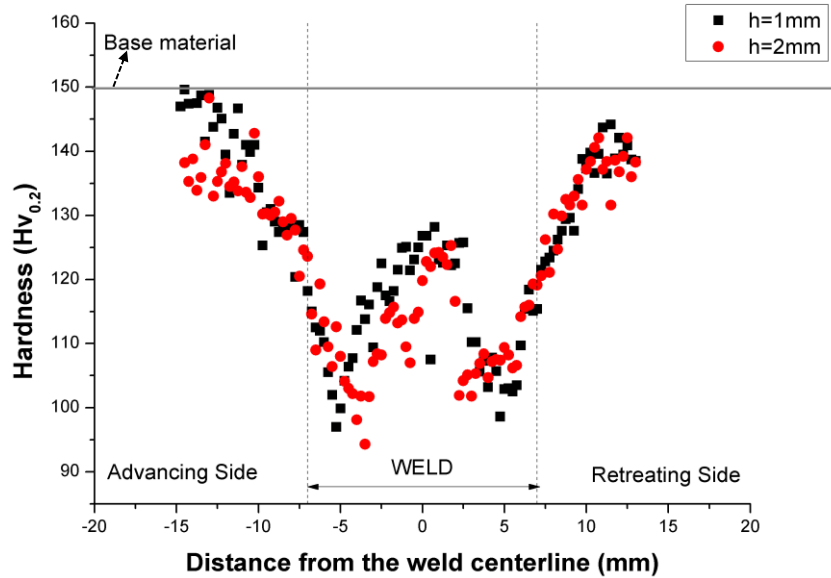
Figure 4.3 Microhardness variation in the weld region determined at two different layers in the cross section of the FSW joint (1 and 2 mm depth from specimen surface).

4.1.2 Uniformly heat treated material

The overaging curves used to select the heat treatment conditions ($200^{o}C$, $250^{o}C$ and $300^{o}C$ for 15 hours) are shown in Figures 4.4a and 4.4b. In Figure 4.4a, the microhardness variation with temperature and heat treatment duration is shown. The microhardness value in the initial T3 state was measured at 150 $Hv_{0.2}$, which is in agreement with [109]. Until $200^{o}C$, no significant drop in hardness is observed with increasing aging time. Above $200^{o}C$, the drop in hardness stabilizes after approximately 15 hours. The maximum decrease in hardness was 50% compared to the T3 state, at $300^{o}C$ for 15 hours. In Figure 4.4b, the hardness-temperature diagram for constant aging times of 10 and 15 hours is presented. A gradual, almost linear decrease of microhardness between the temperature boundaries of $200^{o}C$ and $300^{o}C$ is observed. This hardness gradient between 150 and 75-80 $Hv_{0.2}$ is similar to the microhardness gradient observed in the HAZ (see Figure 4.3).
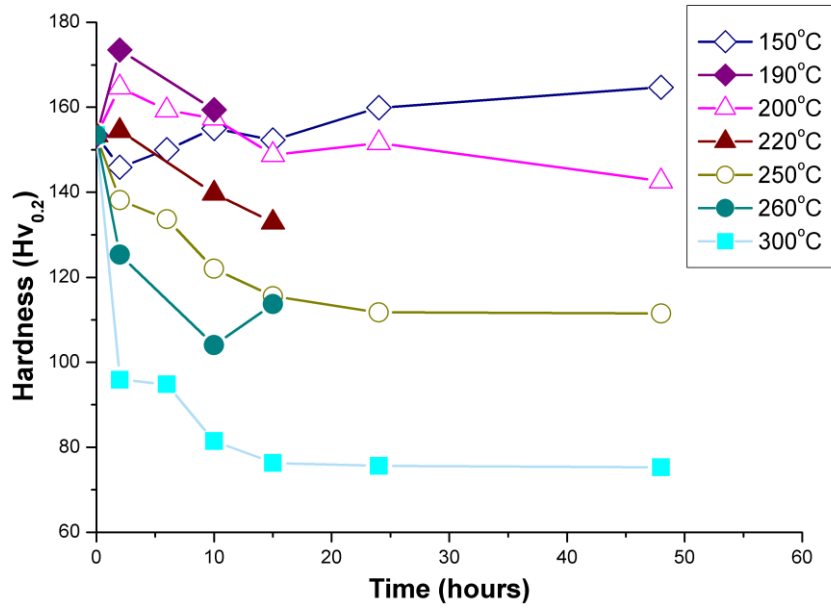
(a)
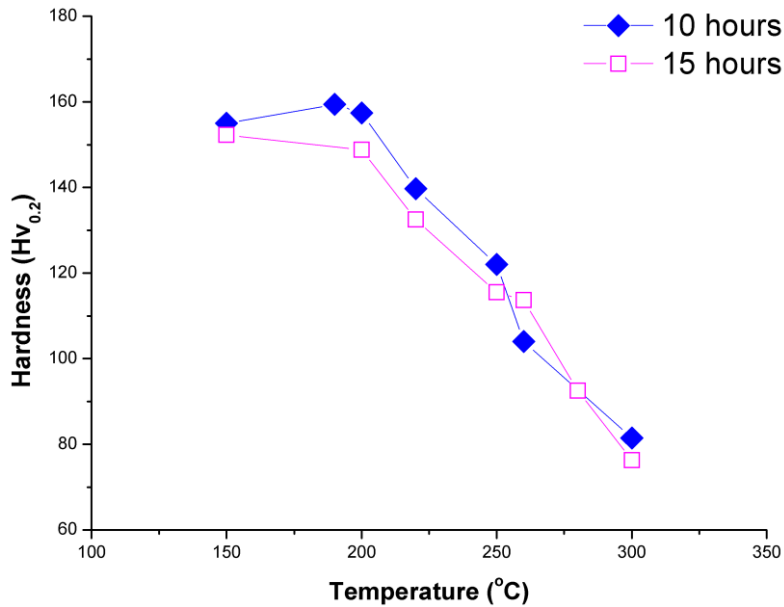
(b)

Figure 4.4 Overaging curves of 2024 T3 aluminum alloy: (a) Hardness-Time diagram for different aging temperatures (b) Hardness-Temperature diagram for constant duration of 10 and 15 hours treatment.

Based on the previous observation the two temperatures (200 and 300°C), as well as the intermediate value of 250°C were selected as aging conditions for the simulation of HAZ. The aging time of 15 hours was chosen as the threshold beyond which, no significant hardness change was observed (Figure 4.4a). The materials produced from T3 state with aging at 200°C, 250°C and 300°C for 15 hours, are referred to as A200, A250 and A300

materials respectively and have similar microhardness values with the HAZ material in the positions 4mm (A300), 7mm (A250) and 14mm (A200) with respect to the weld centerline as presented in Figure 4.5.
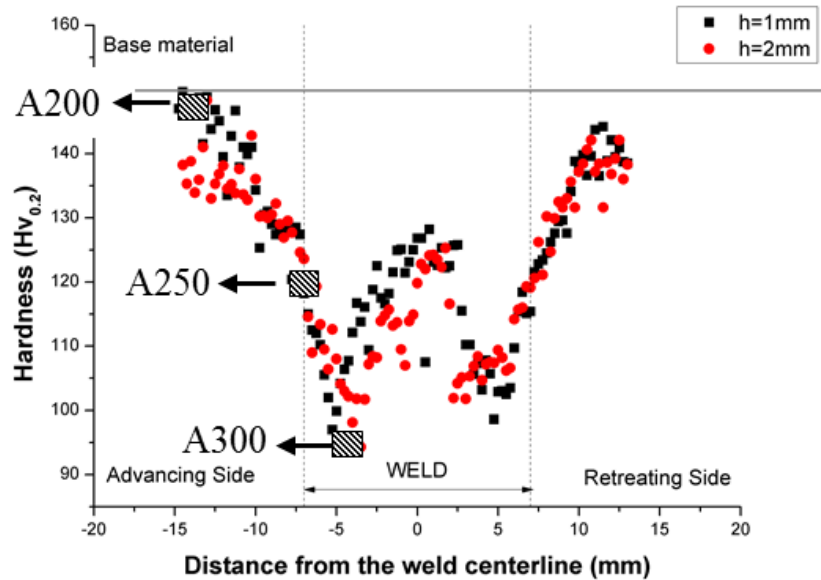
Figure 4.5 Microhardness values of A200, A250 and A300 materials in correlation with HAZ hardness values measured at depths of h=1mm and 2mm from the weld surface.

In Figures 4.6 a-d the produced microstructures in materials A200, A250 and A300 are displayed together with a micrograph of the HAZ microstructure taken 12mm from the weld centerline. The HAZ microstructure of Figure 4.6a has very similar characteristics with the heat treated material A200 (Figure 4.6b), which corresponds to the same position in the gradient (Figure 4.5). At regions of the HAZ closer to the weld nugget the characteristics start to differentiate (heat treated materials A250 and A300). Inside the grains coarsening of the metastable phases can be observed, while inclusions seem to be unaffected with regard to the parent metal (Figure 4.2). Coarsening of metastable phases in the alloy A300 is more pronounced compared to A200 and A250. The above observation is consistent with the lower hardness values of A300 compared to A200 and A250. Moreover, in A250 and A300 precipitate-free zones (PFZs) are evident, where metastable phases have dissolved from the grain boundaries and precipitated in the region around the grain boundaries.
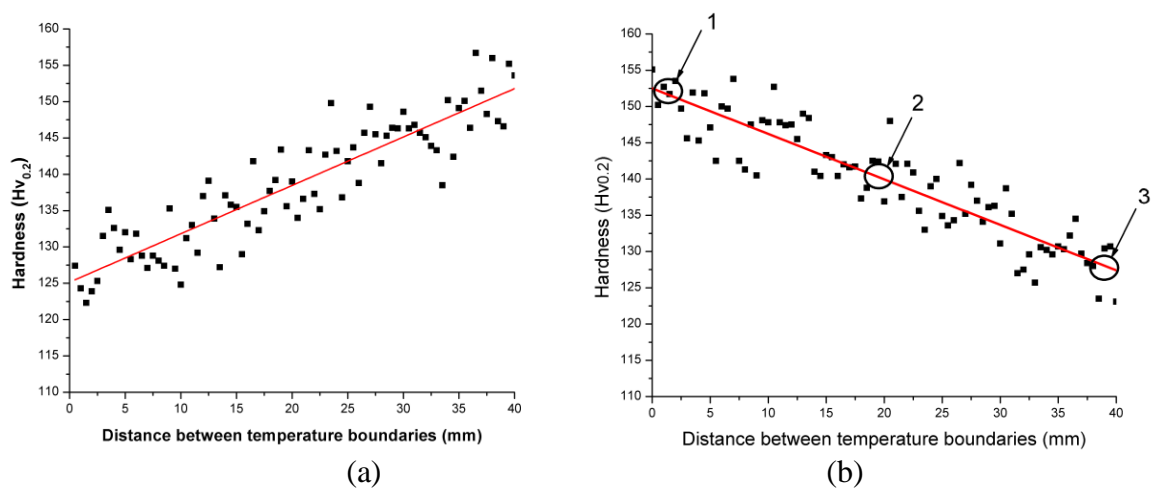
(a)   (b)

(c)   (d)
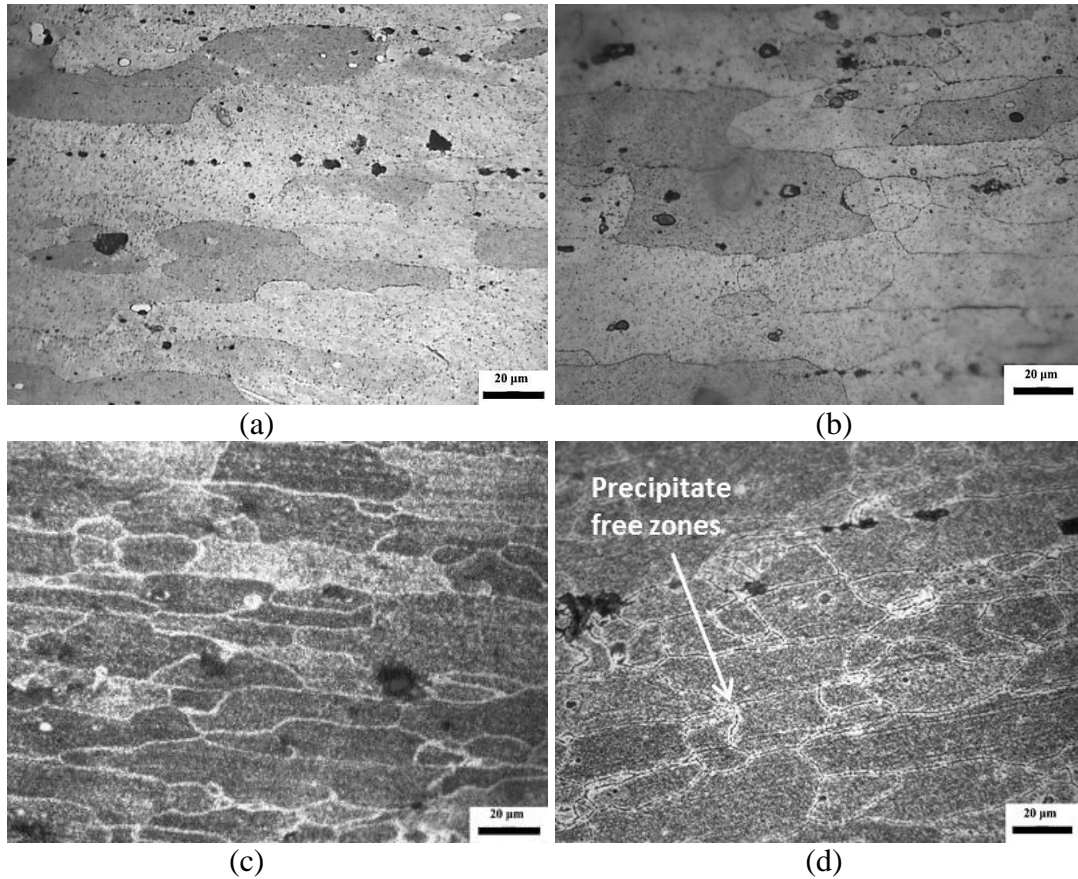
Figure 4.6 Microstructures of (a) HAZ at a distance 12mm from the weld centerline, (b) A200, (c) A250 and (d) A300.

4.1.3 Heat treated material with hardness (strength) gradient

The hardness profiles in the material after heat treatment including exposure to a temperature gradient between 200 and 250°C for 15hours are shown in Figures 4.7a and 4.7b.

(a)   (b)

Figure 4.7 Hardness profiles after heat treatment (a) positive hardness gradient with distance (b) negative hardness gradient with distance.

The microstructural variations at positions 1, 2 and 3 within the gradient are shown in Figure 4.8. With regard to the T3 material, coarsening of the metastable phases can be observed inside the grains and inclusions seem to be unaffected. With increasing temperature, coarsening of metastable phases is more pronounced and lead to higher reduction in hardness. Examination of Figures 4.5 and 4.7b reveal that positions 1 and 3 in the gradient have hardness values similar to the materials A200 and A250. Also, comparison of Figures 4.6b and 4.8a gives similar microstructural characteristics of A200 and position 1 in the gradient. Regarding position 3 (Figure 4.8c), the microstructure differences with A250 concern the absence of PFZs observed in A250 (Figure 4.6c).


(a)

(b)

(c)
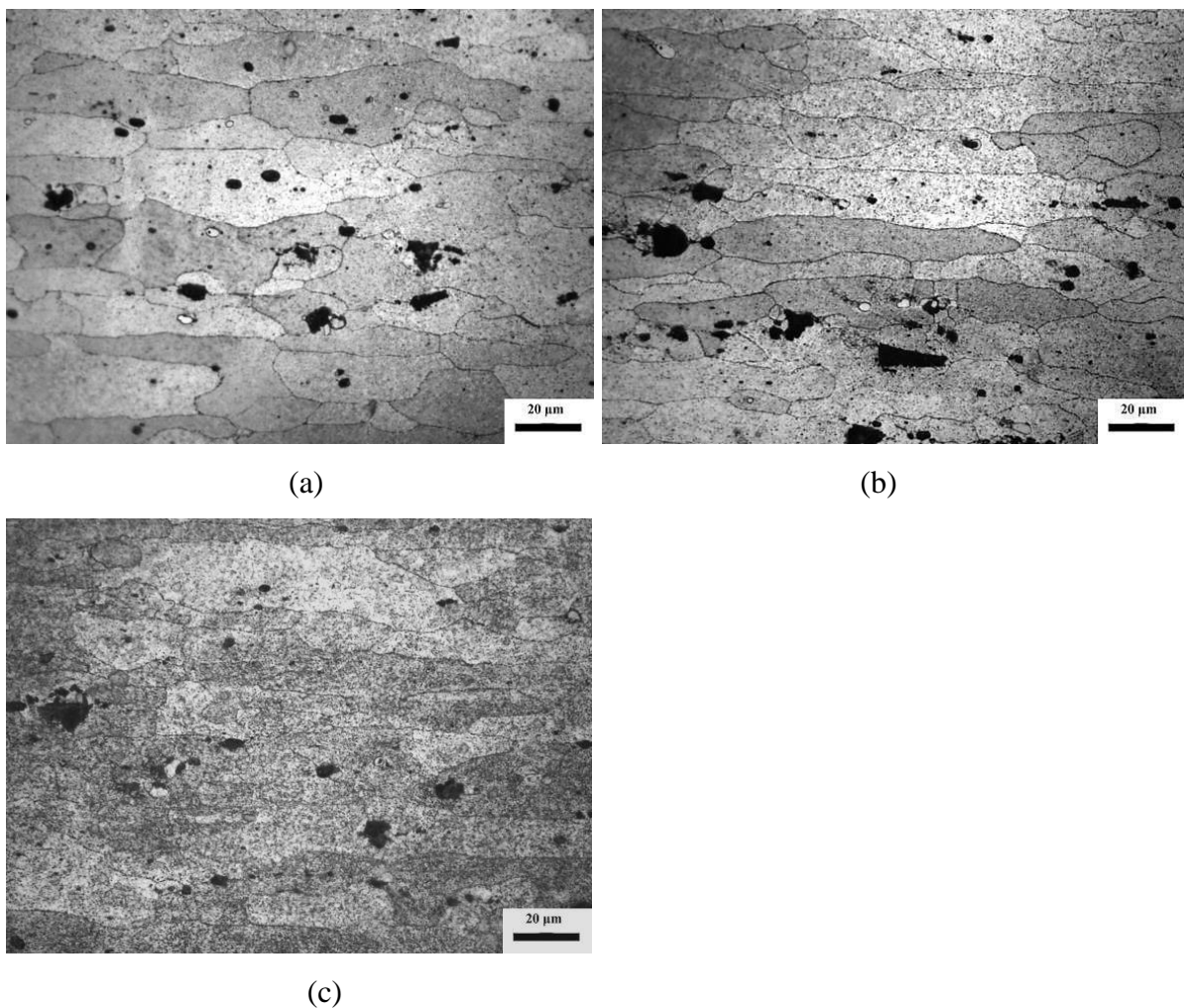
Figure 4.8 Microstructure of materials subjected to artificial aging (a) position 1, (b) position 2, (c) position 3, of Figure 4.7b.

4.2 Weld residual stresses

In Figure 4.9 the distribution of residual stresses measured in the longitudinal direction (y-direction, Figure 2.4a) perpendicular to the weld line is presented. Inside the weld region, in the area which includes the weld nugget and TMAZ, residual stresses are tensile with a magnitude of 52-65MPa. Compressive residual stresses exist in the BM, while the HAZ is characterized by a gradient of tensile residual stresses with boundary values that of the TMAZ and BM. The shift from tensile to compressive stresses appears at a position located ±20mm from the weld center and the distribution is symmetric with respect to the weld centerline. The residual stress profile is consistent with the results in [77] on the same aluminum alloy.

In Figure 4.9 the residual stress profile of the rectangular specimen with dimensions of 75x72mm extracted from the initial welded panel with dimensions of 200x100mm (see Figure 3.9) is presented. After machining, the magnitude of residual stresses in the small specimen is relieved by 33%.
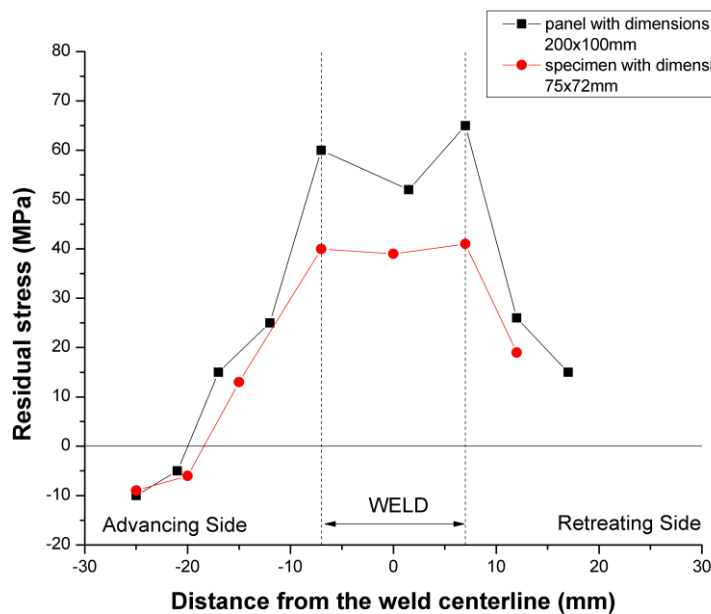
Figure 4.9 Longitudinal residual stress distribution $\sigma_y res(x)$ (see Figure 2.4a) in FSW panel with two different configurations.

4.3 Mechanical performance

4.3.1 Tensile properties

4.3.1.1 Weld material

Tensile properties have been determined in the weld nugget (footprint 3), boundary region of HAZ and TMAZ (footprints 2a, 2r), and HAZ (footprints 1a and 1r) as shown in Figure 4.10. The footprints symbolized as 1a, 1r, 2a, 2r and 3 represent the positions of the specimen

inside the weld for each case resulting in average values of the weld's mechanical properties in the specific area.
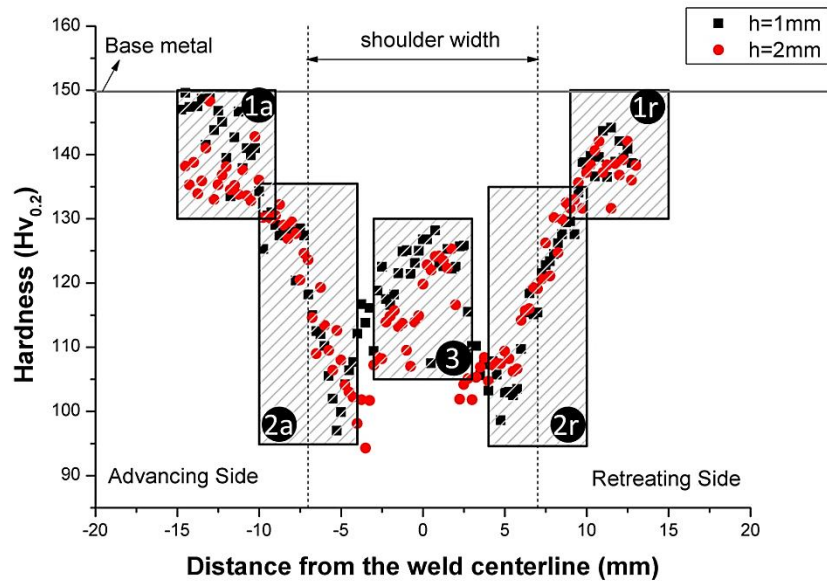

Figure 4.10 Locations where the specimens have been extracted with regard to the microhardness profile and associated weld zones.

The tensile test results are presented in Table 4.1, and the engineering stress-strain curves in Figure 4.11. The yield strength in the HAZ (footprints 1a and 1r, Figure 4.10) is slightly higher compared to the base metal. The yield strength is found 325MPa in the BM and 340MPa in the HAZ (footprint 1a and 1r), while the tensile strength is 477MPa and 482MPa in BM and HAZ respectively. The elongation at fracture is identical in both cases with a value of 18.7%. Footprints 1a, 1r are related to A200 material conditions (see Figure 4.5). The higher yield strength in A200 compared to T3 (BM) is discussed in the next paragraph. In the area with hardness gradient (footprints 2a and 2r, Figure 4.10) a reduction of 10% in yield strength and 16% in tensile strength is observed compared to the base metal. The elongation at fracture is reduced from 18.7% to 10%. In the weld nugget (footprint 3, Figure 4.10), a decrease of 14.5% and 10% in yield and tensile strength respectively is observed compared to the BM. The elongation at fracture is measured at 15.7%.

Table 4.1 Mechanical properties of weld material

Specimen	Yield strength $\sigma_{y0.2}$ (MPa)	Elongation at fracture A_{25} (%)	Tensile strength σ_{UTS} (MPa)	Strain hardening exponent n	Strength coefficient H (MPa)
BM (2024 T3, L-T direction)					
#1	*327*	*18.5*	*480*	*0.131*	*700*
#2	323	19	474	0.133	690
HAZ, Footprint 1a (Figure 4.10)					
#1	344	18	487	0.128	696
#2	339	19	478	0.127	688
HAZ, Footprint 1r (Figure 4.10)					
#1	338	19,4	481	0.126	690
nugget, Footprint 3 (Figure 4.10)					
#1	275	16,5	416	0.174	657
#2	281	14,9	442	0.155	644
HAZ/TMAZ, Footprint 2a (Figure 4.10)					
#1	300	9	412	0.142	604
#2	305	11	411	0.134	591
HAZ/TMAZ, Footprint 2r (Figure 4.10)					
#1	291	9,8	395	0.143	582
#2	274	10,9	384	0.156	588
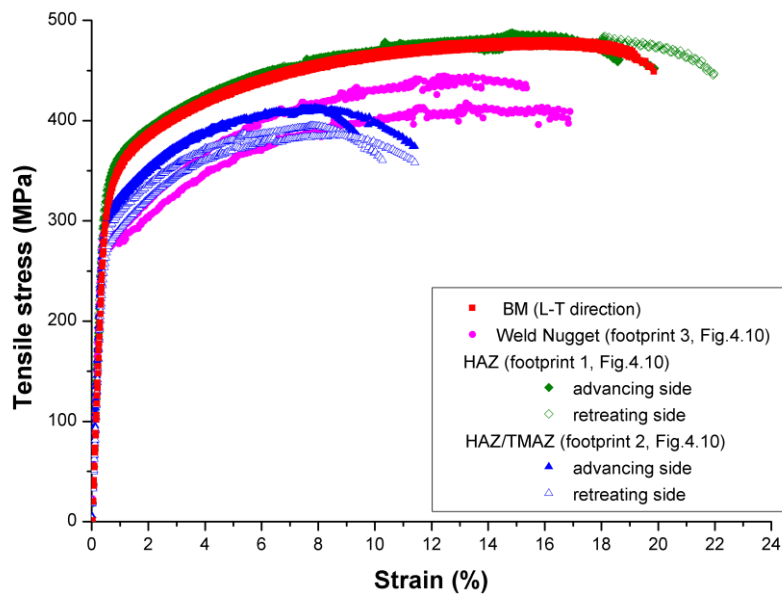
Figure 4.11 Engineering stress-strain curves of different 2024 T3 FSW zones.

The values of strain hardening exponent (Table 4.1) were determined using a Ramberg-Osgood relationship:

$$\sigma = H\varepsilon_p^{\,n} \qquad\qquad (4\text{-}1)$$

48

Equation (4-1) describes the material flow curve with σ and ε_p being the true stress-strain values, which are calculated from:

$$\sigma_{true} = \sigma_{eng}(1+\varepsilon_{eng}) \tag{4-2}$$

$$\varepsilon_{true} = \ln(1+\varepsilon_{eng}) \tag{4-3}$$

where σ_{eng} and ε_{eng} the engineering stress and strain values.

The strain hardening exponent n is higher in the weld material compared to the BM in regions close to the weld nugget. The increase of exponent n is 9% and 25% in the HAZ (footprint 2) and nugget (footprint 3) respectively, compared to the BM. In the boundary region of HAZ and TMAZ (footprint 2), the overaging conditions modify the strain hardening behavior compared to the BM due to the Orowan bypassing mechanism of semi- or incoherent particles [44, 45]. In the weld nugget, the recrystallized microstructure results in a higher decrease of yield strength (reduction of 14.5%) with regard to the tensile strength (reduction of 10%) compared to the BM, which leads to an increase of the strain hardening exponent value. In the HAZ region close to the BM (footprint 1, Figure 4.10), the calculated value of the strain hardening exponent is comparable with the BM.

Comparing the advancing and retreating side (footprints 1a and 1r) the properties are similar. Small differences are observed in regions close to the weld nugget (footprints 2a and 2r) due to the dissimilar deformation behavior of the material caused by the rotation of the welding tool in these sides.

4.3.1.2 Uniformly heat treated materials (A200, A250 and A300)

The tensile properties of the uniformly heat treated materials in L and L-T directions are given in Table 4.2 and the engineering stress-strain curves are shown in Figures 4.12a and 4.12b. In T3 condition, the yield strength of the material is 375MPa (325 MPa in L-T direction) and the tensile strength is 490MPa (477 MPa in L-T direction). The elongation at fracture is 19% in L direction and 15% in L-T direction. In the heat treated alloys, a decrease in yield strength with increasing aging temperature is observed. The reduction is 36% (25% in L-T direction) in A250 and 64% in A300 with respect to the T3 value. In A200 a slight increase of yield strength is observed due to the fact that A200 is closer to the peak-aged condition compared to T3 material (Figure 4.4a). The elongation at fracture for the three overaging conditions is reduced by 30% compared to the T3 state (47% ~ 60% in L-T

49
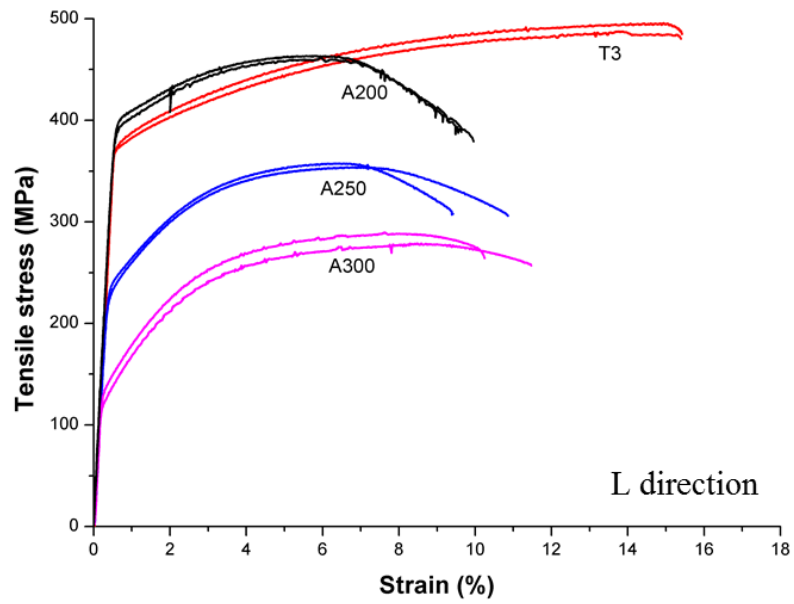
direction).

(a)
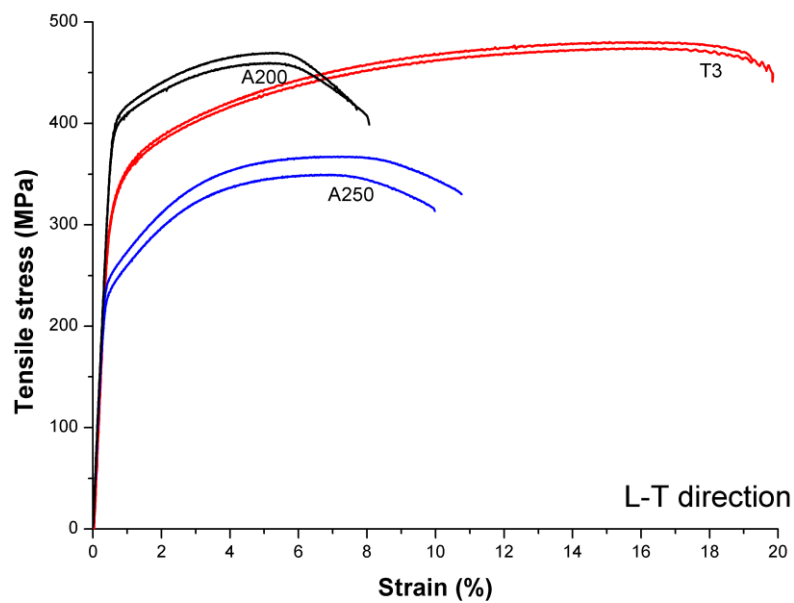
(b)

Figure 4.12 Engineering stress-strain curves of T3 and overaged materials (a) L direction (b) L-T direction.

As discussed previously, the strain hardening behavior is related to the overaging conditions of the aluminum alloy. Here, the strain hardening exponent increases with overaging temperature as shown in Table 4.2.

Table 4.2 Tensile test results of 2024 aluminum alloy in T3 and uniformly heat treated conditions

		Yield strength $\sigma_{y0.2}$ (MPa)	Elongation at fracture A_{25} (%)	Tensile strength σ_{UTS} (MPa)	Strain hardening exponent n	Strength coefficient H (MPa)
L direction	**T3**	*375*	*15*	*490*	*0.120*	*694*
	A200	*395*	*9.5*	*460*	*0.069*	*590*
	A250	*240*	*10*	*355*	*0.161*	*604*
	A300	*135*	*11*	*285*	*0.242*	*594*
L-T direction	**T3**	*325*	*18.7*	*477*	*0.132*	*695*
	A200	*402*	*7.4*	*464*	*0.065*	*592*
	A250	*244*	*9.9*	*358*	*0.152*	*590*

In Figure 4.13 the stress-strain curves of A200 and A250 materials are compared with the behavior of the HAZ material (areas 1 and 2 in Figure 4.10). A good agreement in terms of strength and elongation is obtained, which confirms the reliability of the developed methodology for HAZ simulation. More importantly, the heat treated materials present similar strain hardening behavior with the HAZ material. This characteristic is used to develop the analytical part of the work in paragraph 5.1.
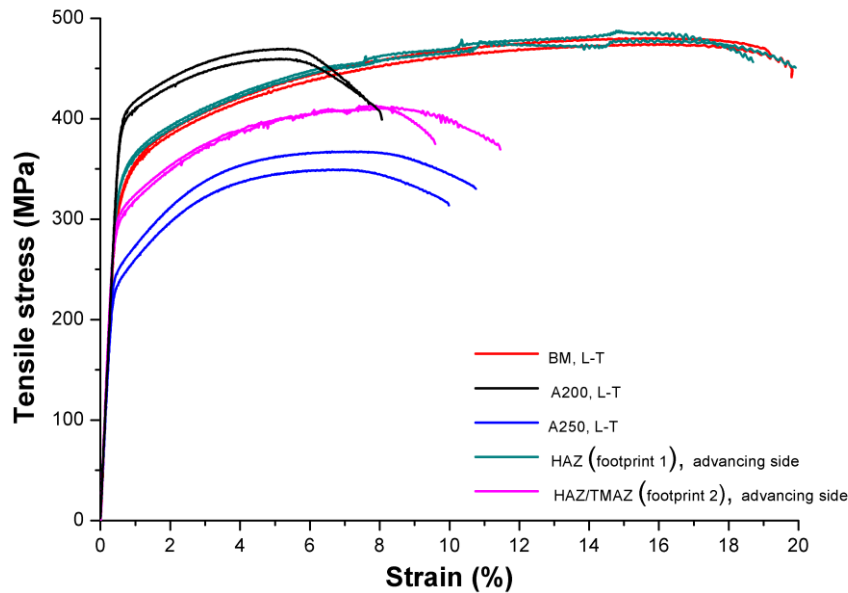
Figure 4.13 Comparison of engineering stress-strain curves in T3, A200, A250 and HAZ materials.

4.3.2 Fracture Toughness

In Figure 4.14 the force vs crack increment diagrams for T3 and A300 materials are displayed. In the T3 material the maximum force (mean value) for stable crack extension was 7730 N, while in A300 the maximum force was 4382 N, a reduction of 43.3% compared to the T3 alloy. The above values result in a stress intensity factor K_{max}= 63.45 MPam$^{1/2}$ in T3 alloy and 22.45 MPam$^{1/2}$ in A300 material. The maximum stress intensity factor is considered as the fracture toughness value of the specific specimen configuration, which complies with LEFM conditions.
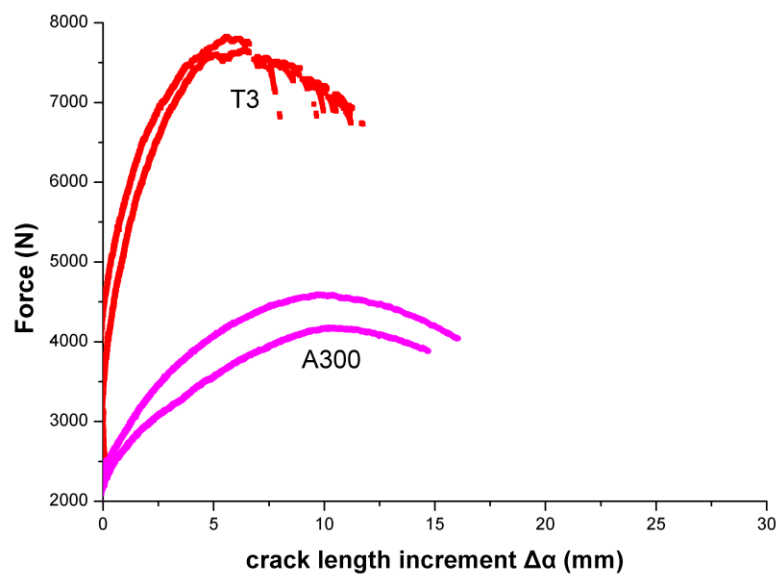
Figure 4.14 Force vs crack length diagrams for T3 and A300 materials.

Table 4.3 Fracture toughness results for T3 and A300 materials

Material		Maximum force P_{max} (N)		Stress intensity factor K_{max} (MPam$^{1/2}$)	
T3	#1	7802	Mean value:	63.42	Mean value:
	#2	7660	7730	63.47	63.45
A300	#1	4175	Mean value:	22.1	Mean value:
	#2	4590	4382	22.8	22.45

52

4.3.3 Fatigue crack growth rates

4.3.3.1 FSW material

The fatigue crack growth rate in the weld material has been examined for the configurations FSW#1, FSW#2 and FSW#3 presented in paragraph 3.7.2 (Figure 3.14).
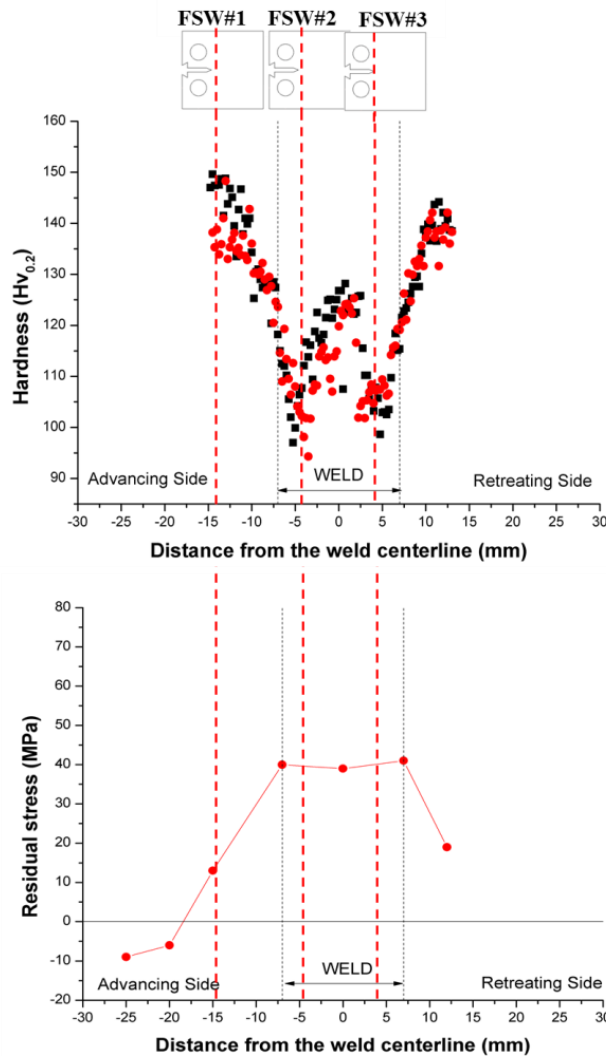
Figure 4.15 Configurations FSW#1, FSW#2 and FSW#3 used to examine FCG behavior in the weld region.

The results are presented in Figure 4.16. In FSW#1, rates are lower compared to FSW#2 and FSW#3 in the same ΔK range. The lower FCG rates of FSW#1 are in agreement with [77, 90, 101]. Regions dominated by compressive or low tensile residual stress fields retard fatigue crack propagation in opposition to regions with fully tensile residual stress fields, which accelerate crack growth. In FSW#2 and FSW#3, at lower ΔK values (11~12 MPam$^{1/2}$) crack growth rates are in the same range, while at higher ΔK FSW#3 exhibits higher crack growth

rates. In both cases, the tensile residual stress field in the wake and in front of the crack plays a dominant role on FCG.

The Paris equation constants, shown in Table 4.4, confirm the crack growth behavior analyzed above. Specimens FSW#2 and FSW#3 have similar D values, while parameter m is slightly higher in FSW#3. FSW#1 has the lowest D and the highest m value from the three cases examined.
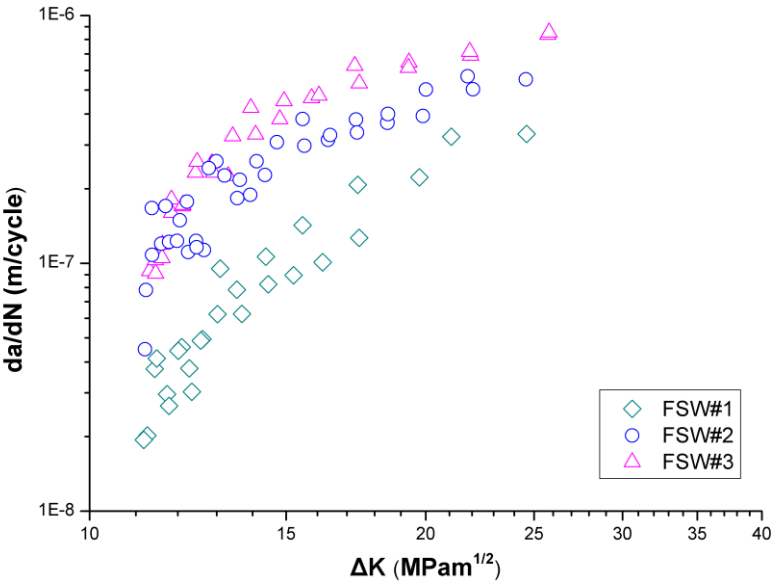
Figure 4.16 Fatigue crack growth rates versus stress intensity factor range for configurations FSW#1, FSW#2 and FSW#3.

Table 4.4 Paris constants calculated for configurations FSW#1, FSW#2 and FSW#3

	Specimen	Parameter m	Parameter D
FSW#1	#1	3.30	1.04×10^{-11}
	#2	4.24	1.04×10^{-12}
FSW#2	#1	2.37	3.68×10^{-10}
	#2	2.41	3.83×10^{-10}
FSW#3	#1	2.37	3.96×10^{-10}
	#2	2.58	2.86×10^{-10}

The crack closure measurements displayed in Figure 4.17 also corroborate the FCG rates observed. The higher levels of crack closure were found in FSW#1, which in the range ΔK=11-15 MPam$^{1/2}$ presents P_{op}/P_{max} values between 0.54 and 0.57. In FSW#2 and FSW#3, P_{op}/P_{max} values where comparable in the same ΔK range (0.31-0.38), with a shift occurring in

the ΔK range 13-15MPam$^{1/2}$. In this range, FSW#2 shows an increase in closure (0.42-0.48) with the respective FSW#3 values being 0.36-0.37. The above crack closure values are consistent with the FCG rates observed in Figure 4.16. For ΔK values higher than 15 MPam$^{1/2}$, a gradual drop of the crack closure is observed in all cases examined. At high ΔK values, the variation of the microstructure and residual stresses profile cannot influence significantly crack closure levels [24, 28, 121, 122].

The results showed that FCG rates in the weld region are strongly dependent on the position of the crack with regard to the weld center. Variation in microstructure and residual stress distribution in the crack plane result in different crack closure levels and FCG rates. The independent contribution of microstructure and residual stresses on FCG is analyzed in the next Sections.
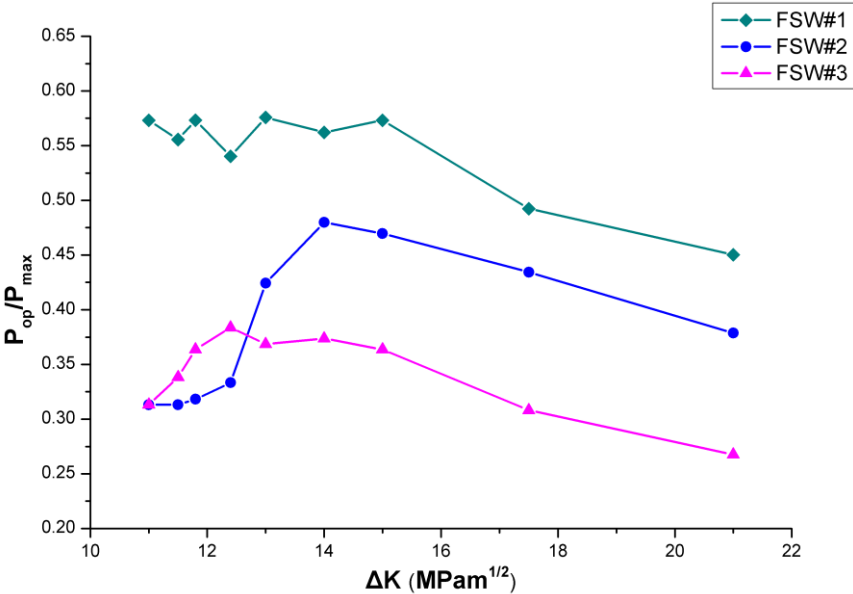
Figure 4.17 Variation of crack closure vs applied stress intensity factor range for configurations FSW#1, FSW#2 and FSW#3.

4.3.3.2 Uniformly heat treated materials (A200, A250 and A300)

The fatigue crack growth results for the T3 and uniformly heat treated materials are compared in Figures 4.18a and 4.19. For better clarity, in the Figures only 2 characteristic tests are presented for each material condition. Fatigue crack growth resistance is enhanced after overaging treatment and increases with the magnitude of overaging temperature. In Figure 4.18b the mean experimental fatigue lives for each condition are shown, taking into account the standard deviation. The outcome of Figure 4.19 is that crack growth rates in A250 and A300 materials are lower than in T3 material, in the whole ΔK range examined, with the

A300 exhibiting superior crack growth resistance. The effect is more noticeable in the lower ΔK range between 12-15 MPam$^{1/2}$. In the case of A200, FCG rates are comparable to the rates of T3 material.

The Paris equation constants were determined from the experimental results and are presented in Table 4.5. The value of parameter D decreases with increasing aging temperature, which agrees with the lower crack growth rates in the overaged material described previously.
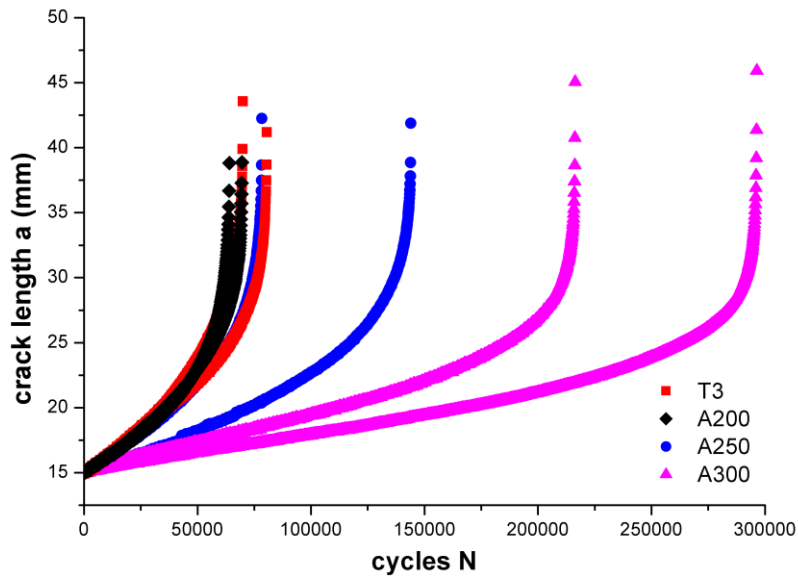
(a)
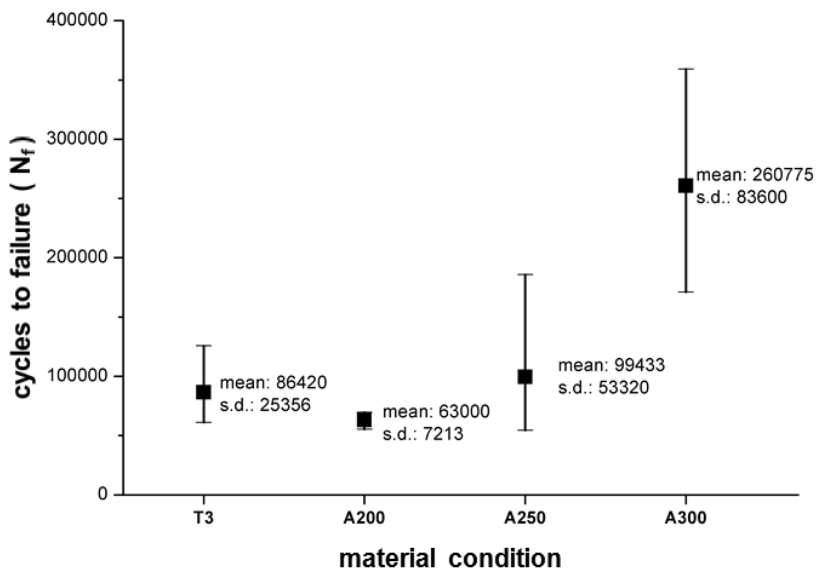
(b)

Figure 4.18 (a) Constant stress amplitude crack growth curves in T3, A200, A250 and A300 materials (b) Fatigue lives obtained from (a-N) curves given as mean values with standard deviation (s.d.).
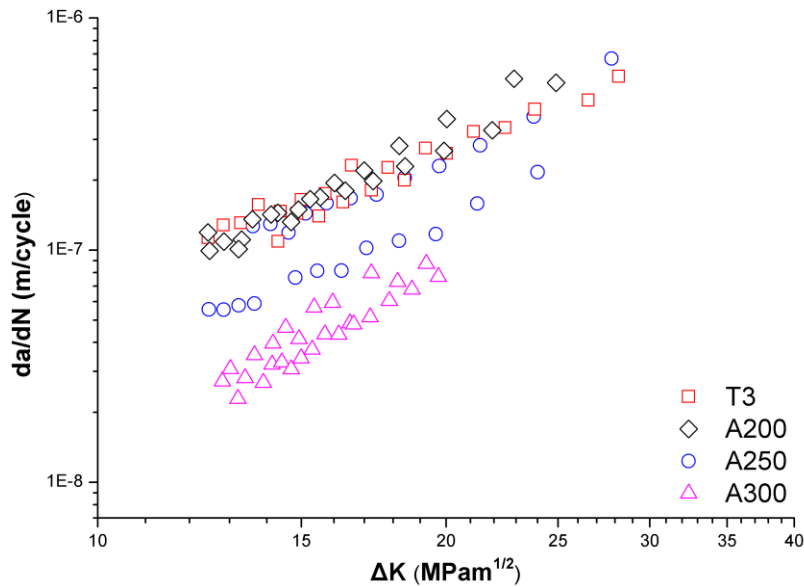
Figure 4.19 Fatigue crack growth rates vs. stress intensity factor range (dα/dN-ΔK) in T3, A200, A250 and A300 materials.

Table 4.5 Values of Paris constants D and m

Specimen number		Parameter m		Parameter D	
T3	#1	1.78		1.9×10^{-9}	
	#2	2.15		2.24×10^{-10}	
	#3	2.19	**mean value:** 2.01	3.5×10^{-10}	**mean value**: 7.51×10^{-10}
	#4	1.80		8.55×10^{-10}	
	#5	1.93		8.88×10^{-10}	
	#6	2.21		2.93×10^{-10}	
A200	#1	2.23	**mean value:** 2.33	3.53×10^{-10}	**mean value:** 6.65×10^{-10}
	#2	2.94		5.33×10^{-11}	
	#3	1.84		1.58×10^{-9}	
A250	#1	1.89		1.44×10^{-9}	
	#2	2.64		5.59×10^{-11}	
	#3	2.01	**mean value:** 2.17	9.83×10^{-10}	**mean value:** 5.93×10^{-10}
	#4	2.26		3.63×10^{-10}	
	#5	2.34		2.29×10^{-10}	
	#6	1.88		4.88×10^{-10}	
A300	#1	2.91		1.18×10^{-11}	
	#2	2.51		5.24×10^{-11}	
	#3	2.85	**mean value:** 2.72	1.57×10^{-11}	**mean value:** 2.96×10^{-11}
	#4	2.51		5.24×10^{-11}	
	#5	2.85		1.57×10^{-11}	

The measurements of crack closure during FCG are presented in Figure 4.20a. The magnitude of crack closure increases steeply with increasing overaging temperature in the

range 11-15 MPam$^{1/2}$, which agrees with the lower D values shown in Table 4.5 (taking into account that variation of parameter m between the materials is small).

In Figure 4.20b the FCG rates are compared for all materials using the effective stress intensity factor range ΔK_{eff}. ΔK_{eff} was calculated according to [114], where K_{op} is the stress intensity factor for the measured P_{op} (crack opening load).

$$\Delta K_{eff} = K_{max} - K_{op} \qquad\qquad (4\text{-}4)$$

For the calculation of K_{op}, a mean value of P_{op} was used for each material in the range 11-21 MPam$^{1/2}$. The mean values of P_{op} were 0.65, 0.65, 0.85 and 1 kN for T3, A200, A250 and A300 materials respectively. With consideration of ΔK_{eff} values, crack growth rate levels are converging in a narrow band, which demonstrates the influence of crack closure on FCG rates.

The results are in agreement with the fact that crack closure is generally more dominant at lower ΔK levels [24, 28, 121, 122] and that crack closure levels increase with the magnitude of aging temperature, which rationalizes the FCG performance observed in Figure 4.19.
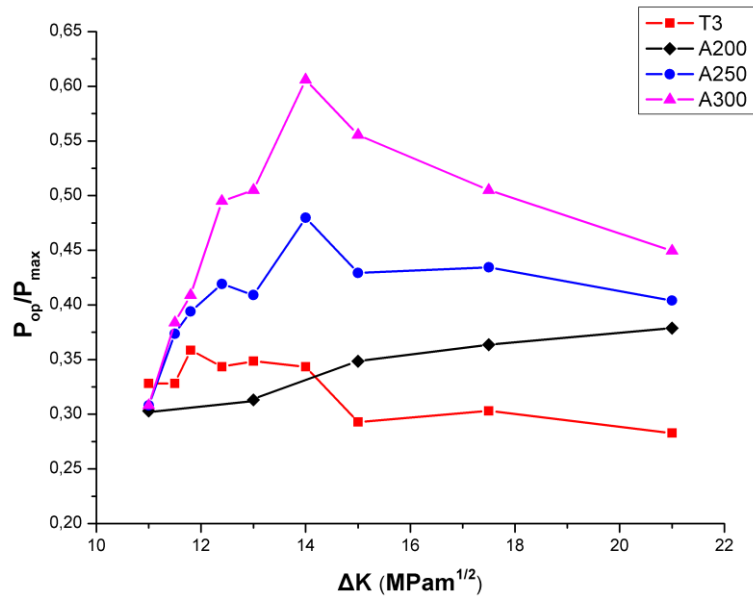
(a)
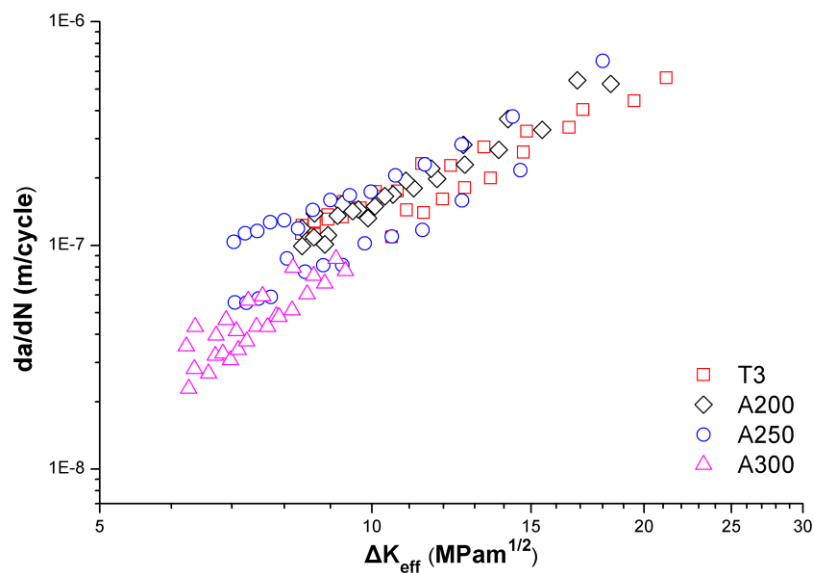
(b)

Figure 4.20 (a) Crack closure vs applied stress intensity factor range in T3 and overaged materials (b) Fatigue crack growth rates vs. effective stress intensity factor range in T3 and overaged materials.

In the micrographs of Figure 4.21 segments of fracture surfaces of T3 and A300 materials are presented. The fracture characteristics of A300 material (Figure 4.21b) are more brittle compared to T3 (Figure 4.21a), and are characterized by radiating ridges from the notch tip, sign of the crack changing slip planes during crack growth [123]. Thus, the fracture path in A300 includes more surface irregularities than T3, which are expected however to have small

contribution to the measured crack closure levels in the intermediate ΔK region. This effect has been shown to be significant in microstructures with variations in grain morphology characteristics resulting in significant crack path tortuosity [38, 40], which is not the case in the present study.
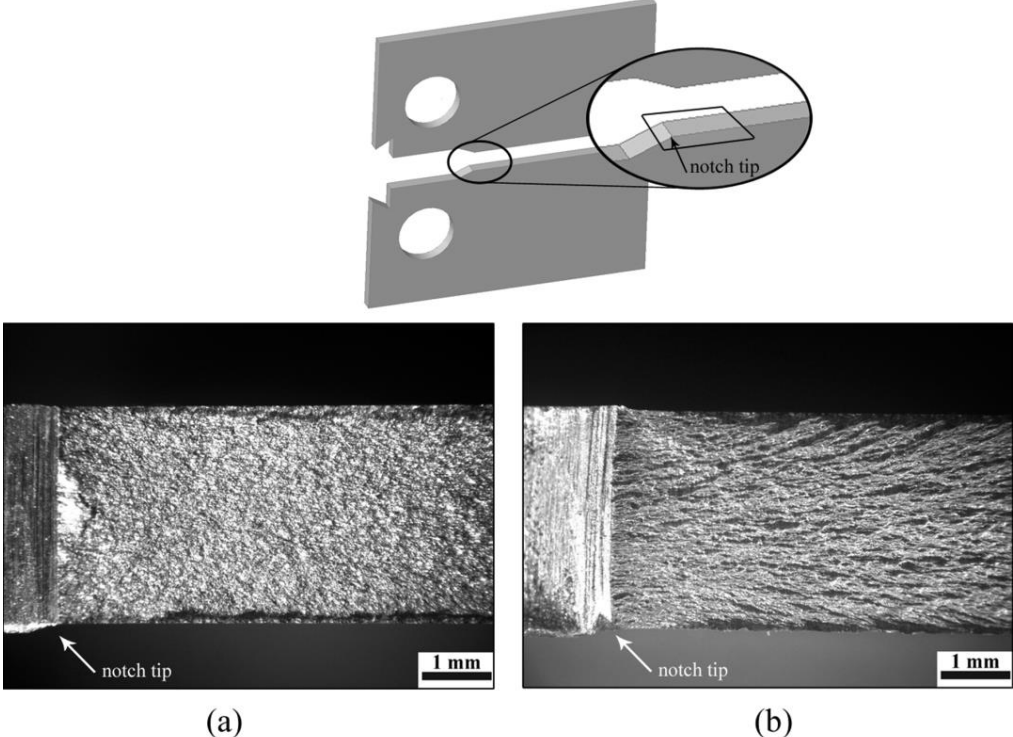
Figure 4.21 Images taken with optical stereoscopy showing segments of fracture surface characteristics during FCG of (a) T3 material (b) A300 material.

In the micrographs of Figure 4.22 the fracture surfaces of T3 and A300 materials taken at a crack length of 16mm (ΔK value of 12 MPam$^{1/2}$) are displayed. The micrographs show a semi-cleavage fracture pattern in T3 alloy consisting of dimples as well as cleavage facets (Figure 4.22a). Fracture surfaces of A300 material include larger brittle regions compared to T3 (Figure 4.22b). This may explain the lower fracture toughness values obtained in A300 compared to T3 alloy (paragraph 4.3.2). The more brittle behavior in combination with the lower crack growth rates in the overaged alloy found previously, suggest that the important factor contributing to crack closure is cyclic strain hardening at the crack tip rather than accumulation of cyclic plasticity. Cyclic strain hardening reduces the ability of the material to plastically deform at the crack front. According to the work in [42], this has been associated with extension of the plastic deformation to the back of the crack tip enhancing crack closure. The influence of overaging on cyclic strain hardening is studied in paragraph 4.3.4.

<div align="center">

(a)   (b)
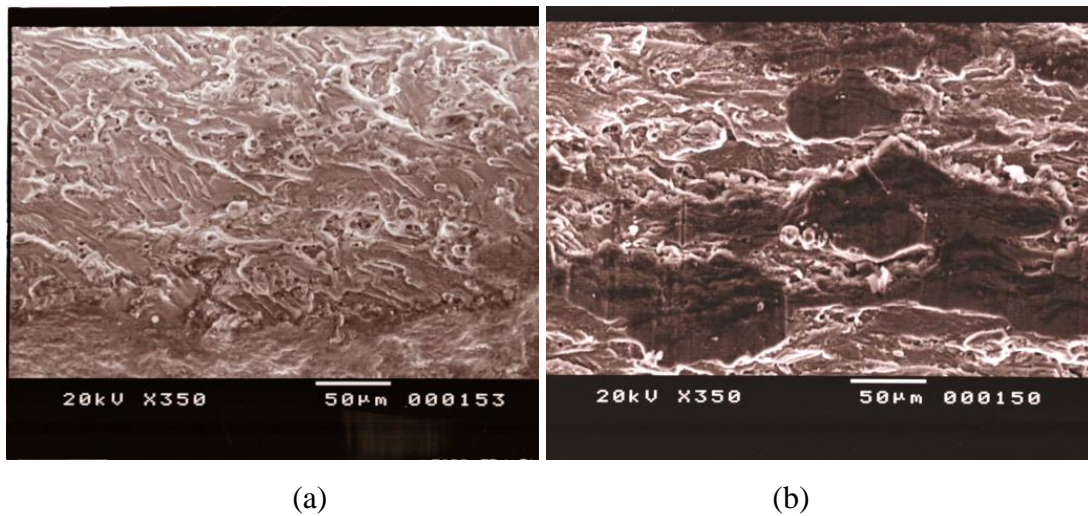
Figure 4.22 SEM micrographs showing fracture surface characteristics during FCG in (a) T3 condition (b) A300 material.

</div>

4.3.3.3 Material with hardness (strength) gradient

The FCG results of specimens including a positive or negative strength gradient are displayed in Figures 4.23a and 4.23b. They are compared with material conditions at the time that the crack enters the gradient (e.g. notch tip). The material conditions at the notch tip for a specimen with a positive strength gradient are that of A250 material, and for a specimen with negative strength gradient are that of A200 material (Figures 3.15a and 3.15b).

In the positive strength gradient (Figure 4.23a), crack growth rates are higher with regard to the reference condition. In the negative strength gradient, FCG rate is not significantly influenced by the presence of the gradient, as shown in Figure 4.23b.
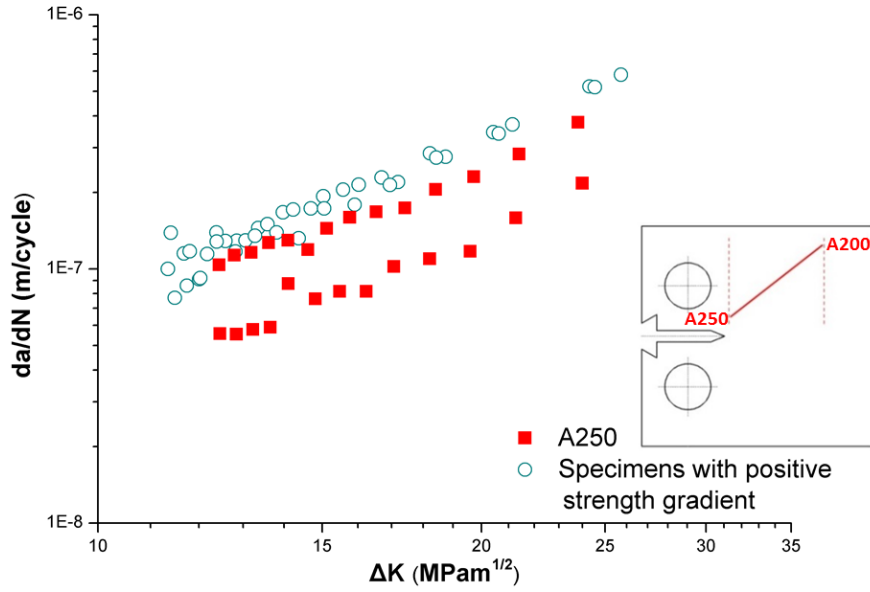
(a)
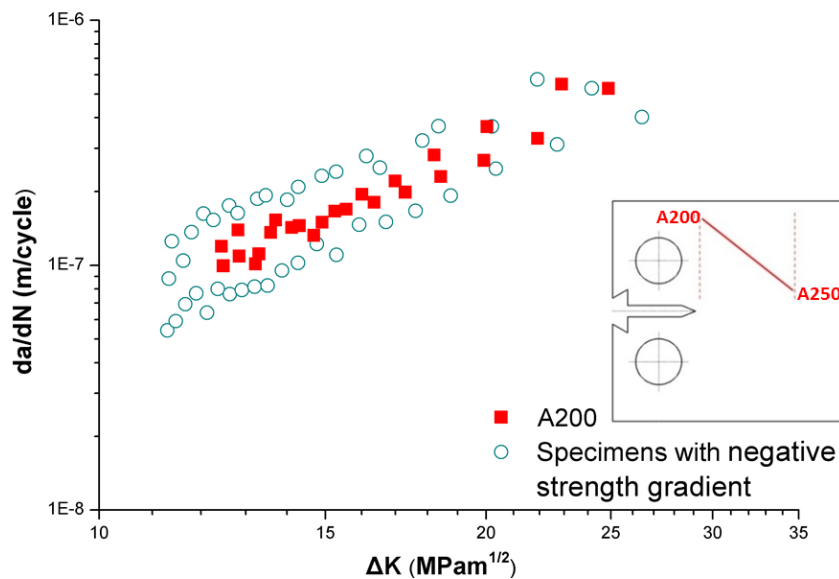
(b)

Figure 4.23 Fatigue crack growth rates vs stress intensity factor range (dα/dN-ΔK) in (a) A250 and material with positive strength gradient (b) A200 and material with negative strength gradient.

In Figures 4.24 and 4.25 fracture surfaces at crack lengths 15mm (area A) and 25mm (area B), corresponding to ΔK values of 11 and 20 MPam$^{1/2}$ respectively, are displayed. In both gradients a semi-cleavage fracture pattern is observed with the cleavage characteristics more pronounced in area A. By comparing areas A and B for the two gradients, the characteristics are similar consisting of dimples as well as cleavage facets.
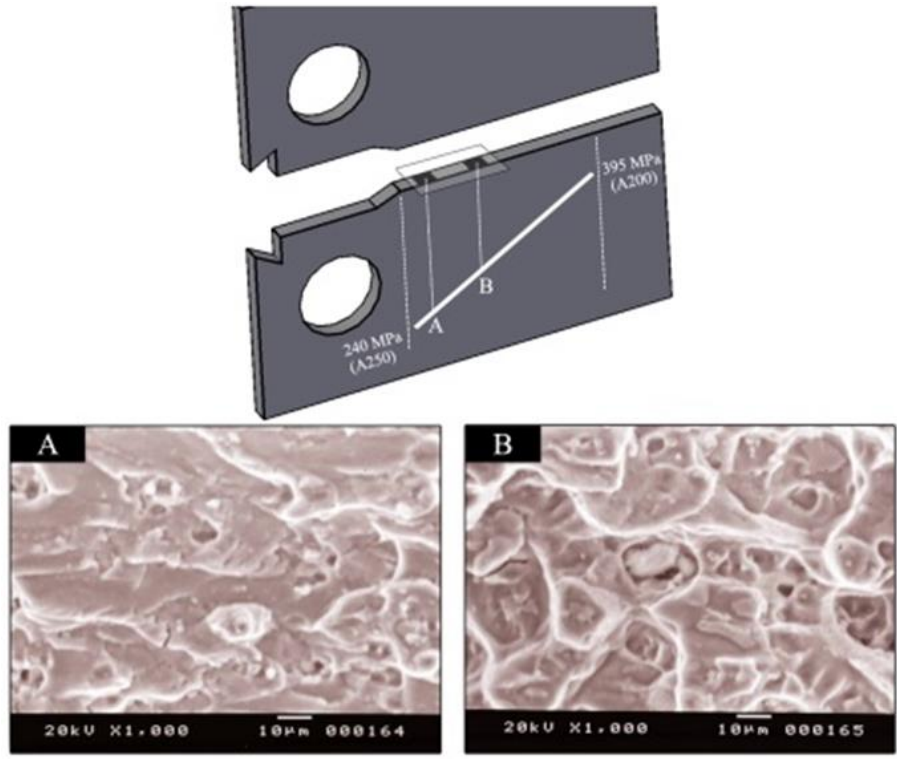
Figure 4.24 Fracture surface characteristics of specimen with positive strength gradient at ΔK values a) ΔK=11 MPam$^{1/2}$ b) ΔK=20 MPam$^{1/2}$.
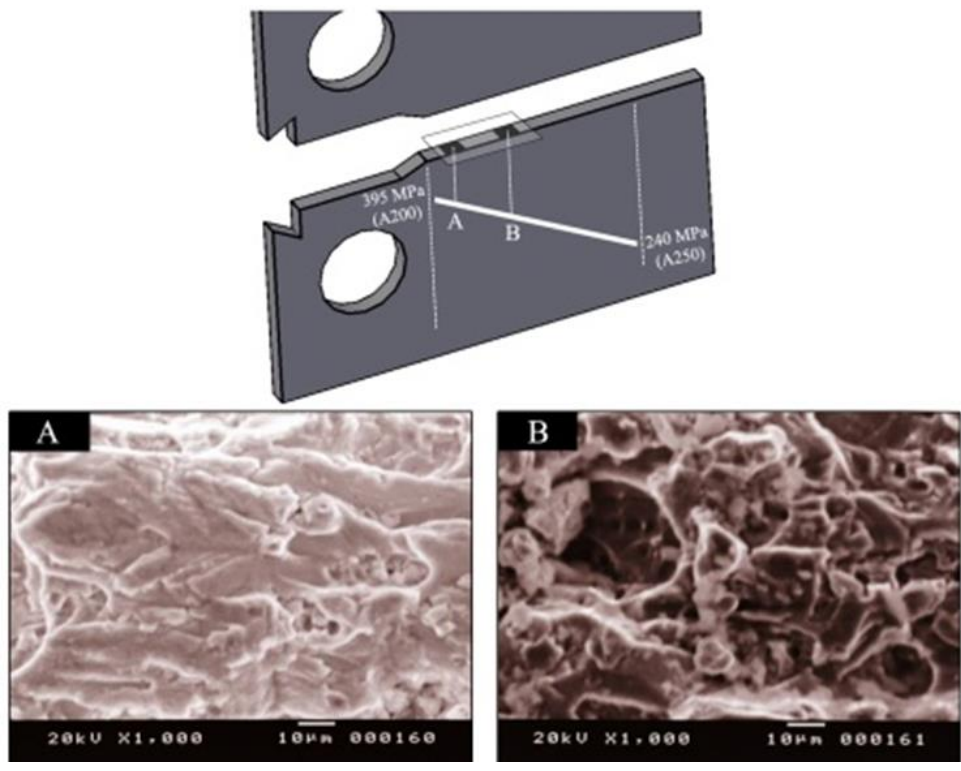
Figure 4.25 Fracture surface characteristics of specimen with negative strength gradient at ΔK values a) ΔK=11 MPam$^{1/2}$ b) ΔK=20 MPam$^{1/2}$.

The results show that strength gradients may influence fatigue crack growth rate in 2024 T3 aluminum alloy. The effect is more noticeable when a crack encounters a gradient with an increasing slope. In [46] the role of gradients has been explained with the interactions of plastic zone size and their effect on crack growth rate. The complex mechanisms influencing crack growth rate in the cases examined, require further investigation to assess which influence is more pronounced on fatigue crack growth, which exceed the scope of the present study.

4.3.4 Strain controlled cyclic tests

In this paragraph, the cyclic strain hardening behavior of A250 and A300 materials is studied and compared to the material in T3 state. In Figure 4.26 the experimental strain-life curves are shown. Fatigue lives for a plastic strain range between 0.08% and 0.1% are higher in the overaged materials compared to T3. The A250 and A300 materials showed similar LCF behavior.

The Coffin-Manson parameters have been determined based on equation:

$$\varepsilon_{p,a} = \varepsilon_f' \left(2N_f\right)^c \tag{4-5}$$

where ε_f' is the fatigue ductility coefficient and c is the fatigue ductility exponent [61, 62]. The experimental constants of equation (4-5) are given in Figure 4.26.
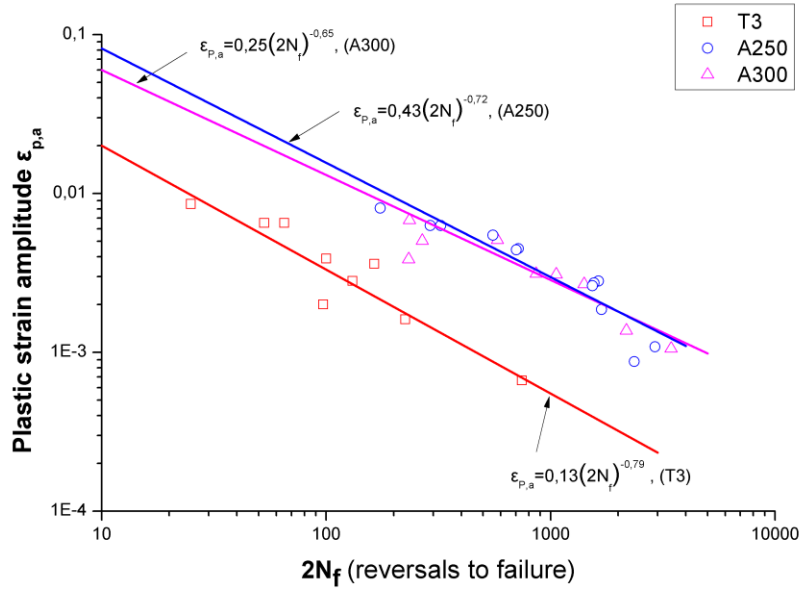
Figure 4.26 Strain-life curves of T3, A250 and A300 materials.

To examine the cyclic hardening behavior, the evolution of peak stress during cyclic loading with the number of cycles are compared for a plastic strain range 0.2% and 0.45% in Figures 4.27a and 4.27b. Tension and compression stress peaks increase with the number of cycles, with the compression curve lying on, or slightly above the respective tension curve, indicating absence of Bauschinger effect. During the initial phase, cyclic hardening occurs, leading to an increase in tensile peak stresses σ_p, followed by an extended phase of maximum cyclic stress saturation N_{sat} (during which stresses present a variation of less than 2.5%). The fatigue lives obtained for both strain levels are higher for A300 material, an indication of higher low cycle fatigue resistance compared to the T3 material. The cyclic hardening magnitude (percentage increase in stress amplitude) has been determined for the $N_{hardening}$ phase, which precedes the N_{sat} phase, as shown in Figure 4.27. For 0.2% plastic strain range the increase in stress amplitude is 11% in the T3 material, at the stabilized cyclic stress-strain behavior, whereas in the overaged material the increase is 25%. At 0.45% plastic strain range the respective $\Delta\sigma$ increase is 17% for T3 material and 26% for the overaged material. At 0.2% plastic strain range, the fatigue crack initiation phase (N_{ini}) is noticeable at the end of N_{sat} phase, where a drop in maximum stresses is observed. At 0.45% plastic strain range, the respective crack initiation period was very small, and sudden fracture occurred at the end of N_{sat} phase.

Based on the test results it can be concluded that the A300 material presents higher cyclic hardening potential than the 2024 alloy in T3 condition.
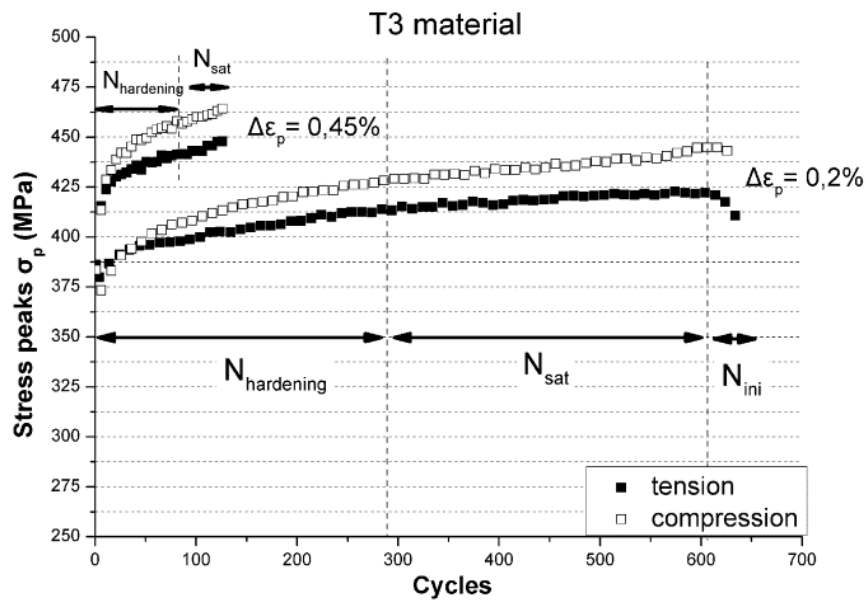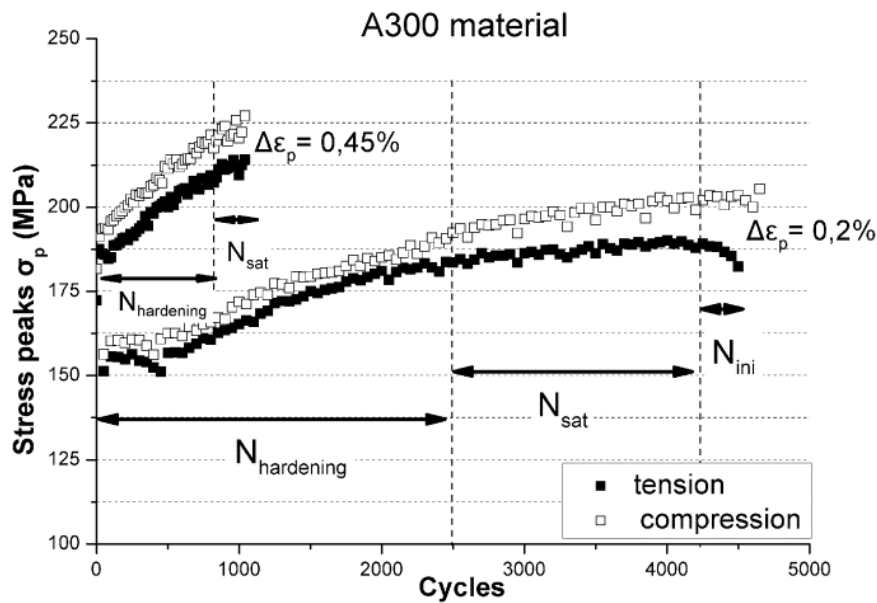
Figure 4.27 Evolution of peak stress with number of cycles for plastic strain range of 0.2% and 0.45% in (a) T3 and (b) A300 material.

The cyclic stress-strain curves are plotted up to a strain range of 2% (Figure 4.28). T3 and A300 materials exhibit cyclic strain hardening with the cyclic curve positioned above the respective monotonic behavior. An increase in cyclic yield strength ($\sigma_{c0.2}$) due to cyclic hardening, of 37% and 16% in A300 and T3 materials respectively, compared to the monotonic behavior is obtained. The cyclic strain hardening exponent n´ and cyclic strength

coefficient H´ were assessed with the Ramberg-Osgood equation [25]:

$$\frac{\Delta\varepsilon}{2} = \frac{\Delta\sigma}{2E} + \left(\frac{\Delta\sigma}{2H^{'}}\right)^{1/n'}$$ (4-6)

 The constants n´, H´ of equation (4-6) are given in Table 4.6 and are compared with the respective n and H values for the monotonic behavior. Cyclic strain hardening exponents after overaging are significantly increased compared to the initial T3 condition. Interesting is the cyclic stress-strain response in A250, which initially reveals smaller cyclic strain hardening compared to T3 and A300 alloys, that increases gradually for higher strain values, a behavior which requires further investigation.
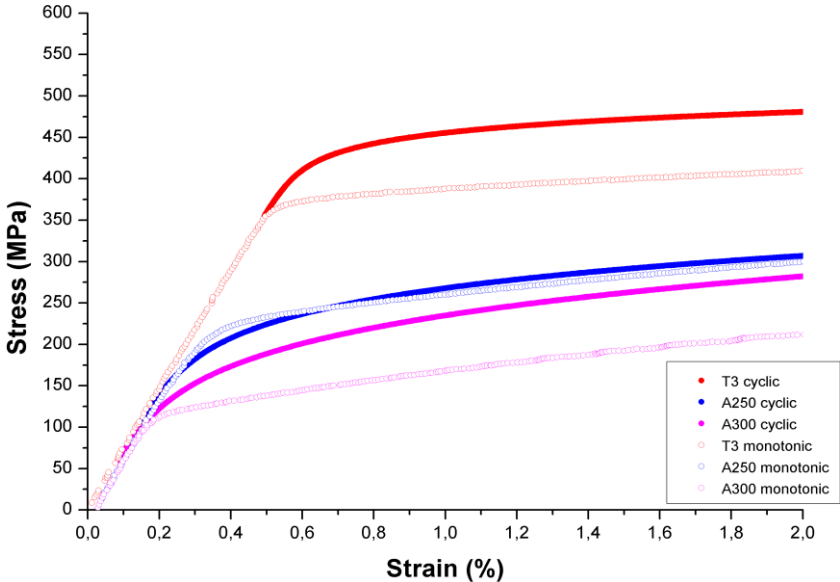
Figure 4.28 Monotonic & cyclic stress- strain curves of T3, A250 and A300 materials.

Table 4.6 Cyclic and monotonic properties of T3, A250 and A300 materials

	Yield strength $\sigma_{0.2}$ (MPa)	Cyclic yield strength $\sigma_{c0.2}$ (MPa)	Strain hardening exponent n	Strength coefficient H (MPa)	Cyclic strain hardening exponent n´	Cyclic strength coefficient H´ (MPa)
T3	375	445	0.120	694	0.042	576
A250	245	245	0.161	604	0.148	568
A300	135	185	0.242	594	0.211	674

Chapter 5: Fatigue crack growth analysis in weld material under mode I loading

In this Chapter, an analytical model is developed, which uses the experimental findings of Chapter 4 to predict fatigue crack growth rate under mode I loading in the weld region. The model takes into account both factors influencing fatigue crack growth discussed previously, which are the variation in microstructure and the residual stresses. In the implementation of the model, the two effects are analyzed separately.

5.1 Modelling the effect of microstructure (HAZ) on fatigue crack growth

Modelling the influence of microstructural effects on fatigue crack growth is very complex and requires a thorough understanding of how damage accumulates and propagates in a multiscale nature. Even more so, in case of weld material where variation of microstructure appears. Modelling tools to predict fatigue crack growth rely mostly on macro-mechanical parameters, which are influenced by the underlying microstructure [55-57, 63, 64]. A similar approach is proposed here, to include in the macro-scale analysis an appropriate parameter, related to the microstructural changes in the weld region, which is representative of the material condition in micro-scale. Based on the studies in [41-43], cyclic strain hardening at the crack tip is related to the closure levels of the advancing crack and hence fatigue crack growth rate. The cyclic strain hardening behavior is influenced by the overaging condition of the material (see paragraph 4.3.4). This dependency has been exploited in the analysis, to account for microstructural variations through the varying cyclic strain hardening properties in the weld material and specifically in the HAZ.

5.1.1 Critical Energy dissipation for crack growth

A material degrades under fatigue by damage accumulation after each cycle of loading initially in the form of cyclic plasticity and then under crack propagation [124]. In many analytical approaches crack growth is assumed to occur incrementally after a critical number of fatigue cycles [55-57, 64]. In the proposed model the crack growth increment is considered equal to a material element with width Δr at the crack plane (Figure 5.1). On this basis, a crack increment of size Δr occurs after a critical number of cycles ΔN. Based on these assumptions, a crack propagation rate can be calculated from equation:

$$\frac{da}{dN} = \frac{\Delta r}{\Delta N} \qquad (5\text{-}1)$$

It is assumed that the material element at the crack tip of width Δr, is subjected to low cycle fatigue conditions [54-57, 63] with an average constant plastic strain range $\Delta \varepsilon_{pm}$.
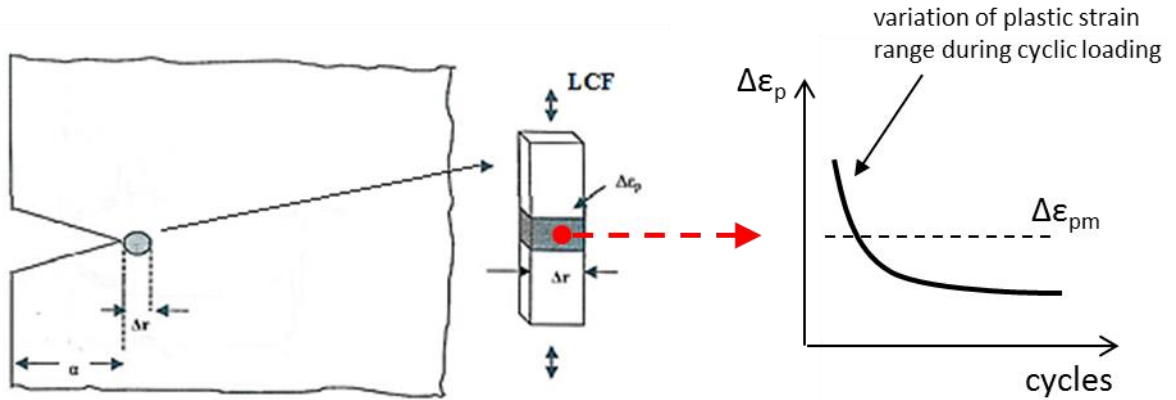
Figure 5.1 Material element ahead of the crack tip subjected to low cycle fatigue conditions.

When a specimen is subjected to cyclic plastic straining, the strain amplitude $\Delta \varepsilon$ can be expressed in terms of the applied stress range $\Delta \sigma$ with the Ramberg-Osgood equation in the form:

$$\frac{\Delta \varepsilon}{2} = \frac{\Delta \sigma}{2E} + \left(\frac{\Delta \sigma}{2H'}\right)^{1/n'} \qquad (5\text{-}2)$$

In equation (5-2), H' is the cyclic strength coefficient and n' is the cyclic strain hardening exponent. In Figure 5.2 a stabilized hysteresis loop is shown under a constant plastic strain range $\Delta \varepsilon_p$ for a strain hardening material. The dissipated plastic strain energy per cycle, is the area of the hysteresis loop and for a Masing material behavior can be described by [60]:

$$\Delta W = 2\sigma_A \Delta \varepsilon_p \left(\frac{1-n'}{1+n'}\right) \qquad (5\text{-}3)$$
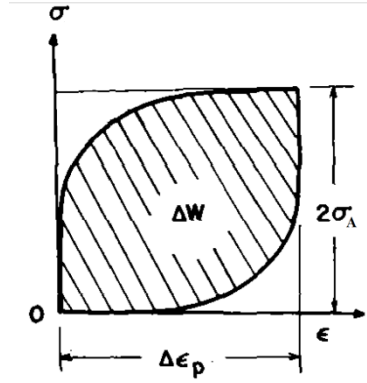
Figure 5.2 Hysteresis loop for a Masing material.

Failure occurs when a critical amount of energy W_f is accumulated in the material after a finite number of loading cycles ΔN. By assuming that the energy per cycle is nearly constant throughout the fatigue test, the total plastic strain energy until fracture may be approximated by [60]:

$$W_f = \Delta W \cdot N_f = 2\sigma_A \cdot \Delta\varepsilon_p \left(\frac{1-n'}{1+n'}\right) N_f \tag{5-4}$$

If the critical amount of energy W_f for the material volume of Figure 5.1 is known, the critical number of cycles necessary for incremental crack growth can be calculated form equation (5-4). To estimate the value W_f the strain energy density theory is implemented.

5.1.2 Strain energy density criterion

In the strain energy density theory (SED) developed by Sih [125, 126], the fundamental quantity is the strain energy density dW/dV contained in a unit volume of material at a given instant of time. The strain energy density function dW/dV with the distance r from the crack tip, has the form:

$$\frac{dW}{dV} = \frac{S}{r} \tag{5-5}$$

where S is the strain energy density factor and r the radial distance measured from the site of possible failure initiation.

The three basic hypotheses of the strain energy density criterion are:

 i) The location of fracture coincides with the location of the relative minimum strain

energy density, $(dW/dV)_{min}$, and yielding with relative maximum strain energy density, $(dW/dV)_{max}$.

ii) Failure by fracture or yielding occurs when, $(dW/dV)_{min}$ or $(dW/dV)_{max}$ reach their respective critical values.

iii) The crack growth increments $r_1, r_2, \ldots r_j, \ldots, r_c$ during stable crack growth satisfy the equation:

$$\left(\frac{dW}{dV}\right)_c = \frac{S_1}{r_1} = \frac{S_2}{r_2} = \cdots = \frac{S_j}{r_j} = \cdots = \frac{S_c}{r_c} \tag{5-6}$$

There is unstable fracture or yielding, when the critical ligament size r_c is reached. In this case, S_c is the critical value of the strain energy density factor, which is a material constant related with the fracture toughness of the material.

For linear isotropic elastic material behavior, the shear modulus of elasticity is given by:

$$\mu = \frac{E}{2(1+\nu)} \tag{5-7}$$

where E is the Young modulus and ν is the Poisson ratio.

For Mode I, plane stress problems, the minimum strain energy density factor S_{min} can be expressed as [127]:

$$S_{min} = \frac{(\kappa-1)\sigma^2 \alpha}{8\mu} \tag{5-8}$$

where $\kappa = \frac{3-\nu}{1+\nu}$ for generalized plane stress.

Equating S_{min} with S_c, the following expression for the critical stress σ_c for onset of crack extension is obtained:

$$\sigma_c a^{1/2} = \left(\frac{8\mu S_c}{\kappa-1}\right)^{1/2} \tag{5-9}$$

For a mode I crack the stress intensity factor K_I becomes critical at the condition of unstable extension under plane stress:

$$K_{cr} = \sigma_c Y\sqrt{\pi\alpha} \tag{5-10}$$

71

where factor Y is a function of crack length and structural geometry. In the present analysis Y will be considered equal to 1 (Y=1 for the case of a central crack of length 2a, in an infinite sheet).

With the use of the equation (5-10), equation (5-9) becomes for plane stress:

$$S_c = \frac{(1-v)K_{cr}^2}{2\pi E} \qquad (5\text{-}11)$$

5.1.3 Crack growth under cyclic loading

Assuming that the total plastic energy for fracture (W_f), given from equation (5-4) can be approximated by the critical strain energy per unit volume $(dW/dV)_c$ from the SED criterion in equation (5-6), the following expression for W_f can be derived with the use of equation (5-11):

$$W_f = \frac{(1-v)K_{cr}^2}{2\pi E r_c} \qquad (5\text{-}12)$$

With the use of equations (5-12) and (5-4), the critical number of cycles N_f for a crack increment $\Delta r = r_c$ can be obtained by:

$$N_f = \frac{(1-v)K_{cr}^2(1+n')}{4\pi E r_c \sigma_A \Delta \varepsilon_p (1-n')} \qquad (5\text{-}13)$$

In equation (5-13), σ_A is the stress amplitude at the position of fracture r_c. Assuming small scale plasticity, the stress amplitude σ_A in an isotropic linear elastic material for mode I loading is given by [128]:

$$\sigma_A = \frac{\Delta \sigma_I}{2} = \frac{\Delta \sigma_\infty Y \sqrt{\pi \alpha}}{\sqrt{2\pi r_c}} = \frac{\Delta K}{\sqrt{2\pi r_c}} \qquad (5\text{-}14)$$

where $\Delta \sigma_I$ is the stress range at the position of fracture r_c, and $\Delta \sigma_\infty$ is the macroscopic applied stress range.

With the hypothesis that the average plastic strain range $\Delta \varepsilon_{pm}$ in equation (5-13) for a stabilized hysteresis loop remains constant during cyclic loading, it can be assumed that

$\Delta\varepsilon_{pm} = \Delta\varepsilon_p$, which is evaluated from the Coffin-Manson relationship [61, 62]:

$$\Delta\varepsilon_p = 2\varepsilon_f'\left(2N_f\right)^c \qquad (5\text{-}15)$$

where ε_f' is the fatigue ductility coefficient and c is the fatigue ductility exponent.

With the use of equations (5-14) and (5-15), the critical numbers of cycles for failure can be calculated from:

$$N_f = \left[\frac{(1-v)K_{cr}^2(1+n')\sqrt{2\pi}}{4\pi E\sqrt{r_c}(\Delta K)2^{c+1}\varepsilon_f'(1-n')}\right]^{1/c+1} \qquad (5\text{-}16)$$

With $\Delta N = N_f$, Δr in equation (5-1) becomes r_c. Hence, substitution of equation (5-16) in equation (5-1) leads to the crack growth equation:

$$\frac{d\alpha}{dN} = r_c^{\frac{2c+3}{2c+2}}\left[\frac{4\sqrt{\pi}E2^{\left(c+\frac{1}{2}\right)}(1-n')\varepsilon_f'}{(1-v)K_{cr}^2(1+n')}\right]^{1/c+1}(\Delta K)^{1/c+1} \qquad (5\text{-}17)$$

Equation (5-17) is a Paris-type crack growth law with a more physical interpretation of material constants D and m, which are replaced by actual mechanical properties. For the proposed model the Paris constants D and m are determined from:

$$D = r_c^{\frac{2c+3}{2c+2}}\left[\frac{4\sqrt{\pi}E2^{\left(c+\frac{1}{2}\right)}(1-n')\varepsilon_f'}{(1-v)K_{cr}^2(1+n')}\right]^{1/c+1} \qquad (5\text{-}18)$$

and

$$m = \frac{1}{c+1} \qquad (5\text{-}19)$$

which depend on the material.

Equation (5-17) can be written in the following simplified form:

$$\frac{d\alpha}{dN} = A^k B^m (\Delta K)^m \tag{5-20}$$

where parameter m is expressed by equation (5-19) and

$$A = r_c \tag{5-21}$$

$$k = \frac{2c+3}{2c+2} \tag{5-22}$$

$$B = \left[\frac{4\sqrt{\pi} E 2^{\left(c+\frac{1}{2}\right)}(1-n')\varepsilon_f'}{(1-v)K_{cr}^2(1+n')} \right] \tag{5-23}$$

Parameters n′, K_{cr}, c, ε_f′, E can be determined experimentally.

In applying equation (5-17) to predict fatigue crack growth in the weld material, the microstructural influence is considered in the model using the cyclic strain hardening parameter n′, which has been evaluated in paragraph 4.3.4 for different locations in the HAZ. Parameters K_{cr}, c, ε_f′ also vary inside the HAZ, but in the present analysis they are taken as reference values from initial 2024 T3 material. Parameter A contains the critical distance r_c where the strain energy density factor reaches the critical value S_c. In the SED criterion r_c is used arbitrarily with no physical interpretation, providing that the material behavior is predominantly elastic at the tip of the crack. For ductile materials such condition cannot be fulfilled and small scale plasticity at the tip of the crack is always present. Parameter r_c is correlated here with a physical, measurable parameter during fatigue crack propagation, which is the striation spacing as it will be shown in the next Chapter.

5.2 Modelling the effect of residual stresses on fatigue crack growth

The basic analytical approaches for simulation of residual stresses on FCG problems have been presented in paragraph 2.3. In the present methodology to simulate the effect of residual stresses on FCG, the superposition approach (see paragraph 2.3.2) has been used. In the superposition approach, the maximum K_{max} and minimum K_{min} stress intensity factors are derived from superposition of external loads and residual stresses, and the FCG rates are a

function of the applied stress intensity factor range ΔK_{app} and effective stress ratio R_{eff}. The effective stress ratio R_{eff} is a function of the applied and residual stress intensity factors ($K_{max,app}$, $K_{min,app}$, K_{res}) and can be calculated from equation (2-27). K_{res} and R_{eff} vary with the position of the crack inside the residual stress field.

In the model, to include the effective stress ratio in fatigue crack growth analysis, the crack growth equation proposed by Elber [26, 27] has been implemented, which accounts for the effect of stress ration on fatigue crack growth:

$$\frac{da}{dN} = D^*(U\Delta K)^m \tag{5-24}$$

where

$$U = 0.5 + 0.4R \tag{5-25}$$

m and D^* are material constants. To account for the influence of residual stresses on FCG in equation (5-25) the stress ratio has been replaced by the effective stress ratio R_{eff}.

The variation of residual stress intensity factor, K_{res} is determined with Bueckner's weight function [86], using equation (2-32).

The simultaneous influence of weld microstructure and residual stresses is taken into account using equations (5-20) and (5-24):

$$\frac{d\alpha}{dN} = A^\kappa B^m (U\Delta K)^m \tag{5-26}$$

where parameters A, k, B and U are given by equations (5-21), (5-22), (5-23) and (5-25) respectively. The microstructural influence is considered via the cyclic strain hardening parameter n´ included in parameter B and the influence of residual stresses through the effective stress ratio R_{eff} included in parameter U.

In equation (5-26), the stress intensity factor range ΔK for a C(T) specimen geometry is calculated from [114]:

$$\Delta K = \frac{\Delta P}{B\sqrt{W}} \frac{(2+s)}{(1-s)^{\frac{3}{2}}} (0.886 + 4.64s - 13.32s^2 + 14.72s^3 - 5.6s^4) \tag{5-27}$$

where ΔP is the applied force range, B the specimen's thickness, W the specimen's width

and s = α / W the ratio of crack length to specimen's width.

For the calculation of crack length, a numerical integration of equation (5-26) is performed in the form:

$$a = a_i + \sum_{i=1}^{N_f} \Delta a_i \qquad (5\text{-}28)$$

In equation (5-28), α is the actual crack length, α_i is the crack length before the application of the *i*-th cycle, N_f is the critical number of cycles for failure and $\Delta\alpha_i$ is the crack increment after one cycle of loading. $\Delta\alpha_i$ is calculated for each loading cycle with numerical integration of equation (5-26).

Chapter 6: Fatigue crack growth simulation in FSW

In Chapter 6, the model is used to predict the mode I fatigue crack propagation rate perpendicular to an FSW weld (Figure 1.2). Firstly, the model is implemented to predict fatigue crack growth rate in uniformly heat treated materials A250 and A300, to evaluate the ability of the model to simulate the overaged microstructure on crack propagation rate. Then, the ability of the model to simulate the growth of a fatigue crack propagating in the specimen with the strength gradient is evaluated. Finally, the model is implemented to simulate fatigue crack growth rate in the FSW material. In all cases the analytical predictions are compared with experimental results from Chapter 4. In the analysis, the sensitivity of the model to the value of parameter r_c is examined. Also, the crack growth ligament r_c is compared to the plastic zone size in the C(T) specimen, applicability of small scale plasticity conditions is discussed, and a physical interpretation of parameter r_c is attempted.

6.1 Fatigue crack growth simulation in uniformly heat treated material

Simulation of fatigue crack growth is made using the crack growth equation (5-20) with material parameters given in Table 6.1, from T3 material. To consider the material condition in overaged state (A250 and A300), the cyclic hardening exponent $n´$ for each condition was implemented. As fracture criterion the critical stress intensity factor K_{cr} was used. The quantity r_c is determined from fitting $d\alpha/d$-ΔK data for the T3 material, for the given set of parameters in Table 6.1.

Table 6.1 Parameters of equation (5-20) used in the analysis

Cyclic hardening exponent $n´$	Parameter r_c (m)	Coffin-Manson exponent c	Coffin-Manson parameter $\varepsilon_f´$	critical stress intensity factor K_{cr} (MPam$^{1/2}$)	Young's modulus E (GPa)	Poisson ratio v
T3: 0.042 **A250:** 0.148 **A300:** 0.211	1.291×10^{-6}	-0.6	0.13	60	73.1 taken from [118]	0.33 taken from [118]

The analytical results are shown in Figure 6.1. In A250 a fairly good agreement with experimental data is obtained. In A300 the analysis overestimates the experimental FCG rates. In Table 6.3 the experimental and analytical N_f are compared as mean values.
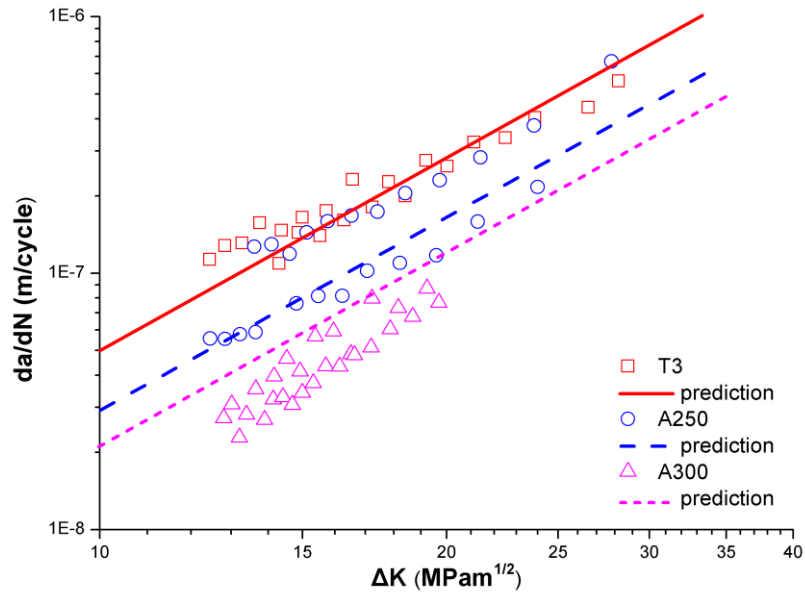
Figure 6.1 Experimental and computed fatigue crack growth rates vs. stress intensity factor range (dα/dN-ΔK) in T3, A250 and A300 materials. The analytical results were obtained for c=-0.6 and r_c=1.291x10^{-6} m.

The results of Figure 6.1 are obtained using a Coffin-Manson parameter value c=-0.6 (Table 6.1). This is an average c value for metallic materials, in the range -0.5 ~ -0.7 [129]. Using in the analysis the mean value c=-0.7 for materials T3, A250 and A300 obtained in paragraph 4.3.4, which lies in the upper bound of the parameter c range [129], parameter r_c is recalculated for fitting T3 data (r_c=1.853x10^{-6} m). For c=-0.7, the behavior of the uniformly heat treated materials is significantly improved (Figure 6.2).
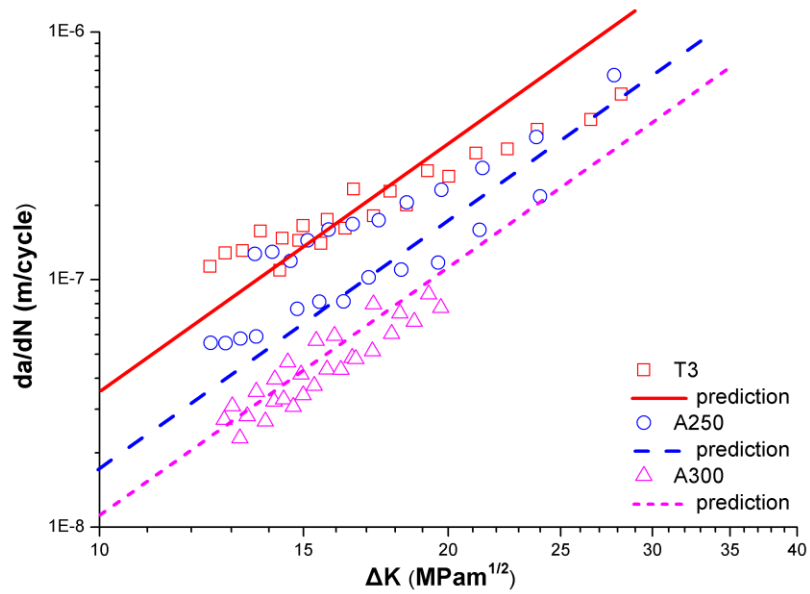
Figure 6.2 Experimental and computed fatigue crack growth rates vs. stress intensity factor range (dα/dN-ΔK) in T3, A250 and A300 materials. The analytical results were obtained for $c=-0.7$ and $r_c=1.853 \times 10^{-6}$ m.

A more detailed examination to investigate the sensitivity of the analytical results on the parameter r_c is performed next. In Table 6.2, the r_c values after fitting the dα/dN-ΔK experimental curves for T3, A250 and A300 materials are given. The values are in the same order of magnitude for all materials and differences are small.

Table 6.2 Values of r_c for T3, A250 and A300 materials for $c=-0.6$

	parameter r_c (m)	
T3	1.291×10^{-6}	*mean:* 1.329×10^{-6}
A250	1.538×10^{-6}	
A300	1.158×10^{-6}	

In Figure 6.3 the analytical dα/dN-ΔK curves are plotted using the mean value of parameter $r_{c,mean}$ from Table 6.2. Comparing the analytical results of Figure 6.3 ($r_{c,mean}$) with the results of Figure 6.1 (r_c from T3 material) the differences are negligible.

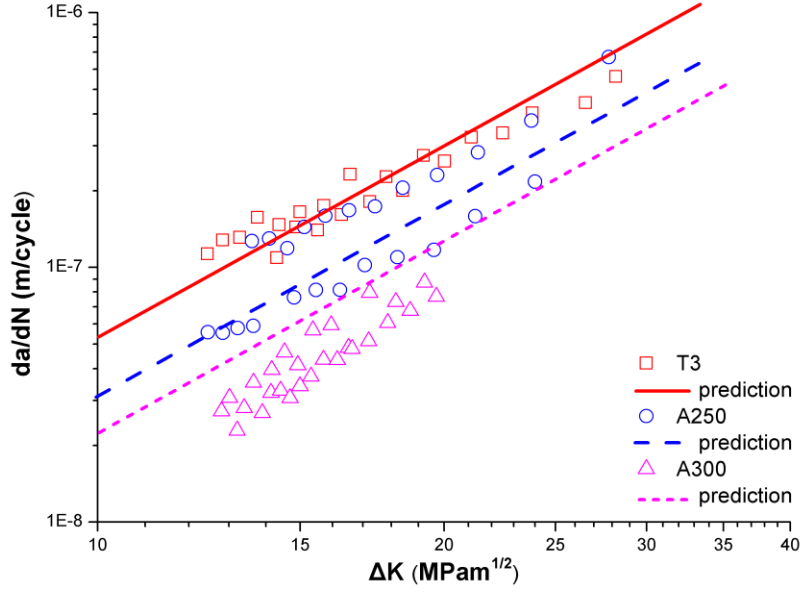**Figure 6.3** Experimental and computed fatigue crack growth rates vs. stress intensity factor range (dα/dN-ΔK) in T3, A250 and A300 materials evaluated for $r_{c,mean}$=1.329x10^{-6} m.

Table 6.3 Experimental (mean values) and analytical results for T3, A250 and A300 materials

			T3	A250	A300
N_f	Experimental		86420	99433	260775
	Analytical	c=-0.6, r_c=1.291x10^{-6} m (Figure 6.1)	86420	147500	204200
		c=-0.7, r_c=1.853x10^{-6} m (Figure 6.2)	86420	176300	272000
		c=-0.6, $r_{c,mean}$=1.329x10^{-6} m (Figure 6.3)	80950	138200	191300

6.1.1 Physical interpretation of parameter r_c

A main assumption in the model is that crack propagation occurs incrementally and the increment is equal to the distance r_c. A physical parameter, which is associated with the magnitude of crack advance during fatigue crack propagation is the striation spacing [24]. It is still controversial whether a single striation spacing corresponds to the damage accumulated during a single loading cycle or after accumulation of several fatigue cycles [130-135]. Based on the assumption used in the model, an attempt is made to correlate distance r_c with measured striation spacings from fractographic images. In the micrographs of Figures 6.4a and 6.4b, fatigue striations observed on the fracture surface of 2024 T3 specimen taken with SEM at ΔK values corresponding to ΔK=11 MPam$^{1/2}$ and 20 MPam$^{1/2}$ are shown. The mean striation spacing is 1.5x10^{-6} m. The mean value of r_c for T3, A250 and A300 is $r_{c,mean}$=1.329x10^{-6} m (Table 6.2). Comparing the $r_{c,mean}$ value with the mean striation spacing, the agreement is very good. Also, the small differences observed in striation spacings as the

crack propagates from a ΔK value $\Delta K=11$ MPam$^{1/2}$ to a $\Delta K=20$ MPam$^{1/2}$ make the use of a constant r_c in the analysis rational. This observation renders the use of r_c as a fitting parameter in the present analysis not arbitrary and provides a physical meaning for it, based on experimental evidence.

(a)   (b)
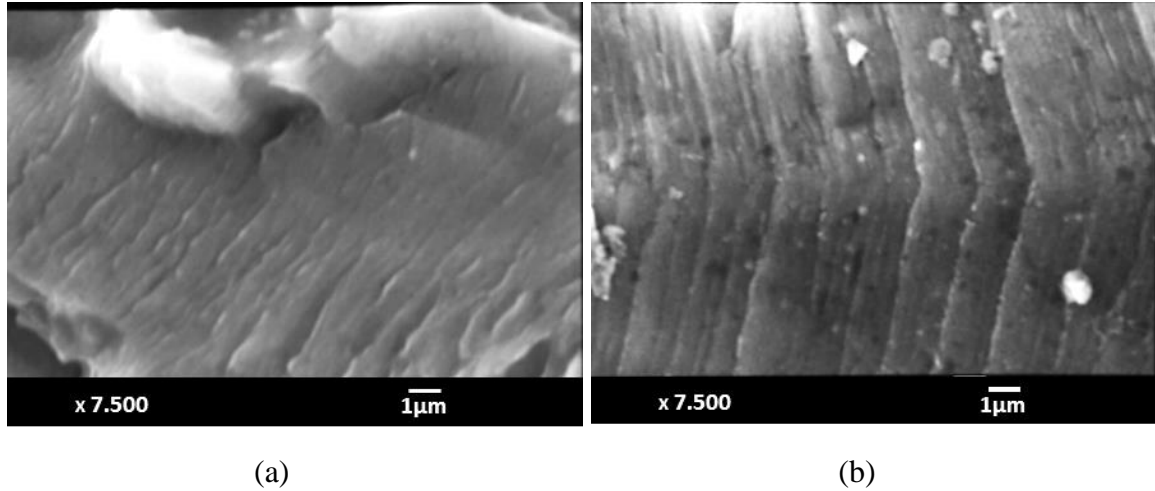
Figure 6.4 SEM micrographs showing fatigue striations on fracture surface during FCG in 2024 T3 AA at stress intensity factor range a) $\Delta K=11$ MPam$^{1/2}$ b) $\Delta K=20$ MPam$^{1/2}$.

6.1.2 Comparison of parameter r_c with the size of the plastic zone

In the SED criterion parameter r_c is used arbitrarily with no physical interpretation, providing that the material behavior is predominantly elastic. For ductile materials such condition cannot be fulfilled and small scale plasticity is always present at the tip of the crack. A comparison of the r_c value to the plastic zone size associated to the geometry and loading condition of the C(T) specimen is performed in this paragraph. The size of the monotonic (r_y) and cyclic plastic zone (r_{cy}) under plane stress conditions was determined. The plastic zone size was evaluated at the initial stage of fatigue crack growth at a ΔK value of 11 MPam$^{1/2}$ using the formulation [129]:

$$r_y = \frac{1}{2\pi}\left(\frac{K_{max}}{\sigma_{y0.2}}\right)^2 \qquad (6\text{-}1)$$

$$r_{cy} = \frac{1}{8\pi}\left(\frac{K_{max}}{\sigma_{y0.2}}\right)^2 \qquad (6\text{-}2)$$

Parameter r_c in the present analysis has a mean value of $r_{c,mean}=1.329\text{x}10^{-6}$ m. The comparison

of plastic zone size and parameter r_c is shown in Table 6.4.

Table 6.4 Comparison of monotonic & cyclic plastic zone size at $\Delta K=11\text{MPam}^{1/2}$ ($K_{max}=12\text{MPam}^{1/2}$) with parameter r_c in 2024 T3 AA

	r_y (mm)	r_{cy} (mm)	$r_{c,mean}$ (mm)
2024 T3	163.057 x10^{-6}	40.764 x10^{-6}	1.329x10^{-6}

The size of cyclic plastic zone is significantly larger, which means that distance r_c is trapped in an area where small scale plasticity prevails. This point provides a small controversy for the application of the SED criterion. On the other hand, linear elastic (LEFM) conditions based on the ASTM standard for the C(T) specimen configuration exist [114]. A strong case for using parameter r_c in the model is that it correlates very well with the size of the striation spacing observed experimentally, which is a physical, measurable parameter during fatigue crack propagation.

6.1.3 Fatigue crack growth analysis in specimen with hardness (strength) gradient

The ability of the model to predict FCG in the C(T) specimen with a strength gradient is examined in this paragraph, to further assess the ability of the model to simulate FCG in the HAZ.

In this case, the variation of cyclic strain hardening exponent n´ within the gradient was considered. In order to use the variation of n´ as input in the model, firstly the microhardness gradient at the crack path was determined (Figure 6.5) and was correlated empirically with the variation of local strength. The hardness values of the uniformly heat treated materials were related to the local yield strength values in the HAZ using the empirical equation:

$$\sigma_y = 3Hv - 90 \qquad (6\text{-}3)$$

which was obtained from the experimental findings in paragraphs 4.1.2 and 4.3.1. Then, the value n´ inside the gradient was calculated from linear interpolation (equation in Figure 6.6). The calculated path is shown in Figure 6.7. A linear dependency of n´ value from the local yield strength inside the gradient is considered, which is given in Figure 6.6.
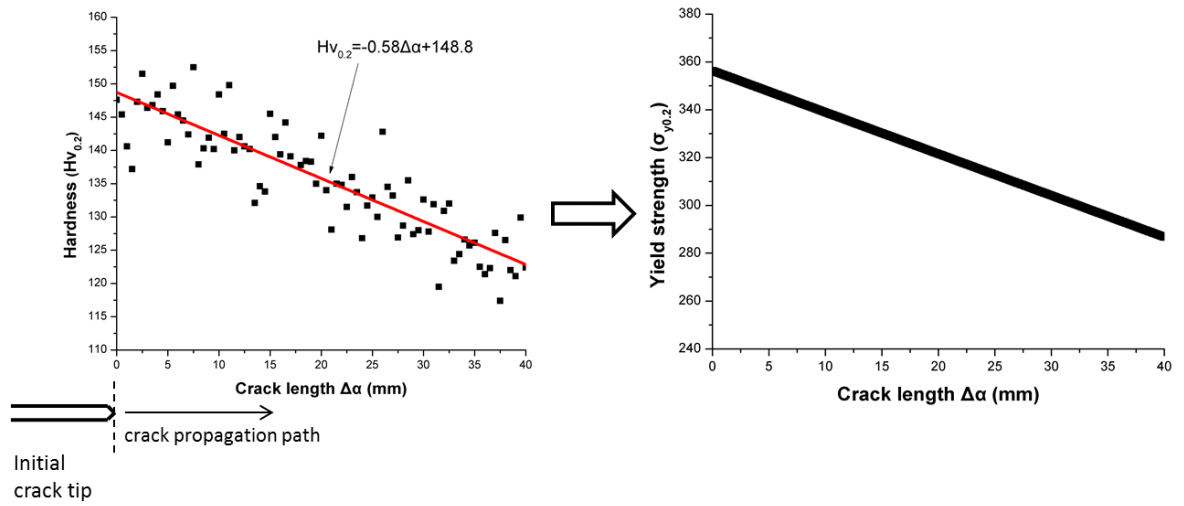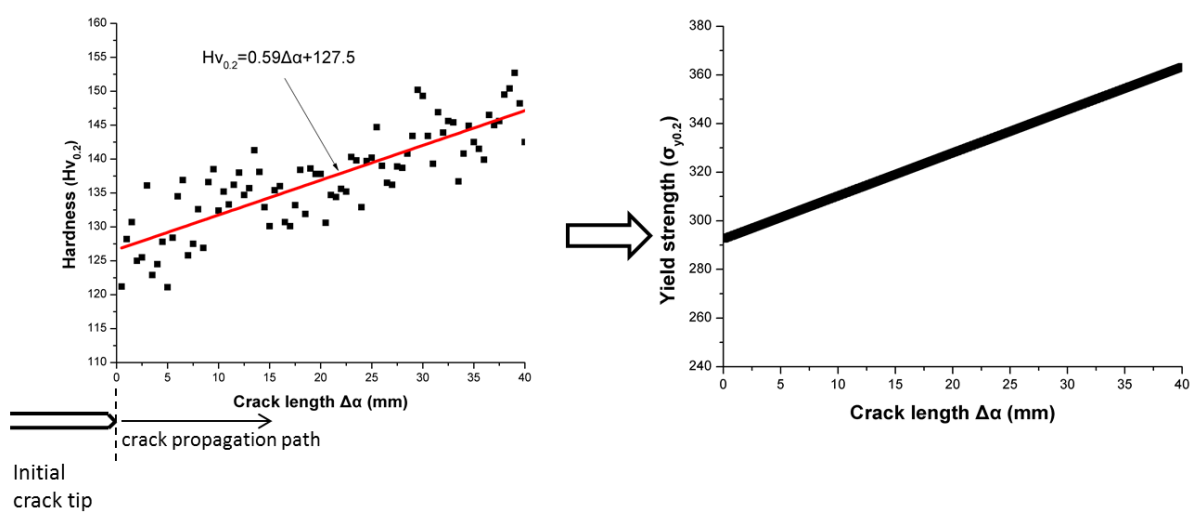
Figure 6.5 Hardness and yield strength profiles of specimens with (a) negative and (b) positive strength gradient
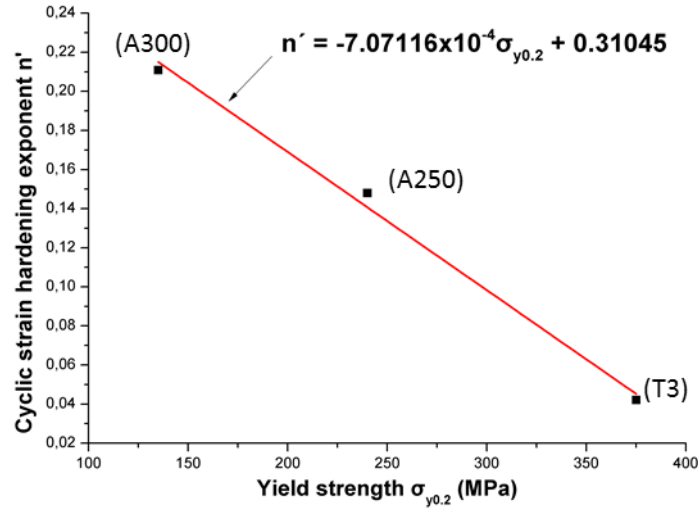
Figure 6.6 Empirical correlation between the cyclic strain hardening exponent (n´) and the yield strength ($\sigma_{y0.2}$) for 2024 material

$Hv_{0.2}=f(\Delta\alpha)$ variation of hardness with regard to crack length (equation in Figure 6.6)

$\sigma_{y0.2} =f(Hv_{0.2})$ variation of local yield strength with regard to hardness variation (equation (6-3))

$n´=f(\sigma_{y0.2})$ variation of cyclic hardening exponent n´ with regard to local yield strength (equation in Figure 6.7)

input in the model (equation (5-20))
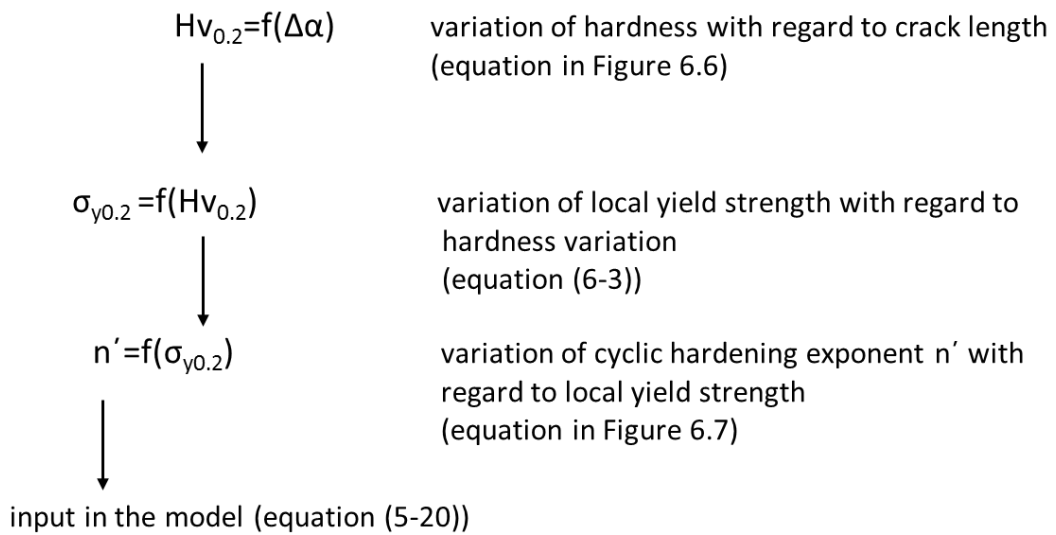
Figure 6.7 Calculation path of cyclic strain hardening exponent n´.

The results are shown in Figures 6.8a and 6.8b. The analytical prediction underestimates the rate of FCG in the positive gradient and describes fairly well the behavior in the negative gradient lying on the lower bound of experimental crack growth results. Further investigation is required to explain the inconsistency observed, especially in the case of positive gradient. The role of plastic zone size interaction due to the change in local yield strength is another mechanism that may influence the results.
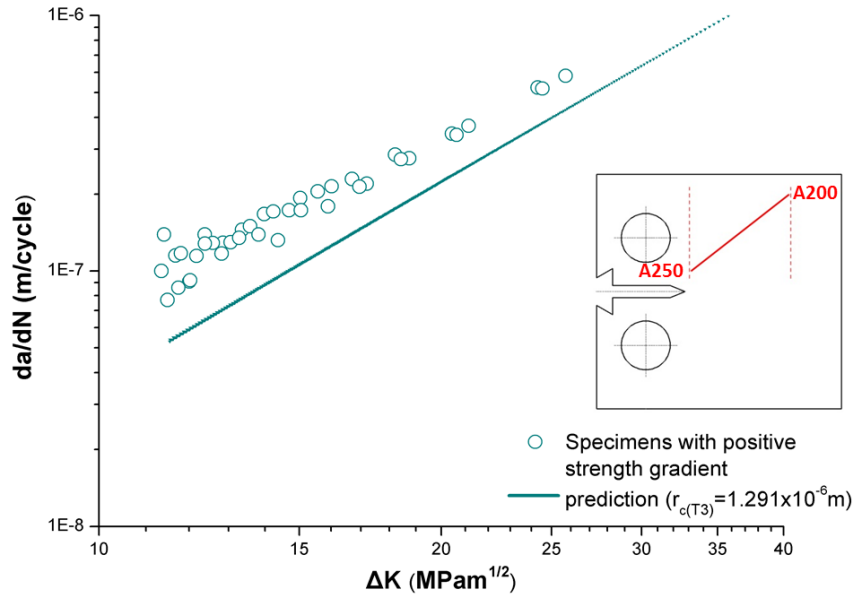
(a)
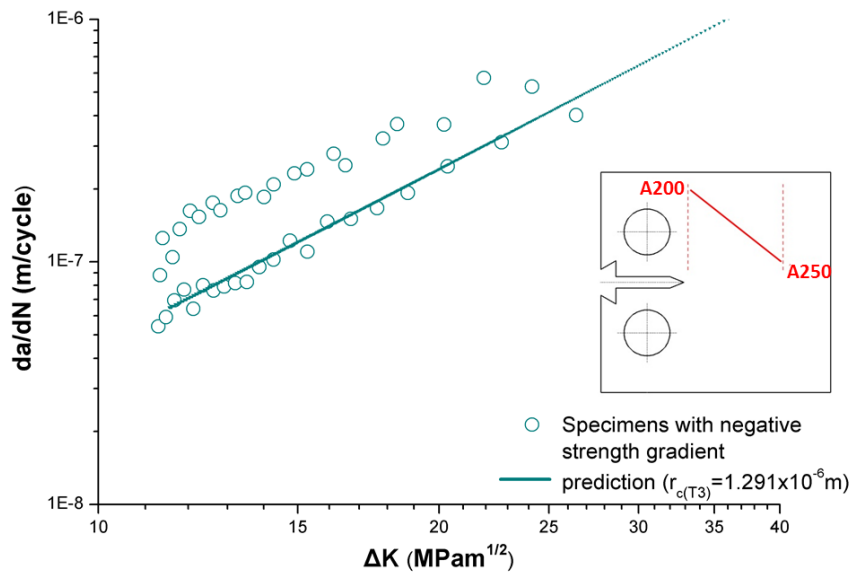
(b)

Figure 6.8 Experimental and analytical fatigue crack growth rates vs. stress intensity factor range (dα/dN-ΔK) in material with (a) positive and (b) negative strength gradient. The analytical results were obtained for r_c=1.291x10^{-6} m for T3 material.

6.2 Fatigue crack growth analysis in 2024 AA friction stir weld

In this paragraph the simulations for the configurations FSW#1, FSW#2 and FSW#3 are presented. The variation of the cyclic strain hardening exponent n´ at the crack front (using the calculation path shown in Figure 6.7), was determined from the actual microhardness gradients for FSW#1 and FSW#3 configurations (Figure 6.9). The inclusion of residual

stresses in the simulation makes the use of parameter U in equation (5-26) necessary. After fitting the experimental dα/dN-ΔK curve for T3 material using equation (5-26), the new r_c value is 4.004×10^{-6} m which is 2.1 times larger than the value without the effect of residual stresses, but in the same order of magnitude. The properties of equation (5-26) were taken from 2024 T3 material.

Table 6.5 Parameter values of equation (5-26) used for fatigue crack growth prediction in FSW

Parameter r_c (m)	Coffin Manson exponent c	Coffin Manson parameter ε_f'	critical stress intensity factor K_{cr} (MPam$^{1/2}$)	Young's modulus E (GPa)	Poisson ratio ν
4.004×10^{-6}	-0.7	0.13	60	73.1	0.33

(a)

(b)
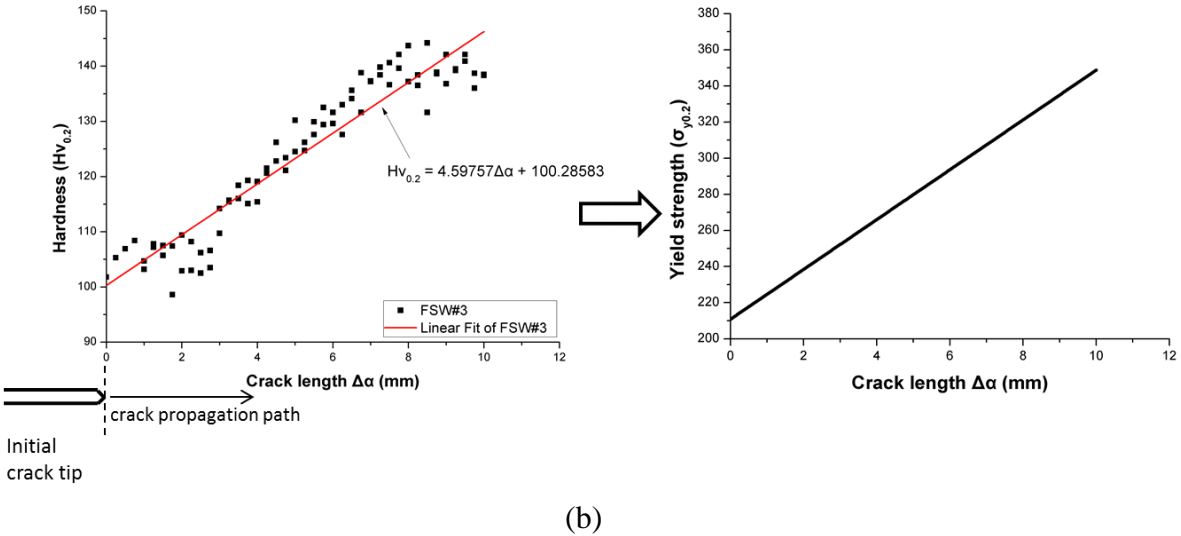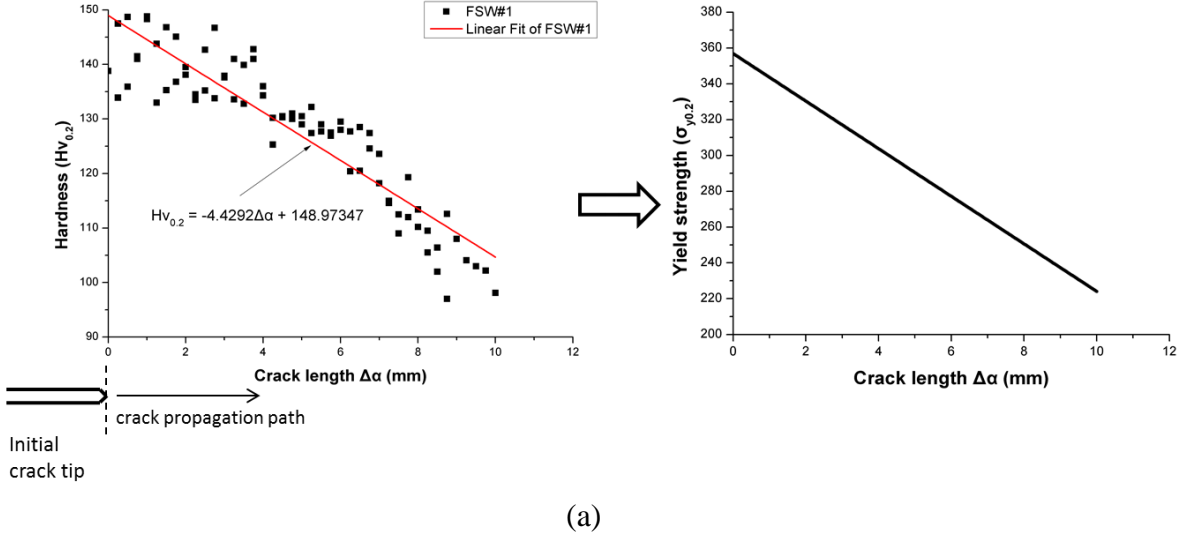
Figure 6.9 Hardness and yield strength profiles of specimens (a) FSW#1 (b) FSW#3

The residual stress distribution at the front of the crack for FSW#1, FSW#2 and FSW#3 is approximated with a linear fitting using a symmetric profile with respect to the weld line as shown in Figure 6.10.
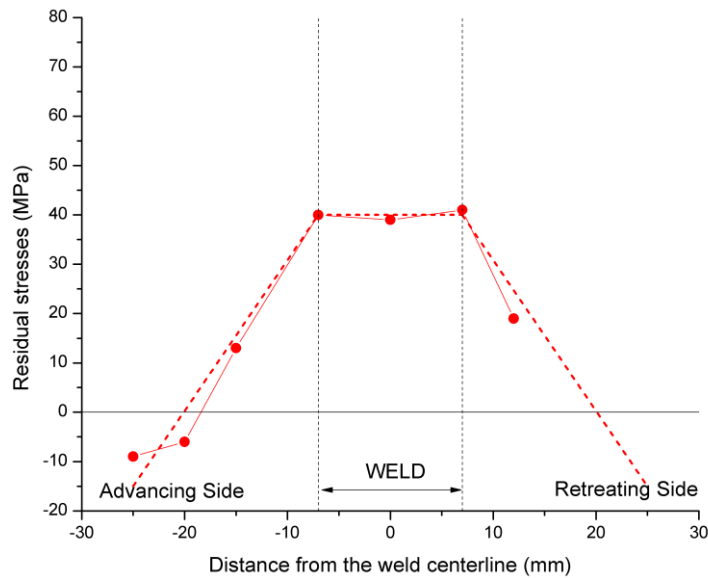
Figure 6.10 Longitudinal residual stress distribution measured in the welded panel (75x72mm) without notch. The linear approximation is presented with the dotted line.

In Figures 6.11a-c the residual stress distribution at the crack path for configurations FSW#1, FSW#2 and FSW#3 is presented. The distribution accounts for the stresses that would exist along the crack plane if the crack was not there and was used to calculate the stress intensity factor K_{res}. The variation in R_{eff} has been approximated with a polynomial regression analysis (Figure 6.12a-c). In FSW#1 (Figure 6.12a), R_{eff} continuously increases with crack length between the values 0.05 and 0.3. In FSW#2 and FSW#3, the high tensile residual stresses along the crack plane lead to higher R_{eff} values compared to FSW#1. Also, R_{eff} decreases after a certain crack length due to the decrease of residual stresses as shown in Figures 6.11b and 6.11c.
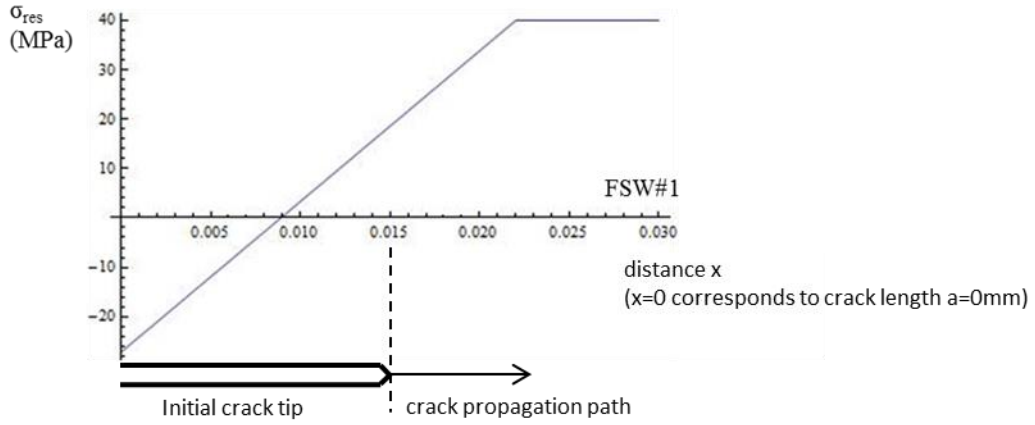
(a)
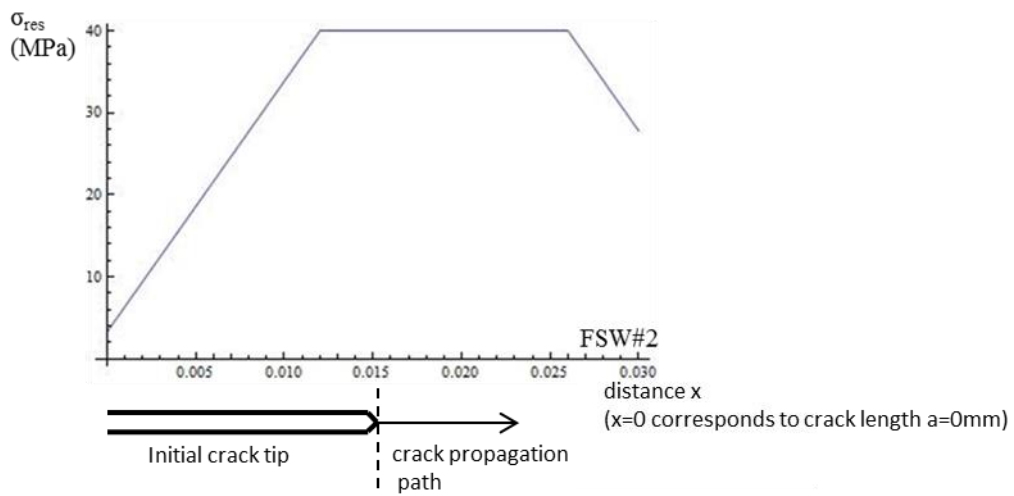
(b)
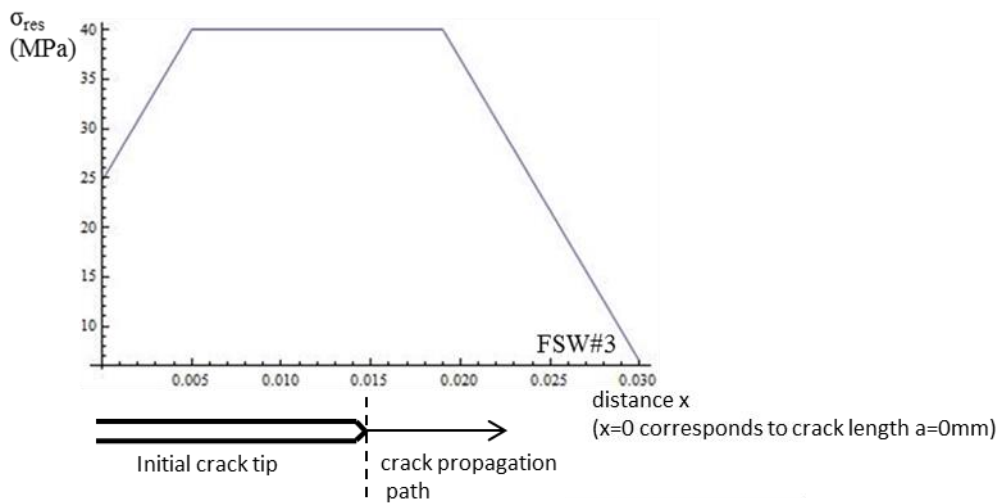
(c)

Figure 6.11 Stress distribution $\sigma_{res}(x)$ at the crack path (a) FSW#1 (b) FSW#2 (c) FSW#3.
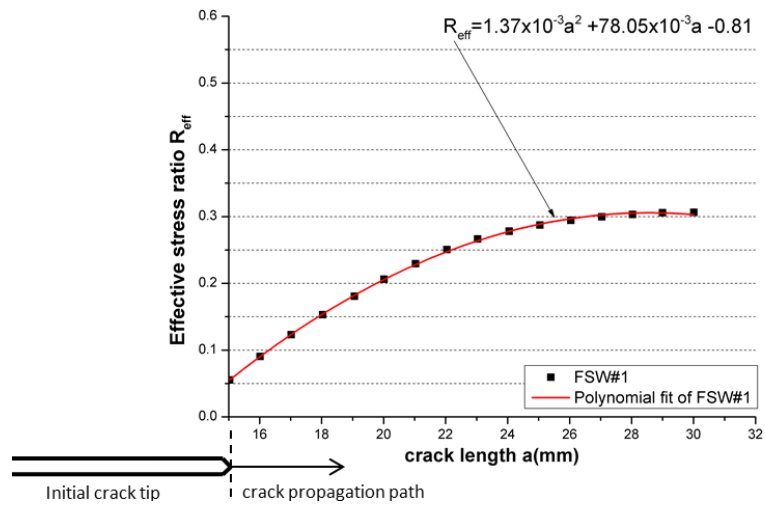
(a)
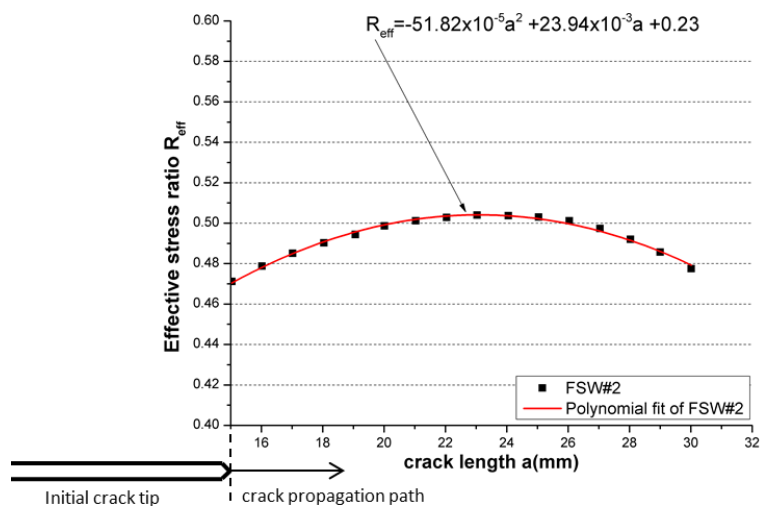
(b)
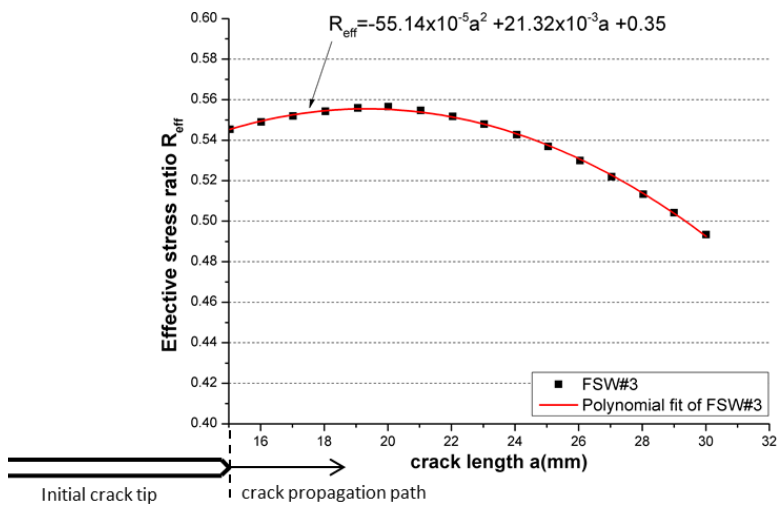
(c)

Figure 6.12 Variation of effective stress ratio with regard to the crack length (a) FSW#1, (b) FSW#2, (c) FSW#3.

The analytical predictions of Figure 6.13 are conducted without taking into account the weld microstructure and show the ability of the model to consider the effect of residual stresses. In FSW#1, which has the lowest R_{eff} values, the fatigue crack growth rates are lower than FSW#2 and FSW#3.
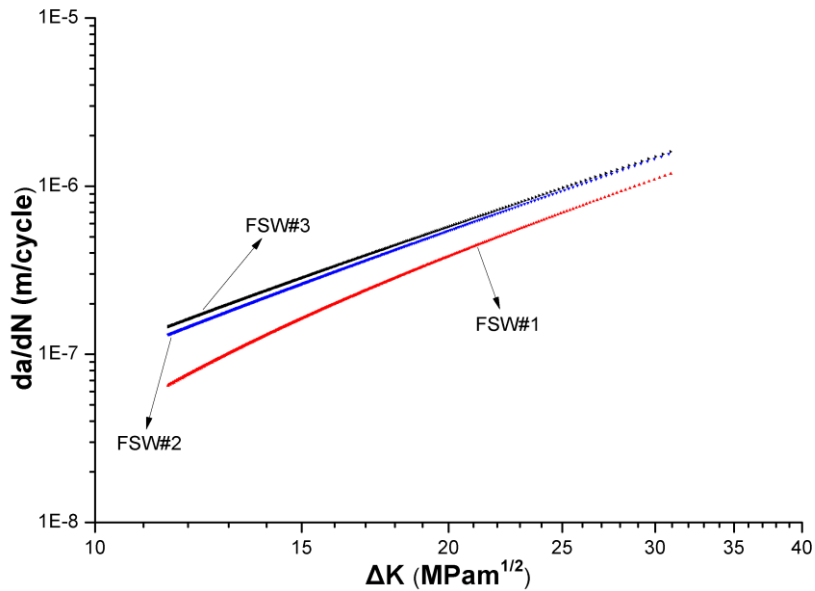
Figure 6.13 Prediction of fatigue crack growth in FSW#1, FSW#2 and FSW#3 considering only the effect of residual stresses.

The analytical predictions accounting for both residual stresses and weld microstructure are compared with experimental data in Figures 6.14-6.16. Also, in Figures 6.14-6.16 each effect is separately plotted for better understanding.

In FSW#1 using only residual stresses, the simulation overestimates FCG rates (Figure 6.14). By accounting in the analysis also for the weld microstructure (local property variation via parameter n´) the behavior is corrected and crack growth rates compare well with the experiment. The crack plane is subjected to a low tensile residual stress field (Figure 6.11a) and therefore the effect of microstructural variation is significant (Figure 6.9a).
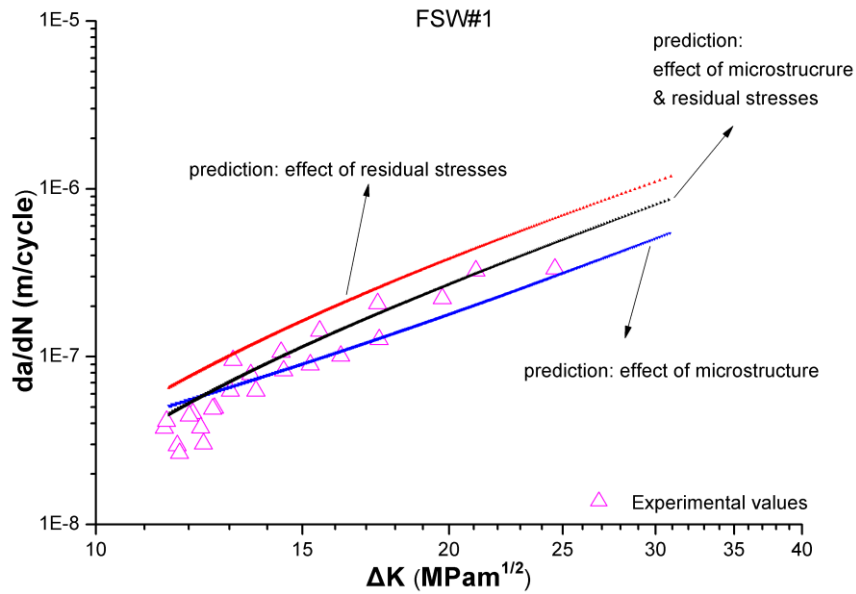
Figure 6.14 Prediction of fatigue crack growth of FSW 2024 AA, case FSW#1.

In FSW#3 using only the effect of residual stresses, the prediction agrees well with the experiment (Figure 6.15), which indicates that microstructural influences are diminished due to the dominant effect of high tensile residual stresses (Figures 6.11c and 6.12c).
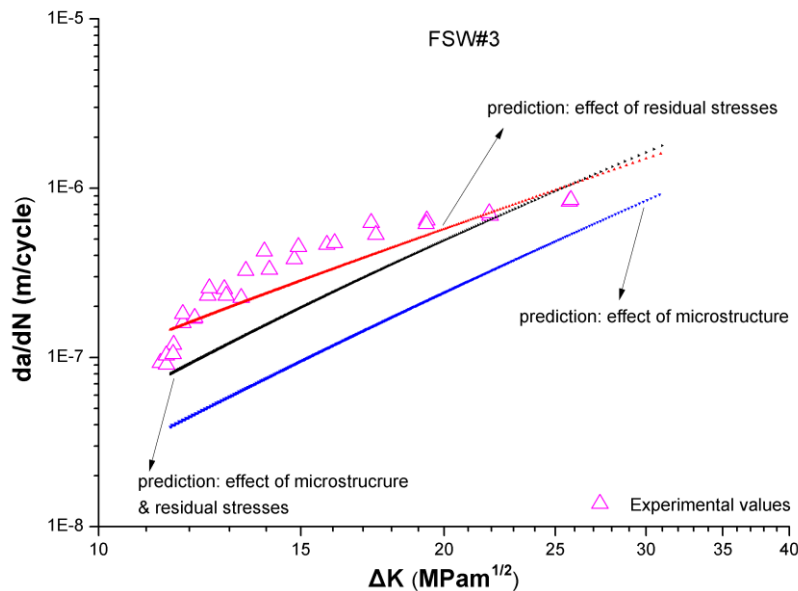
Figure 6.15 Prediction of fatigue crack growth of FSW 2024 AA, case FSW#3.

In FSW#2, again, considering only the residual stresses, the prediction agrees well with the experiment (Figure 6.16). Here, the high tensile residual stress field that exists in the crack plane (Figure 6.11b) leads to high R_{eff} values (Figure 6.12b), and is the major parameter

91

controlling FCG. Analytical results considering the effect of the weld nugget's microstructure on FCG, which is relevant in this case, are not available. However, the magnitude of tensile residual stresses renders the weld nugget influence not significant as obtained from Figure 6.16.
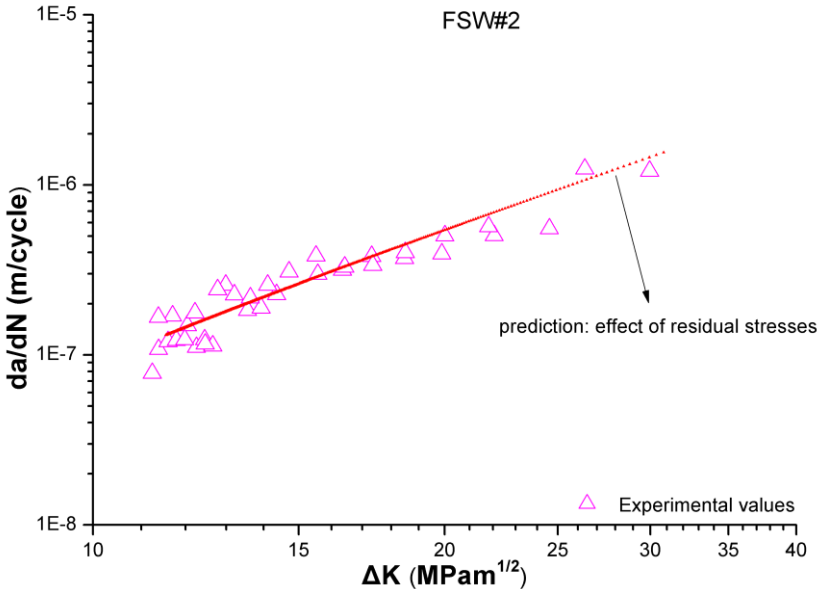
Figure 6.16 Prediction of fatigue crack growth of FSW 2024 AA, case FSW#2.

The analytical results show that the proposed model has the ability to predict satisfactory the experimental FCG rates in the weld region for a mode I crack propagation problem. The dominant factors influencing crack growth rate are the magnitude of residual stresses and the position of the crack inside the weld region. Using the $d\alpha/dN$-ΔK results of Figures 6.14-6.16 and residual stress profiles of configurations FSW#1, FSW#2 and FSW#3 in Figure 6.11, a threshold for the effective stress ratio R_{eff} can be obtained, signifying when the influence of residual stresses is the dominant factor on FCG rate. For a residual stress profile with an effective stress ratio higher than 0.3, the major influence on FCG are the residual stresses (Figure 6.17). For effective stress ratio values lower than 0.3, solely the effect of residual stresses cannot predict accurately the FCG behavior and the microstructural influence must also be considered. The above observations are valid for the ΔK range examined in the present analysis (11-25MPam$^{1/2}$).
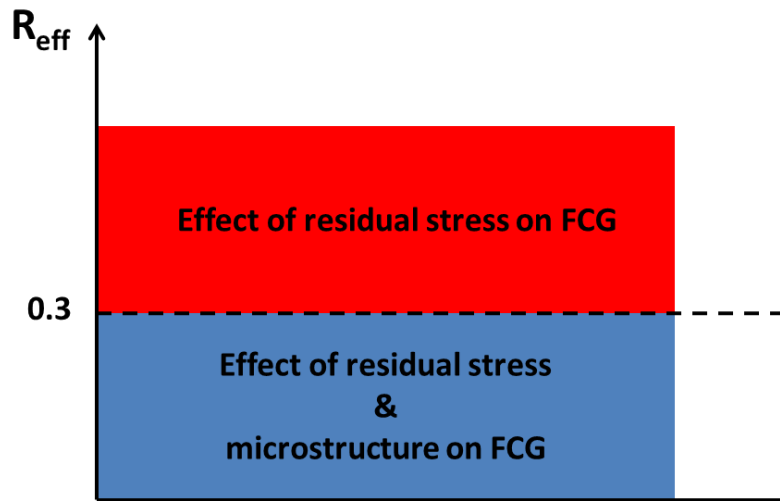
Figure 6.17 R_{eff} threshold showing the importance of residual stresses on FCG in the present analysis.

Chapter 7: Conclusions & Recommendations for further study

In the pursuit of attractive solutions to achieve lighter and low cost airframes in aircraft industry, the use of advanced welding concepts for the "Integral Structure" or "Rivet-Free" aluminum alloy airframes has been considered as a promising technology. Lighter and cost efficient new airframes can be produced with the use of advanced welding technologies such as friction stir welding (FSW) and development of aluminum alloys with improved performances. Already for conventional riveted joints extensive amount of knowledge has been accumulated in the damage tolerance analysis (fatigue crack initiation and growth, residual strength aspects etc.). In this work, new results are provided for the damage tolerance behavior in 2024 T3 aluminum alloy FSW and an analytical model is proposed for prediction of mode I fatigue crack propagation perpendicular to friction stir weld.

In the analysis the role of modified due to welding microstructure and residual stresses on fatigue crack propagation rate has been assessed. The influence of weld microstructure on FCG was examined by simulating the HAZ microstructure in a parent 2024 T3 material with appropriate overaging treatment. The basic conclusions resulting from the experimental investigation in the thesis are the following:

- In the uniformly overaged material fatigue crack growth rates were lower compared to the base metal and were associated with high crack closure levels. Lower fatigue crack growth rates were associated with higher overaging temperatures corresponding to HAZ regions approaching the weld nugget.
- The uniformly overaged material exhibits superior LCF behavior and increased cyclic strain hardening compared to the base metal (2024 T3 alloy) that is associated with higher levels of crack closure compared to the base alloy.
- Low tensile residual stresses prevail in the boundary of BM with HAZ, which result in low fatigue crack growth rates.
- High tensile residual stresses prevail in the weld nugget, which result in high crack propagation rates.

In the analytical part of the thesis, a model was developed for fatigue crack propagation prediction in the FSW under mode I loading. The proposed model takes into account the combined effect of weld microstructure and residual stress profile for the calculation of fatigue crack growth rate. Evaluation of the model was made by comparing the analytical

predictions with experimental data. The main findings that resulted from the analytical investigation are:

- The proposed analytical model has the ability to predict satisfactory the fatigue crack growth behavior inside the FSW region considering the independent effect of weld microstructure and residual stresses on fatigue crack propagation.

- In the proposed model an attempt is made to give a physical meaning for the increment of the growing fatigue crack. It is correlated quantitatively to the striation spacing observed experimentally during fatigue crack growth.

- An effective stress ratio threshold is estimated for the specimen and loading configuration examined, which indicates when the effect of residual stresses is dominant on fatigue crack propagation and when microstructural influences should be accounted for in the analysis.

- For the configuration examined, the residual stress field plays the dominant role on fatigue crack growth in the weld when the effective stress ratio is higher than 0.3. For lower values, the weld microstructure needs to be taken into account for fatigue crack growth prediction.

7.1 Recommendations for further study

In this paragraph, some aspects recommended for further study in the field of damage tolerance behavior of aluminum alloy friction stir welding are presented in brief. They include:

- More detailed investigation of the influence of the weld nugget microstructure on fatigue crack propagation.

- Investigation of the combined influence of cyclic hardening effect and residual stresses due to crack tip plasticity on crack growth rate, and how these mechanisms interact.

- Calculation of the redistribution of residual stresses during crack propagation in the weld region.

- Application of the model to other material types, different welding parameters, or fracture modes in order to evaluate its ability to predict different experimental cases.

References

1. EU-Project WEL-AIR 'Development of Short Distance Welding Concepts for Airframes'. 2004-2007.

2. P.F. Mendez, T.W.E., New trends in Welding in the Aeronaitic Industry, in 2nd Conference of New Manufacturing Trends. 2002.

3. The Welding Institute (TWI). Available from: http://www.twi,co.uk.

4. Damage Tolerance and Fatigue (JAR 25.571), Transport Airplane and Engine Issue Area General Structures Harmonization Working Group, Federal Aviation Administration Aviation Rulemaking Advisory Committee. 2005.

5. W.M. Thomas, E.D.N., J.C. Needham, M.G. Murch, P. Temple-Smith, and C.J. Dawes, Friction Stir Butt Welding, No. PCT/GB92/02203, I.P. Application, Editor. 1991.

6. Thomas, W.M. and E.D. Nicholas, Friction stir welding for the transportation industries. Materials & Design, 1997. 18(4–6): p. 269-273.

7. Cho, J.-H., D.E. Boyce, and P.R. Dawson, Modeling strain hardening and texture evolution in friction stir welding of stainless steel. Materials Science and Engineering: A, 2005. 398(1–2): p. 146-163.

8. Liu, H.J., et al., Tensile properties and fracture locations of friction-stir-welded joints of 2017-T351 aluminum alloy. Journal of Materials Processing Technology, 2003. 142(3): p. 692-696.

9. Lee, W.-B., et al., Microstructural investigation of friction stir welded pure titanium. Materials Letters, 2005. 59(26): p. 3315-3318.

10. Su, J.Q., et al., Microstructural investigation of friction stir welded 7050-T651 aluminium. Acta Materialia, 2003. 51(3): p. 713-729.

11. Frigaard, Ø., Ø. Grong, and O.T. Midling, A process model for friction stir welding of age hardening aluminum alloys. Metallurgical and Materials Transactions A, 2001. 32(5): p. 1189-1200.

12. Mahoney, M.W., et al., Properties of friction-stir-welded 7075 T651 aluminum. Metallurgical and Materials Transactions A, 1998. 29(7): p. 1955-1964.

13. Rhodes, C.G., et al., Effects of friction stir welding on microstructure of 7075 aluminum. Scripta Materialia, 1997. 36(1): p. 69-75.

14. Liu, G., et al., Microstructural aspects of the friction-stir welding of 6061-T6 aluminum. Scripta Materialia, 1997. 37(3): p. 355-361.

15. Jata, K.V. and S.L. Semiatin, Continuous dynamic recrystallization during friction stir welding of high strength aluminum alloys. Scripta Materialia, 2000. 43(8): p. 743-749.

16. Masaki, K., et al., Experimental simulation of recrystallized microstructure in friction stir welded Al alloy using a plane-strain compression test. Scripta Materialia, 2008. 58(5): p. 355-360.

17. Vilaça, P., J. Gandra, and C. Vidal, Linear Friction Based Processing Technologies for Aluminum Alloys: Surfacing, Stir Welding and Stir Channeling. Aluminium Alloys -

New Trends in Fabrication and Applications. 2012.

18. Elangovan, K., V. Balasubramanian, and M. Valliappan, Influences of tool pin profile and axial force on the formation of friction stir processing zone in AA6061 aluminium alloy. The International Journal of Advanced Manufacturing Technology, 2008. 38(3-4): p. 285-295.

19. Bird, C., O. Dupuis, and A. Lamarre, New developments of the ultrasound phased array for the evaluation of friction stir welds. et al., Friction stir welding and processing, vol. IIThe Minerals, Metals & Materials Society, Warrendale, 2003: p. 135-141.

20. Oosterkamp, A., L.D. Oosterkamp, and A. Nordeide, Kissing bond'phenomena in solid-state welds of aluminum alloys. WELDING JOURNAL-NEW YORK-, 2004. 83(8): p. 225-S.

21. Paris, P. and F. Erdogan, A Critical Analysis of Crack Propagation Laws. Journal of Fluids Engineering, 1963. 85(4): p. 528-533.

22. Forman, R.G., V.E. Kearney, and R.M. Engle, Numerical Analysis of Crack Propagation in Cyclic-Loaded Structures. Journal of Fluids Engineering, 1967. 89(3): p. 459-463.

23. Walker, K., The effect of stress ratio during crack propagation and fatigue for 2024-T3 and 7075-T6 aluminum. Effects of environment and complex load history on fatigue life, ASTM STP, 1970. 462: p. 1-14.

24. Suresh, S., Fatigue of Materials. 1998: Cambridge University Press.

25. Dowling, N.E., Mechanical Behavior of Materials: Engineering Methods for Deformation, Fracture, and Fatigue. 2007: Pearson Prentice Hall.

26. Elber, W., The significance of fatigue crack growth Vol. 486. 1971: ASTM STP

27. Elber, W., Fatigue crack closure under cyclic tension. Engineering Fracture Mechanics, 1970. 2(1): p. 37-45.

28. Kemp, R.M.J., Fatigue Crack Closure – A Review, TR 90046 ICAF 1776, R.A. Establishment, Editor. 1990.

29. Kim, J.H. and S.B. Lee, Behavior of plasticity-induced crack closure and roughness-induced crack closure in aluminum alloy. International Journal of Fatigue, 2001. 23, Supplement 1(0): p. 247-251.

30. Katcher, M. and M. Kaplan, Effect of R factor and crack closure on fatigue crack growth for aluminium and titanium alloys. ASTM STP, 1974. 559: p. 264-282.

31. Davidson, D.L., Fatigue crack closure. Engineering Fracture Mechanics, 1991. 38(6): p. 393-402.

32. Gan, D. and J. Weertman, Crack closure and crack propagation rates in 7050 aluminum. Engineering Fracture Mechanics, 1981. 15(1–2): p. 87-106.

33. Gray, G.T., J.C. Williams, and A.W. Thompson, Roughness-Induced Crack Closure: An Explanation for Microstructurally Sensitive Fatigue Crack Growth. Metallurgical Transactions A, 1983. 14(2): p. 421-433.

34. Minakawa, K. and A.J. McEvily, On crack closure in the near-threshold region. Scripta Metallurgica, 1981. 15(6): p. 633-636.

35. Ritchie, R.O. and S. Suresh, Some considerations on fatigue crack closure at near-threshold stress intensities due to fracture surface morphology. Metallurgical Transactions A, 1982. 13(5): p. 937-940.

36. Pokluda, J. and R. Pippan, Analysis of roughness-induced crack closure based on asymmetric crack-wake plasticity and size ratio effect. Materials Science and Engineering: A, 2007. 462(1–2): p. 355-358.

37. Pippan, R., et al., Asymmetric crack wake plasticity – a reason for roughness induced crack closure. Acta Materialia, 2004. 52(15): p. 4493-4502.

38. Venkateswara Rao, K.T., et al., A comparison of fatigue-crack propagation behavior in sheet and plate aluminum-lithium alloys. Materials Science and Engineering: A, 1991. 141(1): p. 39-48.

39. Kamp, N., et al., Influence of grain structure and slip planarity on fatigue crack growth in low alloying artificially aged 2xxx aluminium alloys. International Journal of Fatigue, 2007. 29(5): p. 869-878.

40. Kermanidis, A.T. and S.G. Pantelakis, Prediction of crack growth following a single overload in aluminum alloy with sheet and plate microstructure. Engineering Fracture Mechanics, 2011. 78(11): p. 2325-2337.

41. Budiansky, B. and J.W. Hutchinson, Analysis of Closure in Fatigue Crack Growth. Journal of Applied Mechanics, 1978. 45(2): p. 267-276.

42. Pommier, S., Plane strain crack closure and cyclic hardening. Engineering Fracture Mechanics, 2002. 69(1): p. 25-44.

43. Chang, T. and W. Guo, Effects of strain hardening and stress state on fatigue crack closure. International Journal of Fatigue, 1999. 21(9): p. 881-888.

44. Simar, A., et al., Sequential modeling of local precipitation, strength and strain hardening in friction stir welds of an aluminum alloy 6005A-T6. Acta Materialia, 2007. 55(18): p. 6133-6143.

45. Committee, A.I.H., ASM handbook: Heat treating. 1991: ASM International.

46. Reifsnider, K. and M. Kahl, Effect of local yield strength gradients on fatigue crack propagation. International Journal of Mechanical Sciences, 1974. 16(2): p. 105-119.

47. Nicholls, D.J., THE RELATION BETWEEN CRACK BLUNTING AND FATIGUE CRACK GROWTH RATES. Fatigue & Fracture of Engineering Materials & Structures, 1994. 17(4): p. 459-467.

48. Suresh, S. and R.O. Ritchie, A geometric model for fatigue crack closure induced by fracture surface roughness. Metallurgical Transactions A, 1982. 13(9): p. 1627-1631.

49. Laird, C., The influence of metallurgical structure on the mechanisms of fatigue crack propagation. PAPER FROM FATIGUE CRACK PROPAGATION, ASTM STP NO 415. 1967, 131-180, 1967.

50. Pelloux, R., Mechanisms of formation of ductile fatigue striations. ASM Trans Quart, 1969. 62(1): p. 281-285.

51. Nicholls, D.J., Prediction of fatigue crack growth rates based on crack blunting. Engineering Fracture Mechanics, 1994. 48(1): p. 9-15.

52. Rice, J.R., Mechanics of crack tip deformation and extension by fatigue. In fatigue

Crack propagation. Special Technical Publication, American Society for Testing and Materials 1967. 415: p. 247-309.

53. Weertman, J., Rate of growth of fatigue cracks calculated from the theory of infinitesimal dislocations distributed on a plane. International Journal of Fracture Mechanics, 1966. 2(2): p. 460-467.

54. Wu, S.-X., Y.-W. Mai, and B. Cotterell, A model of fatigue crack growth based on Dugdale model and damage accumulation. International Journal of Fracture, 1992. 57(3): p. 253-267.

55. Kermanidis, A.T. and S.G. Pantelakis, Fatigue crack growth analysis of 2024 T3 aluminium specimens under aircraft service spectra. Fatigue & Fracture of Engineering Materials & Structures, 2001. 24(10): p. 699-710.

56. Shi, K.K., et al., Prediction of fatigue crack growth based on low cycle fatigue properties. International Journal of Fatigue, 2014. 61(0): p. 220-225.

57. Chen, L., L. Cai, and D. Yao, A new method to predict fatigue crack growth rate of materials based on average cyclic plasticity strain damage accumulation. Chinese Journal of Aeronautics, 2013. 26(1): p. 130-135.

58. Tomkins, B., Fatigue crack propagation—an analysis. Philosophical Magazine, 1968. 18(155): p. 1041-1066.

59. McClintock, F.A., On the plasticity of the growth of fatigue cracks. Fracture of solids, 1963. 20: p. 65-102.

60. Morrow, J., Cyclic plastic strain energy and fatigue of metals. Internal Friction, Damping and Cyclic Plasticity, ASTM STP378, 1965: p. 45-87.

61. Manson, S.S., Fatigue: A complex subject—Some simple approximations. Experimental Mechanics, 1965. 5(4): p. 193-226.

62. Tavernelli, J.F. and J.L.F. Coffin, Experimental Support for Generalized Equation Predicting Low Cycle Fatigue. Journal of Fluids Engineering, 1962. 84(4): p. 533-537.

63. Pandey, K.N. and S. Chand, An energy based fatigue crack growth model. International Journal of Fatigue, 2003. 25(8): p. 771-778.

64. Pantelakis, S.G., T.B. Kermanidis, and D. Pavlou, Fatigue crack growth retardation assessment of 2024-T3 and 6061-T6 aluminium specimens. Theoretical and applied fracture mechanics, 1995. 22(1): p. 35-42.

65. Pratt, J.L., Introduction to the Welding of Structural Steelwork. 1989: Steel Construction Institute.

66. Kosteas, D., Estimating residual stresses and their effect in welded aluminum components in fatigue. Analytical and Experimental Methods for Residual Stress Effects in Fatigue, ASTM STP, 1988. 1004: p. 122-130.

67. Hou, C.Y. and F.v. Lawrence, CRACK CLOSURE IN WELDMENTS. Fatigue & Fracture of Engineering Materials & Structures, 1996. 19(6): p. 683-693.

68. Bate, S., D. Green, and D. Buttle, A review of residual stress distributions in welded joints for the defect assessment of offshore structures. 1997: HSE books.

69. Ma, Y.E., et al., Size effects on residual stress and fatigue crack growth in friction stir welded 2195-T8 aluminium – Part II: Modelling. International Journal of Fatigue,

2011. 33(11): p. 1426-1434.

70.   Pouget, G. and A.P. Reynolds, Residual stress and microstructure effects on fatigue crack growth in AA2050 friction stir welds. International Journal of Fatigue, 2008. 30(3): p. 463-472.

71.   Daniewicz, S.R., J.A. Collins, and D.R. Houser, An elastic-plastic analytical model for predicting fatigue crack growth in arbitrary edge-cracked two-dimensional geometries with residual stress. International Journal of Fatigue, 1994. 16(2): p. 123-133.

72.   LaRue, J.E. and S.R. Daniewicz, Predicting the effect of residual stress on fatigue crack growth. International Journal of Fatigue, 2007. 29(3): p. 508-515.

73.   Newman, J.C., Jr., A crack opening stress equation for fatigue crack growth. International Journal of Fracture, 1984. 24(4): p. R131-R135.

74.   Liljedahl, C.D.M., et al., Weld residual stress effects on fatigue crack growth behaviour of aluminium alloy 2024-T351. International Journal of Fatigue, 2009. 31(6): p. 1081-1088.

75.   Beghini, M. and L. Bertini, Fatigue crack propagation through residual stress fields with closure phenomena. Engineering Fracture Mechanics, 1990. 36(3): p. 379-387.

76.   Newman Jr, J.C., A crack-closure model for predicting fatigue crack growth under aircraft spectrum loading. ASTM STP, 1981. 748: p. 53-84.

77.   Fratini, L., S. Pasta, and A.P. Reynolds, Fatigue crack growth in 2024-T351 friction stir welded joints: Longitudinal residual stress and microstructural effects. International Journal of Fatigue, 2009. 31(3): p. 495-500.

78.   Dalle Donne, C., et al. Effect of weld imperfections and residual stresses on the fatigue crack propagation in friction stir welded joints. in Second international conference on friction stir welding. 2000.

79.   Parker, A., Stress intensity factors, crack profiles, and fatigue crack growth rates in residual stress fields. ASTM STP, 1982. 776: p. 13-31.

80.   Servetti, G. and X. Zhang, Predicting fatigue crack growth rate in a welded butt joint: The role of effective R ratio in accounting for residual stress effect. Engineering Fracture Mechanics, 2009. 76(11): p. 1589-1602.

81.   Labeas, G. and I. Diamantakos, Numerical investigation of through crack behaviour under welding residual stresses. Engineering Fracture Mechanics, 2009. 76(11): p. 1691-1702.

82.   Dugdale, D.S., Yielding of steel sheets containing slits. Journal of the Mechanics and Physics of Solids, 1960. 8(2): p. 100-104.

83.   Fatigue, A.C.E.-o., Effects of Environment and Complex Load History on Fatigue Life: A Symposium. 1970: American Society for Testing and Materials.

84.   Glinka, G. and G. Shen, Universal features of weight functions for cracks in mode I. Engineering Fracture Mechanics, 1991. 40(6): p. 1135-1146.

85.   Bao, R., X. Zhang, and N.A. Yahaya, Evaluating stress intensity factors due to weld residual stresses by the weight function and finite element methods. Engineering Fracture Mechanics, 2010. 77(13): p. 2550-2566.

86.   Bueckner, H.F., Weight Functions for the Notched Bar. ZAMM - Journal of Applied

Mathematics and Mechanics / Zeitschrift für Angewandte Mathematik und Mechanik, 1971. 51(2): p. 97-109.

87. Liljedahl, C.D.M., et al., Evolution of residual stresses with fatigue loading and subsequent crack growth in a welded aluminium alloy middle tension specimen. Engineering Fracture Mechanics, 2008. 75(13): p. 3881-3894.

88. Lam, Y.C. and K.S. Lian, The effect of residual stress and its redistribution of fatigue crack growth. Theoretical and Applied Fracture Mechanics, 1989. 12(1): p. 59-66.

89. Lee, Y.-B., et al., Effects of redistributing residual stress on the fatigue behavior of ss330 weldment. International Journal of Fatigue, 1998. 20(8): p. 565-573.

90. El-Soudani, S. and R. Pelloux, Anisotropy of fatigue crack propagation in aluminum alloy butt welded joints. Welding Journal, 1975. 54(5): p. 144s-152s.

91. Shankar, K. and W. Wu, Effect of welding and weld repair on crack propagation behaviour in aluminium alloy 5083 plates. Materials & design, 2002. 23(2): p. 201-208.

92. Link, L., Fatigue crack growth of weldments, American Society for Testing and Materials. Fatigue and Fracture Testing of Weldments, ASTM STP 1058, 1990: p. 16-33.

93. Nordmark, G., L. Mueller, and R. Kelsey, Effect of residual stresses on fatigue crack growth Rates in weldments of aluminum alloy 5456 plate. ASTM special technical publication, 1982(776): p. 44-62.

94. Kang, K.J., J.H. Song, and Y.Y. Earmme, FATIGUE CRACK GROWTH AND CLOSURE THROUGH A TENSILE RESIDUAL STRESS FIELD UNDER COMPRESSIVE APPLIED LOADING. Fatigue & Fracture of Engineering Materials & Structures, 1989. 12(5): p. 363-376.

95. Tsay, L.W., et al., Microstructures and fatigue crack growth of EH36 TMCP steel weldments. International Journal of Fatigue, 1999. 21(8): p. 857-864.

96. Scialpi, A., L.A.C. De Filippis, and P. Cavaliere, Influence of shoulder geometry on microstructure and mechanical properties of friction stir welded 6082 aluminium alloy. Materials & Design, 2007. 28(4): p. 1124-1129.

97. Cavaliere, P., et al., Mechanical and microstructural behaviour of 2024–7075 aluminium alloy sheets joined by friction stir welding. International Journal of Machine Tools and Manufacture, 2006. 46(6): p. 588-594.

98. Ceschini, L., et al., Effect of friction stir welding on microstructure, tensile and fatigue properties of the AA7005/10vol.Al2O3p composite. Composites Science and Technology, 2007. 67(3–4): p. 605-615.

99. John, R., K.V. Jata, and K. Sadananda, Residual stress effects on near-threshold fatigue crack growth in friction stir welds in aerospace alloys. International Journal of Fatigue, 2003. 25(9–11): p. 939-948.

100. Prime, M.B., et al., Residual stress measurements in a thick, dissimilar aluminum alloy friction stir weld. Acta Materialia, 2006. 54(15): p. 4013-4021.

101. Bussu, G. and P.E. Irving, The role of residual stress and heat affected zone properties on fatigue crack propagation in friction stir welded 2024-T351 aluminium joints. International Journal of Fatigue, 2003. 25(1): p. 77-88.

102. Lombard, H., et al., Optimising FSW process parameters to minimise defects and maximise fatigue life in 5083-H321 aluminium alloy. Engineering Fracture Mechanics, 2008. 75(3): p. 341-354.

103. Elangovan, K. and V. Balasubramanian, Influences of pin profile and rotational speed of the tool on the formation of friction stir processing zone in AA2219 aluminium alloy. Materials Science and Engineering: A, 2007. 459(1): p. 7-18.

104. Hattingh, D., et al., Characterization of the influences of FSW tool geometry on welding forces and weld tensile strength using an instrumented tool. Journal of Materials Processing Technology, 2008. 203(1): p. 46-57.

105. Kim, Y., et al., Effect of welding parameters on microstructure in the stir zone of FSW joints of aluminum die casting alloy. Materials Letters, 2006. 60(29): p. 3830-3837.

106. Cavaliere, P. and F. Panella, Effect of tool position on the fatigue properties of dissimilar 2024-7075 sheets joined by friction stir welding. Journal of materials processing technology, 2008. 206(1): p. 249-255.

107. Jata, K.V., K.K. Sankaran, and J.J. Ruschau, Friction-stir welding effects on microstructure and fatigue of aluminum alloy 7050-T7451. Metallurgical and Materials Transactions A, 2000. 31(9): p. 2181-2192.

108. Golestaneh, A.F., A. Ali, and M. Zadeh, Modelling the fatigue crack growth in friction stir welded joint of 2024-T351 Al alloy. Materials & Design, 2009. 30(8): p. 2928-2937.

109. Kaufman, J.G., Introduction to Aluminum Alloys and Tempers. 2000: A S M International.

110. Fourier, J.B.J., The Analytical Theory of Heat. 2003: Dover Publications.

111. ASTM E92 Standard Test Methods for Vickers Hardness of Metallic Materials, Annual book of ASTM Standards. 2003, American Society for testing and Materials: Philadelphia (PA).

112. ASTM E 837-08 Standard Test Method for Determining Residual Stresses by the Hole-Drilling Strain-Gage Method, Annual book of ASTM Standards. 2008, American Society for testing and Materials: Philadelphia (PA).

113. ASTM E8M Standard Test Methods for Tension Testing of Metallic Materials, Annual book of ASTM Standards. 2001, American Society for testing and Materials: Philadelphia (PA).

114. ASTM E647 Standard Test Method for Measurement of fatigue Crack Growth Rates, Annual book of ASTM Standards. 2000, American Society for testing and Materials: Philadelphia (PA).

115. ASTM E561 Standard Practice for R-curve Determination, Annual book of ASTM Standard. 1998, American Society for Testing and Materials: Philadelphia (PA).

116. SEP 1240 Testing and Documentation Guideline for the Experimental Determination of Mechanical Properties of Steel Sheets for CAE Calculations, 1st edition. 2006, Institute VDEh, : Dusseldorf, Germany.

117. Huda, Z., N.I. Taib, and T. Zaharinie, Characterization of 2024-T3: An aerospace aluminum alloy. Materials Chemistry and Physics, 2009. 113(2–3): p. 515-517.

118. Davis, J.R., Properties and selection: nonferrous alloys and special-purpose materials.

1990: ASM International.

119. Besharati-Givi, K. and P. Asadi, Advances in Friction-Stir Welding and Processing. 2014: Elsevier Science.

120. Threadgill, P., et al., Friction stir welding of aluminium alloys. International Materials Reviews, 2009. 54(2): p. 49-93.

121. Bergner, F., G. Zouhar, and G. Tempus, The material-dependent variability of fatigue crack growth rates of aluminium alloys in the Paris regime. International Journal of Fatigue, 2001. 23(5): p. 383-394.

122. Borrego, L.P., et al., Microstructure dependent fatigue crack growth in aged hardened aluminium alloys. International Journal of Fatigue, 2004. 26(12): p. 1321-1331.

123. Callister, W.D. and D.G. Rethwisch, Materials Science and Engineering: An Introduction, 9th Edition: Ninth Edition. 2013.

124. Sih, G.C. and C.K. Chao, Failure initiation in unnotched specimens subjected to monotonic and cyclic loading. Theoretical and Applied Fracture Mechanics, 1984. 2(1): p. 67-73.

125. Sih, G.C., Methods of analysis and solutions of crack problems. Vol. 1. 1973: Springer.

126. Sih, G.C., Some basic problems in fracture mechanics and new concepts. Engineering Fracture Mechanics, 1973. 5(2): p. 365-377.

127. Sih, G.C., Strain-energy-density factor applied to mixed mode crack problems. International Journal of Fracture, 1974. 10(3): p. 305-321.

128. Anderson, T.L. and T.L. Anderson, Fracture Mechanics: Fundamentals and Applications, Third Edition. 2005: Taylor & Francis.

129. Stephens, R.I., et al., Metal Fatigue in Engineering. 2000: John Wiley & Sons.

130. Shyam, A. and E. Lara-Curzio, A model for the formation of fatigue striations and its relationship with small fatigue crack growth in an aluminum alloy. International Journal of Fatigue, 2010. 32(11): p. 1843-1852.

131. Nedbal, I., J. Kunz, and J. Siegl, Quantitative fractography possibilities and applications in aircraft research. Materials science monographs, 1988. 46: p. 393-403.

132. Nedbal, I., J. Siegl, and J. Kunz. Relation between striation spacing and fatigue crack growth rate in Al-alloy sheets. in ICF7, Houston (USA) 1989. 2013.

133. Moreira, P.M.G.P., P.F.P. de Matos, and P.M.S.T. de Castro, Fatigue striation spacing and equivalent initial flaw size in Al 2024-T3 riveted specimens. Theoretical and Applied Fracture Mechanics, 2005. 43(1): p. 89-99.

134. Takeo, Y. and S. Kiyoshi, The effect of frequency on fatigue crack propagation rate and striation spacing in 2024-T3 aluminium alloy and SM-50 steel. Engineering Fracture Mechanics, 1976. 8(1): p. 81-88.

135. Davidson, D. and J. Lankford, Fatigue crack growth in metals and alloys: mechanisms and micromechanics. International Materials Reviews, 1992. 37(1): p. 45-76.